TU Wien - USTEM (Universitäre Service-Einrichtung für
Transmissionselektronenmikroskopie)

Microstructural Characterization of Advanced Superconducting Materials for Different Components of the CERN hadron-hadron Future Circular Collider

PhD Thesis

Author:
Alice Moros

Supervisor:
Prof. Michael Stöger-Pollach

Dedicated to you, red fox of my heart

Abstract

How far can the curiosity push our capabilities? Is our thirst of knowledge stronger than the fear of our human limits? This is not the incipit of a philosophy manual, but the beginning of a magnificent idea. This idea led the great scientists at the European Organization for Nuclear Research (CERN) to start the huge project of the Future Circular Collider (FCC). We have been asking for ages about the evolution of our Universe and the nature of the matter, antimatter and particles describing it. The Large Hadron Collider (LHC) is the first great machine built at CERN with the aim of satisfying all the open questions related to the origin of the Universe. The discoveries it led to, together with the breakthrough represented by the observation of the Higgs boson, can be considered the starting point transforming the need of exploring new physics into a worldwide collaboration for the realization of a new extraordinary machine. In fact, the FCC aims at pushing the energy and intensity frontiers of particle colliders towards reaching collision energies of 100 TeV: the discovery of a new physics, possible when such energies are at stake, can lead to an extension of the known „Standard Model“ and a better understanding of the Higgs boson. Within this study, scenarios for three different types of particle collisions are examined: hadron (proton-proton and heavy ion) collisions, like in the LHC, electron-positron collisions, as in the former LEP, and proton-electron collisions [1], [2], [3], [4]. This magnificent collider of the future will be the next large research facility after the LHC and its High-Luminosity upgrade (HL-LHC), whose realization is ongoing, once they approach the limits of their discovery potential [5].

According to CERN recently published conceptual design study for a future hadron collider (FCC-hh), this extraordinary machine with its center-of-mass energy target of 100 TeV would be located in a 100 km circumference ring close to Geneva (Switzerland). A key requirement for such a machine is the development of high-field superconducting accelerator magnets, capable of satisfying the requirements given by a non-copper critical current density (J_c) of at least 1500 A/mm^2 at 16 T and 4.2 K [1]. Nb_3Sn, a low temperature superconductor with a critical temperature T_c up to 18.3 K, is currently the best candidate for such magnets, since it is the only affordable material able to meet the afore mentioned requirements. To feed the FCC-hh magnets, new superconducting lines will be developed. Similarly to the LHC electrical layout, also for the FCC case the transfer of the current from the surface to the tunnel, where the magnets are located, would be possible via superconducting links containing tens of cables feeding different circuits [6]. The work related to the realization of such links focuses on the development of novel types of cables made out of MgB_2. Furthermore, since the FCC-hh is expected to produce unprecedented amounts of synchrotron radiation, a superconducting beam screen is necessary in order to protect its sensitive components. Two suitable candidates for the beam screen coating are the high temperature superconductors YBCO and the

technologically still unexploited thallium-based cuprate Tl-1223. Since YBCO is expensive and has a complex preparation on large scale, Tl-1223 could represent the proper choice for the material addressed to the beam screen coating. The introduced materials (Nb_3Sn, MgB_2 and Tl-1223), which represent the best candidates for some of the FCC-hh fundamental components, are the „main characters“ of my PhD thesis. In particular, I investigated their structure on a micro- and nanoscale level, and a greater emphasis was given to the study of Nb_3Sn for the FCC-hh bending magnets.
The microstructural investigation is an essential tool for understanding how the material superconducting properties can be enhanced, in order to exploit them for future applications. The electron microscopy, the science allowing the material microstructural analysis, plays a very important role in terms of studying the material intrinsic and extrinsic attributes for understanding its superconducting behavior. The manufacturing processes the superconducting materials come from are crucial in defining their characteristics: a key point in my work is to understand how the parameters involved in such processes influence the material microstructural features, strictly connected to its superconducting properties. In this way, it would be possible to give the manufactures an effective contribution in terms of producing wires and thin films with enhanced superconducting performance. For the material microstructural characterization electron microscopes were employed: these instruments use accelerated electrons under vacuum conditions in order to generate highly magnified images of specimens. In particular, both a scanning electron microscope (SEM) and a transmission electron microscope (TEM) were used. The first one provides information from the surface of a sample: in fact, electrons scattered by or emitted from its surface are used for image generation. TEM uses instead the electrons transmitted from a very thin specimen (approx. 100 nm) to build images. Since these microscopes are equipped with several attachments such as X-ray detectors (both SEM and TEM) or energy filters (TEM), they provide element-specific information from the sample, e.g. chemical composition, elemental distributions, grain size and shape, doping agents size and density.

This work is part of the Marie Skłodowska-Curie Action EASITrain, funded by the European Union’s H2020 Framework Programme under grant agreement no. 764879.

Acknowledgements

Table of contents

1 Introduction

1.1 The future hadron collider (FCC-hh) at CERN

The European Organization for Nuclear Research (CERN) recently published a conceptual design study for a future hadron collider (FCC-hh) [1]. Figure 1.1 shows the schematic of the ring (27 km) currently present at CERN (Geneva, Switzerland), the large hadron collider (LhC), and of the FCC ring (100 km), in principle capable to host three collider types [1], [2], [3], [4].

This study aims at building a 100 km long tunnel and increasing the collision energy up to 100 TeV, thanks to two counter rotating proton beams with an energy of 50 TeV each. For this high-energy machine of the future, high performance superconducting bending magnets with a nominal dipole field of 16 T are required [7],[8]. Such a field would be about twice the 8.3 T generated by the Nb-Ti magnets in the LHC and about 5 T higher than the 11 T of the Nb_3Sn-based dipole magnet of the high-luminosity (HL) LHC upgrade [1]. Nb_3Sn, already being produced for the magnets of the upcoming HL-LHC [9],[10],[11], is currently the only affordable superconducting material which can lead to conductors delivering a critical current density (J_c) of at least 1500 A/mm^2 at 4.2 K and 16 T [12]. The state-of-the-art internal tin restacked-rod-process (RRP®) Nb_3Sn wires can reach a J_c between 1000 A/mm^2 and 1200 A/mm^2 at the afore-mentioned conditions. Researchers and industrial partners are therefore collaborating in developing and studying innovative wire manufacturing technologies, in order to achieve a higher J_c performance.

Why are the dipole magnets so important? Due to their magnetic field, these components steer the proton particle beam, keep it in orbit inside the circular accelerator, and confine it in a well-defined volume inside a vacuum pipe [13], [14].

Another important function is to focus the beam, giving it the required stability in the plane perpendicular to the trajectory [13]. Beside dipoles, other magnet types (quadrupoles, sextupoles and octupoles) take care of the stability of the beam in the transverse space. A detailed overview of the accelerator magnet types can be found in [13], [1], [15]. Nb_3Sn superconductors manufactured via Internal-Tin (including RRP®) and Powder-In-Tube (PIT) processes are envisioned for FCC-hh dipole magnets, and have been studied in the conductor development program [7], [8], [16], [17]. Both manufacturing technologies are described in the subsection 1.2.2.

In Figure 3.46, J_c of state-of-the-art wires (between 1000 A/mm^2 and 1200 A/mm^2) is compared to the FCC target (1500 A/mm^2). Three methods are principally used to raise J_c in Nb_3Sn wires: reducing the inhomogeneities in terms of Sn concentration gradient over the wire cross-section [18], [19], [20], introducing artificial defects [21], and reducing grain size [22]. In this work, a major emphasis will be given to the first point.

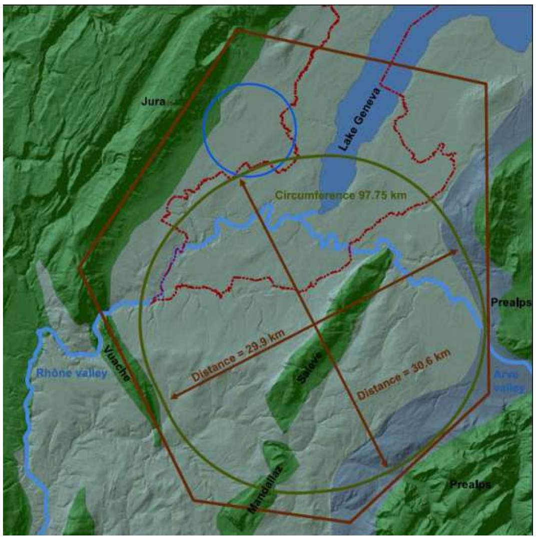

Figure 1.1: Schematic of the 27-km-long tunnel of the LhC, currently present at CERN (light blue circle), and the about 100-km-long tunnel of the FCC (light brown circle), in principle capable to host three collider types [1].

We investigated the Sn concentration gradient in Nb_3Sn wires with different layouts produced by TVEL and the Bochvar Institute (Moscow, Russia), and we analyzed doping agents (artificial defects) size and density in wires produced by Hyper Tech Reasearch, Inc. (Columbus, Ohio). The microstructural characterization of Nb_3Sn wires through several electron microscopy techniques is the main focus of this thesis (Chapter 3).

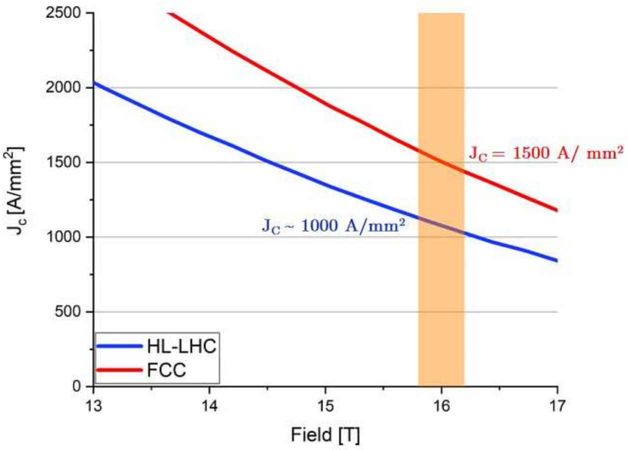

Figure 1.2: J_c of state-of-the-art wires (between 1000 A/mm^2 and 1200 A/mm^2) compared to the FCC target (1500 A/mm^2). *Graph adapted from [23].*

Table 1.1 is showing a comparison between some of the main parameters forseen for the FCC-hh and those currently charactering the LhC [1], [3].

Parameter	FCC-hh	LhC
Collision energy [TeV]	100 TeV	14 TeV
Dipole field [T]	16	8.33
Circumference [km]	97.75	26.7
Synchrotron radiation power per beam [kW]	2400	3.6
Stored energy per beam [GJ]	8.4	0.39

Table 1.1: Some fundamental collider-parameters: FCC-hh vs LhC. Other important parameters can be found in [1], [3].

As visible in Table 1.1, the proton beams circulating in the accelerator would produce several tens of watts of synchrotron radiation per meter due to their high energy. A beam screen is necessary to prevent this radiation from impinging on the dipole magnets. This beam screen would be kept at 50 K for cryogenic efficiency (see ”working point” in Figure 3.46). Its surface impedance needs to be minimized for beam stability reasons: to guarantee a better performance than copper (used in LhC) would allow, the only alternative materials are High Temperature Superconductors (HTSs).

The dashed lines of Figure 4.19 represent the irreversibility field (H_{irr}) of different superconducting materials. The irreversibility field of a ”type II” superconductor is *the field up to which you can easily pass current and it is often about four times lower than the critical field* [24] (B_c). According to the displayed H_{irr} lines, two suitable candidates for the beam screen coating are YBCO and the technologically still unexploited thallium-based cuprates Tl-1223. As YBCO is expensive and has a complex preparation on large scale [25], Tl-1223 is currently being investigated for the FCC-hh beam screen [26], [27], [28]. Specimens of both materials are typically prepared through deposition techniques [29], [26], [30], [31]. The advantages of Tl-1223 over YBCO [28] are summarized in Table 1.2.

Material	Pros	Cons	Deposition-substrate requirements
Tl-1223	High J_c High H_{irr} Higher critical temperature T_c: $\sim$ 120 K [26] Very tolerant for out stoichiometry	Toxic	No sophisticated texture
YBCO	Safe High J_c High H_{irr}	Very expensive Complex preparation on large scale Lower T_c: $\sim$ 93 K [32]	High-quality biaxial texture

Table 1.2: Advantages of Tl-1223 over YBCO [27], [33].

In the next section (”The phenomenon of superconductivity: some fundamental aspects”), the concepts of type II superconductor, J_c, B_c, H_{irr}, and T_c will be better clarified.

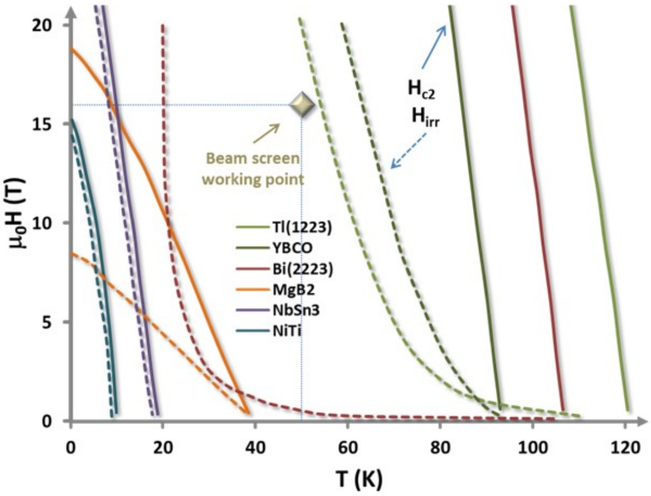

Figure 1.3: Magnetic field (T) vs temperature (T) graph showing the beam screen working point (50 K at 16 T) [27]. The H_{irr} lines (dashed ones) of different superducting materials are displayed.

As thallium-based superconductors are still little known, it is important to find the optimal recipe in terms of thin film deposition. Electrochemical deposition performed at CNR-SPIN in Genoa, Italy (subsection 1.3.2) is demonstrating high potential for the production of increasingly optimized Tl-1223 thin films [26]. Once the most effective recipe is defined, large-scale production could be possible [33]. The microstructural investigation we performed on the produced thin films aimed at assessing the formation of the desired Tl-1223 phase, and the substrate coverage, together with the connection between grains (Chapter 4). In the case of HTSs, J_c is strongly dependent on the grain boundary misalignment and is drastically suppressed if the misorientation angles are too big, i.e. the grains are not well connected. The results of our analyses will contribute to a better understanding of the potential of the still mysterious thallium-based superconductors to advance the FCC-hh design project.

The FCC-hh magnets would be powered by superconducting lines made out of MgB_2 [6], [34]. These superconducting links, being already under study for the CERN HL-LHC project, would be located in the FCC-hh tunnel to transport current from the power supplies to the magnet coils [6], [11],[1], [9], [10]. The power converters and the current leads (see Figure 1.4) would be located either in surface buildings or in underground areas [6], and the MgB_2 superconducting links carrying current to the magnets ”would contain tens of cables transferring altogether more than 150 kA” [6].

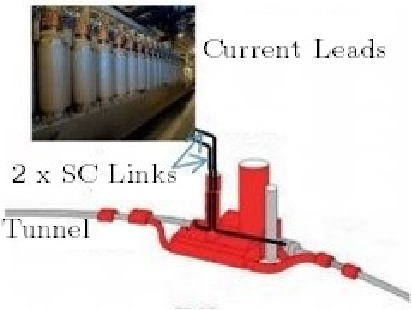

Figure 1.4: Schematic of two superconducting links powering the magnets developed in the context of the CERN HL-LHC upgrade. *Figure adapted from [6].*

As for Nb_3Sn, the increase in J_c plays an important role for MgB_2 as well. The J_c enhancement was observed as a consequence of partial substitution of B by carbon, after the reaction with C based compounds [35]. In this framework, we characterized the microstructure of C-doped MgB_2 wires produced at CNR-SPIN (Genoa) [36] using haemoglobin and inulin as C sources. We investigated C dispersion within the MgB_2 matrix to better understand the role of C in raising the J_c value (Chapter 5).

Dipole magnets, beam screen, and superconducting links just a few of the major components necessary for the operation of FCC-hh. A complete picture of the design of this grand machine of the future can be found in [1].

1.1.1 The phenomenon of superconductivity: some fundamental aspects

This section will review some key steps in the history of superconductivity. We will then focus on some aspects of this phenomenon to better clarify the scope of this work.

- **1908:** H. Kamerling Onnes succeeded in liquefying helium and began to study the electrical properties of conductive materials at very low temperature (up to 1K).
- **1911:** following his research on cryogenic techniques, and studying the conduction of mercury at low temperatures, H.K. Onnes discovered the phenomenon of superconductivity: below a characteristic critical temperature T_c the material resistance drops abruptly to zero.
- **1913:** H.K. Onnes reported that there was a critical value of the current density (J_c) in mercury, temperature dependent and above which the resistance-free state disappeared. This value increases as the temperature is reduced below T_c. He also understood that superconductivity disappears in presence of a magnetic field above a critical and temperature-dependent value (B_c). He won the Nobel prize.
- **1933:** H.K. Onnes, W. Meissner, R. Ochsenfeld discovered that the superconductor is not only a perfect conductor, but also has the property to prevent magnetic fields

to penetrate it. In fact, a superconducting material develops on its surface screen currents that induce a magnetic field, inside the superconductor itself, able to compensate the external one (perfect diamagnetism or Meissner effect).

- **1934:** C.J. Gorfer and H.B.G. Casimir proposed a two-fluid model providing a macroscopic description of the thermodynamic properties of superconductors, by defining the existence conditions of "normal" and "superelectron" electrons.
- **1935:** Brothers F. and H. London developed two equations that describe macroscopically the state of zero resistance and the Meissner effect.
- **1950:** H. Froehlich, V.L. Ginzburg, L.D. Landau, A.B. Pippard, E. Maxwell, C.A. Reynolds et al. explained the superconducting state through a theory focusing on electron-phonon interaction.
- **1954:** B. Matthias found Nb_3Sn to be a superconductor with T_c of about 18 K.
- **1956:** S.C. Colins and L.N. Cooper experimentally determined the upper limit of the resistivity of a superconductor. Introduces the concept of electron pairs (Cooper pairs).
- **1957:** J. Bardeen, L.N. Cooper, and J.R. Schrieffer developed the microscopic theory of superconductivity based on quantum mechanics and known as BCS Theory. This theory is still the most comprehensive explanation of the superconductivity of metallic materials.

  Alexei Abrikosov discovers an essentially new mechanism of superconductor interaction with the magnetic field for the new class of superconductors, called by him "type II superconductors"; he envisions the possibility of vortex lattice formation. The way for applications of superconductivity in intense magnetic field (but still at low temperature), is open. He won the Nobel prize in 2003.
- **1961:** J.E. Kunzler et al., B.S. Deaver, W.M. Fairbank identified a group of superconducting compounds and alloys capable of carrying very high currents (10^6 A/cm^2) in very intense fields (30 T), awakening interest in power applications (type II superconductors). They experimentally verified the quantization of the flux enclosed by a ring-shaped superconductor.

  Ability to support high currents and magnetic fields was discovered in Nb_3Sn. The era of superconductivity for large-scale applications started.
- **1962:** B.D. Josephson analyzed what happens between two superconductors separated by a thin insulating layer (Josephson junction), thus paving the way for future electronic applications of superconductivity.

  T. G. Berlincourt and R. R. Hake discovered the outstanding superconducting properties of Nb-Ti which made its alloys as the most widely used superconductors.

- **1970:** The first reliable superconducting magnets are realized.
- **1972-1973:** J. Bardeen, L.N. Cooper, J.R. Schrieffer, and I.Giaever and B.D. Josephson won the nobel prize.
- **1973:** J.R. Gavaler prepares a compound of Nb_3Ge with a T_c of about 23 K, the highest among conventional metal superconductors or low critical temperature superconductors (LTSs).
- **1986:** As a result of extensive studies on the electronic properties of perovskites, A. Mueller and G. Bednorz observed the transition to the superconducting state at 34 K in the compound $La_{2-x}Ba_xCuO_4$:this is the first discovered cuprate superconductor. This experiment opened the way to a new class of superconductors with transition temperatures T_c above 90 K and that can be cooled with liquid nitrogen. These are called high critical temperature superconductors (HTS)s.
- **1987:** The post-doctoral researcher Zhengzhi Sheng and Allen M. Hermann discovered Tl-based superconducting cuprates (T_c between 90 K and 130 K).
- **2001:** J. Akimitsu discovers superconductivity at 40 K in the simple binary compound MgB_2.
- **2003:** A.A. Abrikosov, V.L. Ginzburg, A.J. Leggett won the Nobel Prize for pioneering contributions to the physics of superconductivity and superfluidity.
- **2008:** H. Hosono et al. discovered superconductivity at 25 K in LaFeAs(O,F). The era of iron-based superconductors began.
- **2013:** Room-temperature superconductivity was obtained in $YBa_2Cu_3O_{6.5}$ for picoseconds, using short pulses of infrared laser light to deform the material crystal structure.
- **2017:** Undiscovered superhard materials, such as critically doped beta-titanium Au, were pointed out as possible candidates for new superconductors with high T_c, up to 233 K (exceeding the T_c known to be the highest, 134 K of HgBaCuO).
- **2018:** Researchers noted a possible superconducting phase at 260 K in LaH_{10} achievable with very high pressure (200 GPa).
- **2020:** Room-temperature superconductivity at 288 K was reported in a carbonaceous sulfur hydride at 267 GPa.

More information about the history of superconductivity can be found in [24], [37], [38], [39], [40], [41], [42], [43], [44].

1.1.1.1 Type I and type II superconductors

The information here provided is based on [24], [45], and [46].

Type I superconductors, according to the afore-mentioned Meissner effect, expel the magnetic field completely for an applied field smaller than B_c. Above B_c, the material abruptly reverts to the normal resistive state (Figure 1.5a). Type I superconductivity is represented by most elementary superconductors (e.g., Pb, Hg, Sn, etc.), except Nb, V, and Tc [47]. The values of T_c for type I superconductors are usually < 10 K, those of B_c are in the range of 5-200 mT [47]. Due to their low T_c and B_c values, Type I superconductors have limited use in terms of applications.

As observable in Figure 1.5b, type II superconductors have two critical magnetic fields (B_{c1} and B_{c2}). Below B_{c1}, the type II superconductor behaves like the type I one, expelling completely the magnetic flux (Meissner effect). For B between B_{c1} and B_{c2}, the magnetic flux begins to penetrate the sample in the form of discrete bundles called ”flux lines” and the sample goes into the mixed state or “vortex state”. A.A. Abrikosov demonstrated that the magnetic field penetration here occured as single tubes containing a quantum of magnetic flux and electrical current flowing around them to shield the sorrounding superconducting region from magnetic field. Such tubes look like vortices because of the way the electrical current circulates around them (see Figure 1.6 in the next section). For B higher than B_{c2}, the superconductor is in the normal resistive state. Type II superconductivity is typical of metal compounds, alloys, and complex oxide ceramics. All materials analyzed in this work (Nb_3Sn, Tl-1223, and MgB_2) are type II superconductors. The critical magnetic fields and J_c values characterizing this type of superconductors are much higher than those of type I. Therefore, these materials have a higher potential for practical applications.

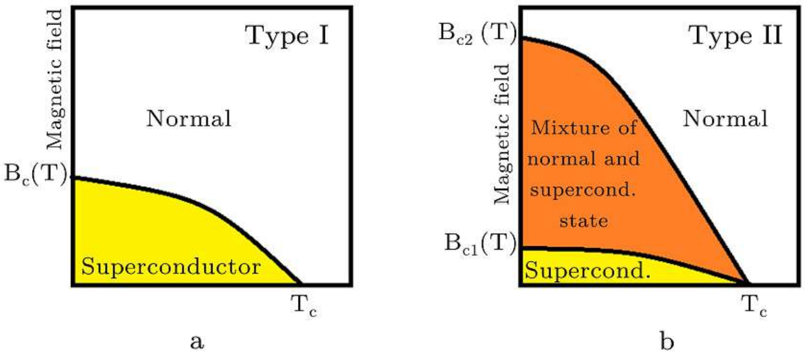

Figure 1.5: Schematic of type I (a) and type II (b) superconductors showing a clear separation between superconducting and normal resistive state (a), and a gradual transition from superconducting to normal state due to the presence of a mixed state (b).

To further clarify type I and type II superconductors, two concepts will be introduced: the coherence length ε and the penetration depth λ.

The London brothers, with their equation, showed that magnetic fields are excluded from a superconductor (Meissner effect) but that the field could penetrate a very short distance into the superconductor surface. This distance is the London penetration depth λ.

Pippard defined as coherence length ε the distance needed for superconductivity to turn on, measured from a region where there is no superconductivity. According to this, it is not possible to have a clear interface between superconducting and non-superconducting regions: the transition takes place gradually over a transition layer of thickness related to ε. In we consider the superelectrons as Cooper pairs (BCS Theory [48]), ε could be simply described as the length within which electrons can still be considered paired.

In type I superconductors, ε is much larger than λ. In this case, the energy cost of destroying superconductivity near the interface superconducting-normal state exceeds the energy bonus of allowing the field to penetrate a little. The interface between the superconducting and the normal state is costly and the system prefer not to make an interface unless it is necessary. In type II superconductors, λ is much longer than ε. The energy cost of destroying superconductivity near the interface superconducting-normal state is outweighed by the energy bonus of allowing the field to penetrate: this means that having an interface between superconducting and normal state saves energy, and thus the formation of interfaces is extremely favorable. A type II superconductor will be full of interfaces (vortices).

The ratio of λ over ε defines the Ginzburg-Landau parameter κ. Type I superconductors satisfy the condition $\kappa < \frac{1}{\sqrt{2}}$, whereas for type II superconductors $\kappa > \frac{1}{\sqrt{2}}$.

1.1.1.2 Critical current density J_c and flux pinning

The concept of "vortices" characterizing the mixed state of type II superconductors was introduced in the previous section. Abrikosov considered the vortices as the explanation for many superconductors appearing to exhibit an imperfect Meissner effect by letting the magnetic field penetrate through them [45].

The critical current density (J_c) is a crucial parameter of a superconductor and it's directly related to its potential for practical applications [49], [50], [51], [45]. It is determined by the T_c, electronic structure, and the so-called "flux pinning mechanism" due to naturally or artificially generated microscopic defects in the material [45]. As previously described, the magnetic flux penetrates into the superconducting sample in the form of tubes with normal-conducting cores and surrounded by vortex-shaped supercurrents. Such tubes or vortices are also known as fluxons. An example of fluxon can be observed in Figure 1.6 (brown cylinder). Vortex currents cause any two vortices to repel each other forming an ordered lattice called the "Abrikosov vortex lattice" [45]. If an electric current flows through a superconductor in its mixed state, the vortices would experience a Lorentz force $\vec{F_l} = \vec{J} \times \vec{B}$, for which they would begin to move in a direction perpendicular to the directions of the transport current $\vec{J}$ and the applied magnetic field $\vec{B}$. However, certain types of defects or impurities in superconducting materials (dislocations, voids, grain boundaries, etc.) act as pinning centers for the vortices and the magnetic flux is trapped. Simply said, these defects would prevent the fluxons from moving across the material and so leading it to go into the normal resistive state. They are said to "pin" the fluxons, which is why they are commonly referred to as pinning centres. What does it mean that they are pinning the vortices/fluxons? The force withstanding the motion of fluxons under the influence of $\vec{F_l}$ is the "pinning force" $\vec{F_p}$, which is the one related to the presence of defects in the material. The flux lines remain static, as long as $F_p > F_l$ [45]. If $F_l > F_p$, fluxons start moving across the superconductor with a velocity v, and an electric field is generated. As both the current and the generated electric field would be parallel, a certain amount of power would be dissipated in the system and the superconductor would lose its ability to sustain a current flow without dissipation. A schematic of the forces involved is presented in the figure 1.6.

The penetration of magnetic flux into a type II superconductor is gradual over a wide range of applied magnetic field [45]. The presence of lattice defects can change the structure of the vortices, leading them to be "stuck" at the defect sites and thus no longer free to move. The defect sites are surrounded by an energy barrier that the vortex must be able to overcome to start moving. The Lorentz force lowers this energy barrier and the J_c of a sample would be reached when the pinning force is balanced by the Lorentz force. Thermal activation also lowers the height of this energetic barrier, resulting in a J_c that is strongly temperature dependent [45].

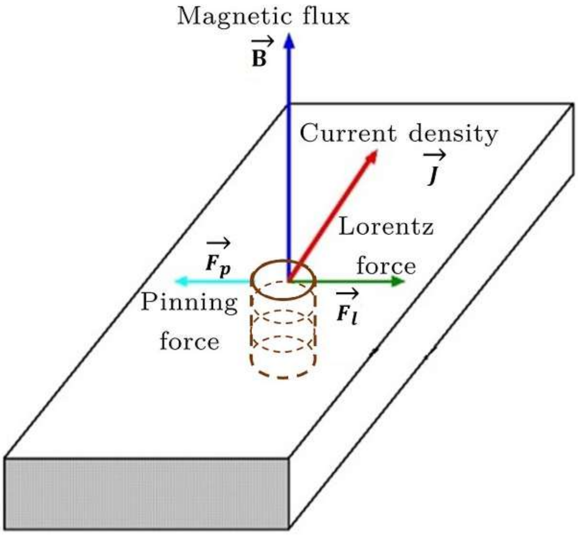

Figure 1.6: Schematic of flux pinning in type II superconductors. The brown cylider represents a vortex.
Figure inspired by the similar one in [48].

Introducing the concept of pinning centers will help to know its meaning when we talk about it for Nb_3Sn in chapter Chapter 3 and for MgB_2 in chapter Chapter 5.

1.2 Nb_3Sn for the FCC-hh bending magnets

In this section, some general properties of Nb_3Sn are explored along with the related wire manufacturing technologies.

1.2.1 General properties

Nb_3Sn is a type II superconductor and a LTS with T_c up to 18.3 K [52]. It is a brittle intermetallic compound with a Cr_3Si structure type, also known as A15 phase, belonging to the space group $P_{m3n}\left(O_h^3\right)$. In the course of this thesis we will sometimes refer to Nb_3Sn as A15. The A15 phase corresponds to a Sn content in the range between 18 at.% and 25 at.% [53], [54]. According to J. P. Charlesworth et al. [55], this range would be even wider (between 17 at.% and 27 at.%). A phase diagram of the Nb-Sn system can be found in [54].
Figure1.7 exhibits a schematic of the Nb_3Sn unit cell: the Nb atoms are located at $\left(\frac{1}{2},\frac{1}{2},\frac{1}{2}\right)$ (lying on the sides of the unit cell in three chains orthogonal to each other), and the Sn atoms at (000) and $\left(\frac{1}{2},\frac{1}{2},\frac{1}{2}\right)$ (on bcc sites) [56],[49]. The Nb_3Sn lattice parameter is 0.529 nm [52].

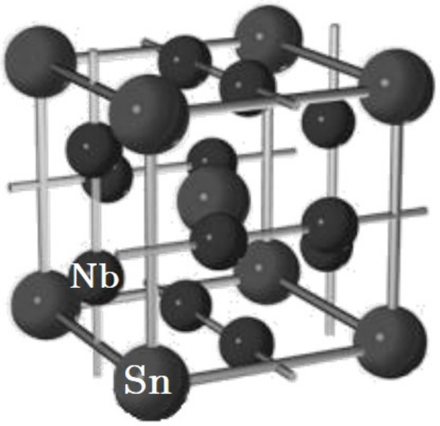

Figure 1.7: Crystal structure of Nb_3Sn where the Sn atoms (big spheres) are located at corner and centre sites of the cube, and the Nb atoms (small spheres) lying in three orthogonal chains.
Figure adapted from [49].

If we speak about multi-filamentary Nb_3Sn composite wires, we refer to a conductor where thin superconducting filaments are distributed in a normal low resistance matrix, which is typically Cu (see Figure 1.8) [53]. Due to its high thermal conductivity, this matrix carries heat away from the surface of the superconducting filaments, it absorbs a significant amount of heat because of its specific heat, and decreases Joule heating when the superconductor transit into the normal resistive state [53].

If single-phase Nb_3Sn is formed by solid-state diffusion above approximately 930 °C in the binary Nb-Sn system, the presence of Cu in the ternary system Nb-Sn-Cu effectively lowers this temperature to practical values in industrial wires of about 650°C [53]. Grain growth would thus be limited, so retaining a higher grain boundary density, which is a fundamental aspect for flux pinning in Nb_3Sn [53], [54], [57].

Considering the brittle nature of Nb_3Sn, its formation through heat treatment and diffusion process (described in the next section) is postponed until the desired conductor configuration is obtained [53]. The conductor configuration studied in this work is multi-filamentary wire.

In the modern multi-filamentary Nb_3Sn wires, ternary compounds such as $(Nb,Ti)_3Sn$ and $(Nb,Ta)_3Sn$ are formed by adding 1 at.%–2 at.% of Ti or 2 at.%–4 at.% of Ta. This is a stratergy adopted to enhance B_{c2} without sacrificing T_c [58], [59]. The highest B_{c2} values in ternary Nb_3Sn wires was found to be around 30 T [60], [61].

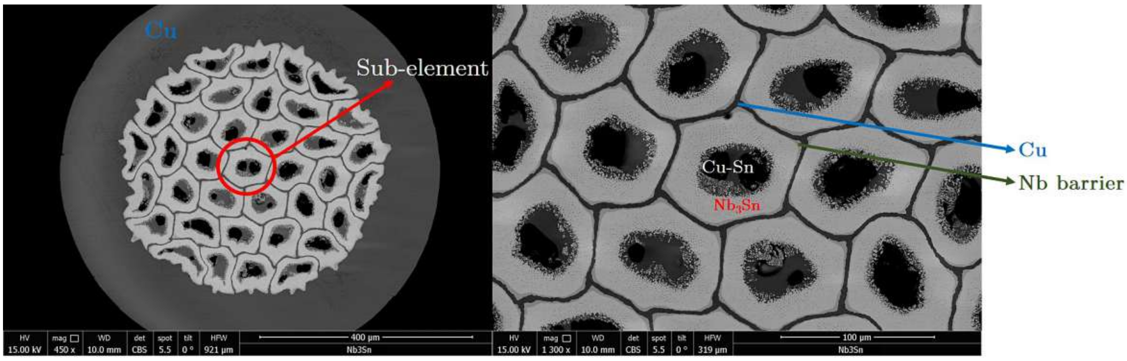

a b

Figure 1.8: SEM images taken with the backscatter detector - BCS (details in Chapter 2) and representing (a) a typical overview of a multifilamentary Nb_3Sn wire, and (b) the filament (or sub-element) features. A filament or sub-element is pointed out in (a) with a red circle.

As described in the beginning of this thesis, the J_c enhancement represent one of the main goals of the FCC-hh project. Previously, we mentioned a "non-Cu J_c": as a typical Nb_3Sn wire consists of different phases (Nb_3Sn, Nb and Cu), T_c can be mainly defined in three ways [60].

1. The engineering J_c is intended as the average critical current density over the whole wire cross-section, including the A15 phase, the Cu one, the Nb barrier, and the residual Cu and Sn in the sub-element core.
2. The layer J_c is represented by the critical current density of the A15 phase.
3. The non-Cu J_c, the one used for the FCC-hh target value (1500 A/mm^2 at 16 T and 4.2 K), is the average critical current density of the A15 phase, the Nb barrier, and the residual Cu and Sn in the sub-element core.

Some of the main application areas of Nb_3Sn conductors are the following [60]: tokamak fusion devices (such as International Thermonuclear Experimental Reactor, ITER) for the central solenoid (CS) and the toroidal field (TF) coils, high-energy physics (FCC projects) in terms of dipole and quardrupole magnets, magnetic resonance imaging (MRI), and nuclear magnetic resonance (NMR).

1.2.2 Manufacturing process of Nb_3Sn wires

We can classify Nb_3Sn wire production technologies into standard processes and internal oxidation method. The standard manufacturing techniques are mainly three: the bronze process, the internal tin (IT) process including the RRP® variant and the powder-in-tube (PIT) process [16], [53]. All production techniques are characterized by a final high-temperature heat treatment step for the formation of the A15 phase. The entire heat treatment process consists of several steps with different temperatures (up to around 700°C) and duration. Details about the heat treatment steps can be found in [62], [16],

[52], [63].

In the bronze process, the Sn source is represented by a Cu-Sn bronze matrix [64], [60]. A certain number of Nb rods is inserted into this matrix. The composite is now wrapped with a Ta foil and inserted into a Cu can, and the stacked system is then drawn down to the final size [60]. Ta foils have the function of preventing Sn leakage into the Cu matrix during heat treatment. Each Nb alloy rod in the bronze matrix transforms to a Nb_3Sn sub-element after heat treatment, leading to small filament size (2-3 μm). As solubility of Sn in bronze is limited, Sn content in the formed Nb_3Sn phase is low, and so J_c is [60].
Considering the previously mentioned high J_c requirements, and the need to produce in large quantities, only Nb_3Sn IT, including RRP®, and PIT wires are currently considered (among the standard produced wires) for high-energy physics applications [59], [12], [16].

As a variation of the IT process, the RRP® maintained the record for the production of wires with the best performance for many years, until PIT wires with artificial pinning centres (or internally oxidized APC wires) achieved the J_c FCC-hh specifications in short samples (2019) [16]. The specimens investigated in Chapter 3 of this manuscript are mainly IT wires. A part of this work is also dedicated to the preliminary analysis of internally oxidized APC wires (for simplicity, we will call them APC).
In the IT RRP® process, Nb rods (filaments) are stacked into a Cu matrix. A Sn or Sn-alloy rod is located in the core (central hole) of this matrix, and the whole composition is formed into easily stackable hexagonal rods. A thin Nb or Ta barrier is typically used to prevent Sn from diffusing into the Cu matrix. Multiple of these sub-elements are inserted into a copper tube. The final wire size is achieved by cold drawing. During the heat treatment, Sn diffuses outwards and meets the Nb rods, so forming the Nb_3Sn phase. IT wires usually show high J_c values due to their optimal Sn content [65], [16], [52]. Doping of such wires is performed by inserting Ti or Ta rods between the Nb filaments inside sub-elements: Ti has the role of lowering and optimizing the heat treatment temperatures. Ta rods, as previously said, help enhancing B_{c2} without sacrificing T_c [16], [58], [59].
A simplified schematic of the IT process is reported in Figure 1.9.

In the PIT process, tubes made of Nb or Nb-alloys are filled with fine $NbSn_2$ powder and Cu (few at.%) to help A15 phase formation occurring faster below a temperature of 700 °C. The filled tubes are inserted into a Cu matrix and the wire is then drawn to its final size. For the A15 phase formation, a final heat treatment step at a temperature of about 675 °C is performed (it typically lasts a few days). More details about this production technology can be found in [65], [19], [16].

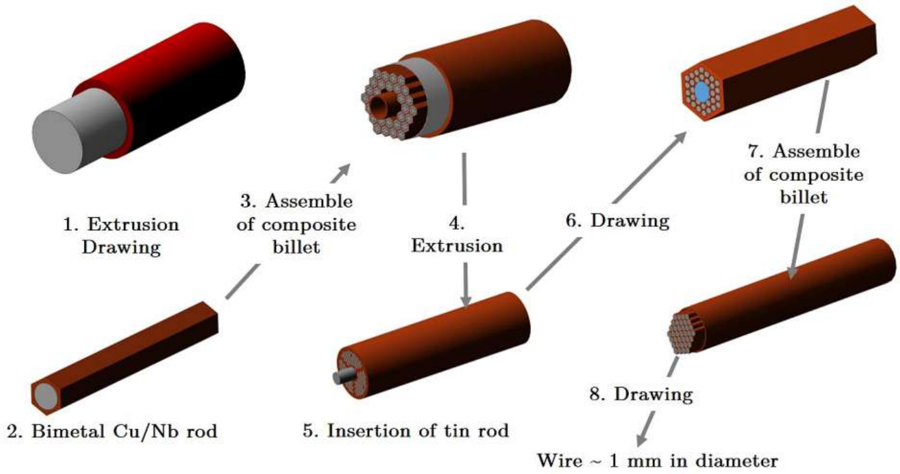

Figure 1.9: Simplified schematic of manufacturing steps to produce a IT wire. In the "insertion of tin rod" (step 5) you may notice that the Nb filaments area is divided into 3 regions by Cu insertions. This is the specific case of a Nb_3Sn IT wire with cluster layout. This layout type will be discussed in Chapter 3. *Figure adapted from [66].*

In 2019 new generation APC wires manufactured by Hyper Tech Research Inc. have achieved a J_c close to the FCC target of 1500 Amm^{-2} at 16 T, corresponding to a J_c of 3600 Amm^{-2} at 12 T [16].

In these wires, Nb_3Sn grain refinement (fundamental aspect contributing to flux pinning) was obtained by adding Zr and O to Nb and Sn before heat treatment, so leading to the internal oxidation of Zr and the formation of ZrO_2 nanoprecipitates. As a consequence, a reduction in Nb_3Sn grain size was achieved [22], [60]. An internally oxidized wire is like a PIT wire where O is supplied by adding SnO_2 powder. 1 at.% Zr is alloyed with Nb. An example of PIT APC wire is reported in [67]. Intra-granular ZrO_2 precipitates could potentially act as pinning centres contributing to the increase of the pinning force in such a wire type [68]. As the affinity of Zr to O is much stronger than the affinity of Nb to O, a Nb-Zr alloy is typically used. The oxygen required to oxidize Zr atoms during the heat treatment is usually supplied in the form of oxide powders located inside the sub-elements. The resulting ZrO_2 nanoprecipitates were observed both at grain boundary and in the grains with diameters of approx. 2-15 nm.

Recently, internally oxidized Nb_3Sn wires were found to have an average grain size of 36 nm and J_c values significantly increased (almost twice as high as in conventional Nb_3Sn wires) [69].

The internal oxidation process is also performed with Hf instead of Zr, since both elements show a high affinity to O. Both Zr and Hf routes were employed with and without an O source in the form of SnO_2, and the highest pinning performance was obtained using a Nb4Ta1Hf alloy without SnO_2 [70]. The addition of Ti to APC wires has been explored with success, leading to small sub-elements (25 μm in diameter) [68]. In the newest generation of APC wires, the addition of Ta brought B_{c2} values of 28T.

1.3 Tl-1223 for the FCC-hh beam screen

In this section, some general properties of Tl-1223 are explored along with the electrodeposition process performed at CNR-SPIN to produce thin film samples.

1.3.1 General properties

Tl-1223 is a type II superconductor and a HTS with $T_c \sim 120$ K [71], [72]. It is described by the general formula of Tl-based cuprates TlmBa2Can-1CunO2n+m+2 (abbreviated as Tl-m2(n-1)n), where m = 1 and n = 3. Among Tl-based superconductors, Tl-1223 is one of the preferable candidate in terms of applications due to its high T_c, and its efficient flux pinning properties [73], [74], [75]. Liu et al. reported a simultaneous partial substitution of Tl with Bi and Pb, and Sr for Ba in the form of $(Tl_{0.6}Pb_{0.2}Bi_{0.2})(Sr_{1.8}Ba_{0.2})Ca_2Cu_3O_{9+\delta}$ leading to an increase of T_c with respect to the other Tl-based compounds, and an accelerated formation of the Tl-1223 phase citeliu1994improvement, [76]. Tl-1223 crystal structure belongs to the space group P4lmmm [77] and the dimensions of the unit cell are: $a = 3.814\,\text{Å}$ and $c = 15.29\,\text{Å}$ [77][78]. A phase diagram for this compound is reported in [79]. This compound shows a single insulating Tl-O layer between the current carrying Cu-O layers [76]. The reduced spacing between Cu-O layers causes an increase in the coupling energy between the Cu-O planes [76]. It was suggested that such an increase in the coupling energy prevents the vortex lattice from being thermally activated (which would cause the transition to the normal resistive state) [80], [76].
Figure 1.10 shows Tl-1223 primitive tetragonal unit cell.

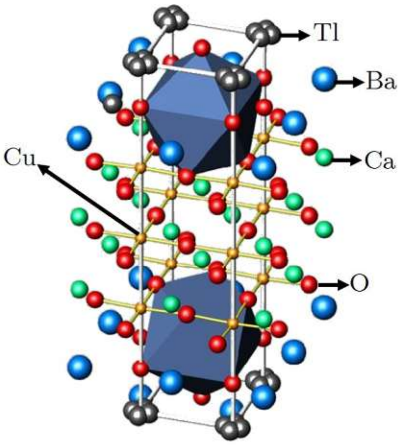

Figure 1.10: Crystal structure Tl-1223 showing Tl split positions (black atoms), Ba (blue), Ca (green), Cu (orange), and O (red). *Figure adapted from [81].*

1.3.2 Manufacturing process of Tl-1223 thin films

Tl-1223 thin films were produced at CNR-SPIN in Genoa via electrodeposition process in a 3-electrode system by employing a flat cell [26], [82].

This manufacturing process consists in depositing a film of a complex oxide compound based on Tl, Bi, Pb, Ba, Sr, Ca, and Cu on Ag and $SrTiO_3$ (STO) substrates (metallized via sputtering) [83], [82]. Considering the required properties for the future application, we selected $Tl_{0.7}Bi_{0.2}Pb_{0.2}Sr_{1.6}Ba_{0.4}Ca_{1.9}Cu_3O_{9\ +x}$ [26].

The working, counter and reference electrodes were represented respectively by substrate, platinum grid, and $Ag/AgNO_3$ 0.1 M in Dimethyl Sulfoxide (DMSO, Sigma-Aldrich, 99.9%, anhydrous, suresealed grade). Nitrates of the phase elements were dissolved in 250 ml of DMSO. At this process step, the stoichiometry of the solution is far from the one required on the substrate due to the large difference in the overpotential for the different ions [26]. By iterative analysis of the deposited precursors using dispersive X-ray spectroscopy (EDX, described in Chapter 2), we obtained the required element contents: 0.25 g of $TlNO_3$, 0.18 g of $Bi(NO_3)_3 \cdot 5H_2O$, 0.18 g of $PbNO_3$, 2.73 g of $Sr(NO_3)_2$, 1.52 g of $Ba(NO_3)_2$, 1.63 g of $CaNO_3 \cdot H_2O$ and 1.33 g $Cu(NO_3)_2 \cdot H_2O$. The film deposition was performed between - 2.9 V and - 3.1 V for 600 s with a commercial potentiostat. Since DMSO is a high boiling point solvent, samples were dried under vacuum at 120 °C before performing the final high-temperature heat treatment. They were then processed in a three-zone tube furnace in a partially closed system inside a gold foil crucible for 10 min at 885 °C.

Thallium oxide is volatile above 710 °C, so it is very important to keep the sample in a thallium atmosphere. The latter was created by keeping Tl_2O_3 powder (4 mg) and Tl-1223 pellets (whose production is described in [26]) along with the precursor film during the heat treatment. For the last films produced, a thallium atmosphere was created using only Tl_2O_3 powder in a different amount (more details will be given in Chapter 4). By doing so, we aimed at finding the best compensation between losses and reabsorption of thallium-bismuth-lead: the precursor-pellet releases with an already balanced stoichiometry and this helps the growth of Tl-1223 phase.

Further details about this Tl-1223 thin film electrodeposition process can be found in [26].

In Figure 1.11, the electrodeposition system used at CNR-SPIN is shown.

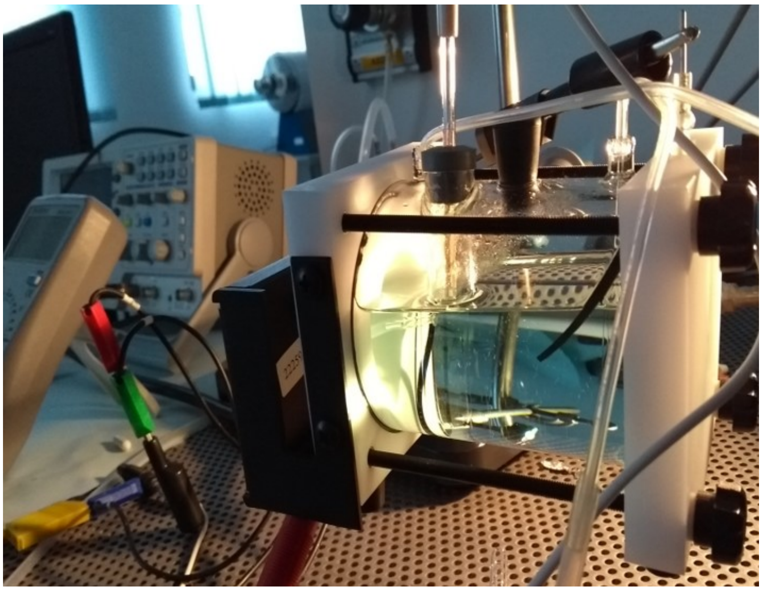

Figure 1.11: Electrodeposition system used at CNR-SPIN (Genoa, Italy).
Credits: Alessandro Leveratto, Emilio Bellingeri, CNR-SPIN (Genova). Electrodeposition process described in [26].

1.4 MgB_2 for the FCC-hh superconducting links

In this section, some general properties of MgB_2 are explored along with its typical wire manufacturing technologies, and the freeze-drying process (FDP) performed at CNR-SPIN.

1.4.1 General properties

MgB_2 is a type II superconductor with T_c = 39 K [84], which is lower than those of HTSs, but significantly above the value of the LTS Nb_3Sn (approx. 18 K) [35], [85]. It is a binary compound with simple hexagonal structure of AlB2 type, space group P6lmmm [86], [87], [49] which is quite common among borides [88], [89]. The structure is characterized by the superposition of graphitic-type boron planes separated by hexagonal planes of magnesium atoms. The dimensions of the unit cell are: $a = b = 3.084\,\text{Å}$ and $c = 3.522\,\text{Å}$, $\alpha = \beta = 90°$ e $\gamma = 120°$ [78]. B atoms form honeycomb planes, whereas Mg atoms are at the centres of the hexagons inbetween boron planes [90]. Similar to graphite, MgB_2 exhibits a remarkable covalent nature for B-B bonding between B atoms belonging to the same plane [91].The binary phase diagram for the Mg - B system, in the form known at the time of the discovery of the superconductivity of MgB_2 can be found in [92].
In Figure 1.12, a representation of MgB_2 crystal structure is shown.

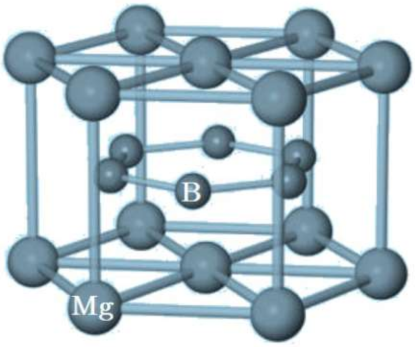

Figure 1.12: Crystal structure of MgB_2 showing Mg and B layers. As shown, small spheres represent B atoms and big ones represent Mg.
Figure adapted from [49].

1.4.2 Manufacturing process of MgB_2 wires

Most of the information in this section is based on [93], [35].

The Powder-In-Tube process (PIT) is a commonly used manufacturing method for long length production of wires. As the name of the technique says, the process starts with precursor powder and it is known to have two main routes: ex-situ, in which pre-reacted MgB_2 powder is inserted into a tube, and in-situ, where Mg and B powders are well mixed before being inserted into a tube. The MgB_2 phase is therefore formed during this heat treatment in this case.
Tubes are typically made of Ni, Monel, in some cases characterized by a Nb barrier and a Monel outer sheath [35]. In both methods, the filled tubes are deformed into single-core wires, which are then stacked into a multi-filament billet (as shown in Figure 1.13). After deformation of the billet into a wire, typically done by drawing, a heat treatment is performed. The purpose of this heat treatment is increasing the cross-section of the current path from grain to grain by sintering the powder grains (ex-situ process), and leading to MgB_2 phase formation (in-situ process, as previously mentioned).
Another technique used for the production of MgB_2 wires is the so-called ”internal Mg diffusion” (IMD). This method will only be mentioned, as the wires investigated in this work were produced by PIT (ex-situ): the related details can be found in [35] and [94].

The studied wires were manufactured by ex-situ PIT starting with a C-doped nanoboron (nB). An innovative B nanostructuration method was developed at CNR-SPIN in Genoa and patented in 2010 [36]. B plays a fundamental role in enhancing the superconducting properties of MgB_2 [95], [96], [36].
Their nB production method allows to homogeneously disperse a carbon source (in this case inulin and haemoglobin) into boron oxide (B_2O_3) molecules through the atomization of solutions in cryogenic liquids [36]. A homogenous dispersion of C in B_2O_3 solid

phase was achieved by freeze-drying process (FDP), which removed water. The nanostructured B_2O_3 was reduced to C-doped nB by magnesiothermic process [97], [98], [99]. For the wire preparation, 260 g of B_2O_3 powder was solubilized in 5 liters of deionized water, then atomized in liquid nitrogen. A dispersion of very small boric acid molecules (B_2O_3 + $3H_2O$) was thus obtained in equally small ice particles. To produce different C-doped powders, carbon sources (inulin, haemoglobin) were added and a homogeneous solution was obtained. The FDP was used to remove water from the frozen powders, and nanostructured B_2O_3 extracted from the freeze-drying machine was reduced to raw nB [97] through the Moissan process (reduction of boric oxide with Mg [100]). The reaction performed in stainless-steel crucibles at 800 °C for 5 h under Ar flow led to a mixture of pure nB, MgO, and unreacted B_2O_3. The purification phase is typically characterized by a sequence of leaching steps with hot hydrochloric acid. Finally, the product was dried in an electric oven at 80 °C for several hours to remove residual moisture.
The nB powders were stored and handled in a glove box under a pure Ar atmosphere (99.9999%) to avoid oxidation and contamination. Further information about nB production by FDP and magnesiothermic process are given in [36].

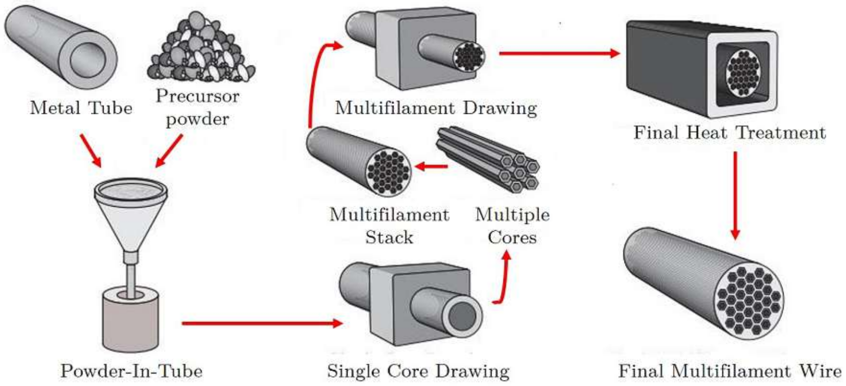

Figure 1.13: Schematic of the PIT process. The precursor powder can be pre-reacted MgB_2 (ex-situ strategy) or a mixture of Mg and B (in-situ strategy). *Figure adapted from [93].*

1.5 Outline of the thesis

In this manuscript, we presented the microstructural investigations by different electron microscopy techniques of Nb_3Sn as the material envisioned for the FCC-hh dipole bending magnets, Tl-1223 for the low surface resistance FCC-hh beam screen, and MgB_2 for the FCC-hh superconducting links. Most of the focus has been on Nb_3Sn.

In Chapter 2, *Sample preparation and characterization techniques*, we described the different sample preparation methods we used. An optimal electron microscopy analysis is impossible without a high-quality sample preparation. Furthermore, we presented the employed electron microscopy techniques by both SEM and TEM.

In Chapter 3, *Nb_3Sn for the FCC-hh superconducting magnets*, we presented and compared different layouts of IT Nb_3Sn wire in terms of Sn concentration gradient as this is one of the crucial factors influencing J_c enhancement. We focus on a layout type with cluster, which might lead to the production of more homogeneous wires. Moreover, we performed a preliminary analysis on size and density of the potential pinning centres (doping agents) in APC Nb_3Sn wires coming from different heat treatment. We also carried out a preliminary grain size study. The idea behind the investigation of these APC wires was to understand the influence of the heat treatment on the afore-mentioned parameters.

In Chapter 4, *Tl1223 for the FCC-hh beam screen*, we explored the microstructural features of Tl-1223 thin films produced via electrochemical deposition with the aim of assessing the formation of the desired Tl-1223 phase, the substrate coverage, and the connection between grains. These analyses set the stage for optimizing the manufacturing process of this still mysterious thallium-based superconducting material.

In Chapter 5, *MgB_2 for the FCC-hh superconducting links*, we characterized the microstructure of C-doped MgB_2 wires produced using C-doped nano-boron as precursor. We investigated C dispersion within the MgB_2 matrix to better understand the role of C as pinning agent with potential in terms of raising the J_c value.

A key point of this work is to understand how the variables involved in the manufacturing processes influence the material microstructural features, strictly connected to its superconducting properties. In this way, it would be possible to give the manufactures an effective contribution in terms of producing wires and films with enhanced superconducting performance.

This work is part of the european project EASITrain (European Advanced Superconductivity Innovation and Training), belonging to the CERN FCC international collaboration. This collaboration includes 135 research institutes and universities and 25 industrial partners from all over the world [101].
EASITrain is a Marie Sklodowska-Curie Training Network funded by the European Union's H2020 Framework Programme under grant agreement no. 764879. *"EASITrain establishes a well-balanced consortium, integrating complementary competencies of 6 universities, 5 research centers and 13 companies of different sizes, from complementary technical and industrial backgrounds"* [102].

2 Sample preparation and characterization techniques

This chapter describes the sample preparation methods and the different eletron microscopy techniques used for characterizing the microstructure of Nb_3Sn, MgB_2 and Tl-1223 samples.

2.1 Sample preparation

A good sample preparation is the main ingredient for obtaining an optimized electron microscopy analysis. According to the sample size and shape (wire for Nb_3Sn, MgB_2 and thin film for Tl-1223), the employed instrumentation (SEM or TEM) and the analysis type, different preparation techniques were used. Unlike sample preparation for TEM analysis, the one for SEM investigation does not require thinning of samples and it is therefore easier. Furthermore, many specimens being conductive do not need any specific preparation before SEM characterization. It must be said, however, that insulating materials do not bring any path to ground for the specimen current and may become electrostatically charged when exposed to the electron probe [103]. This problem can be solved by using a sputter coater to deposit a conductive layer (e.g. Au-Pd) on top of the sample surface. This being done, if the sample is drifting, two or more path lines connecting its surface to the ground (sample holder) can be drawn using a conductive paste (e.g. Ag paste). The TEM sample preparation typically involves the use of a Focused Ion Beam (FIB). This machine allows to prepare very thin lamella samples (thickness $\approx 100\,\mathrm{nm}$), which require several thinning steps at the final preparation stage, in order to optimize the quality of the TEM analysis. All TEM measurements in this work were performed on FIB lamellas.

2.1.1 Sample preparation for SEM analysis

The mechanical preparation represented by several grinding and polishing steps is one of the most commonly used method to prepare the sample surface for SEM analyses. Before starting the polishing process, the sample has to be mounted in a proper embedding system. In particular, the sample is first inserted in a suitable supporting tool and then positioned in a molder (red cylinder in Figure 2.1a). The latter is filled with a resin mixed with a hardener (or accelerator) to provide the embedding compound. Depending on the hardening agent, the polymerization process can take place at room temperature, if it requires a short curing time, or in an oven to speed up long curing processes. The final product looks like the object in Figure 2.1b and 2.1c.

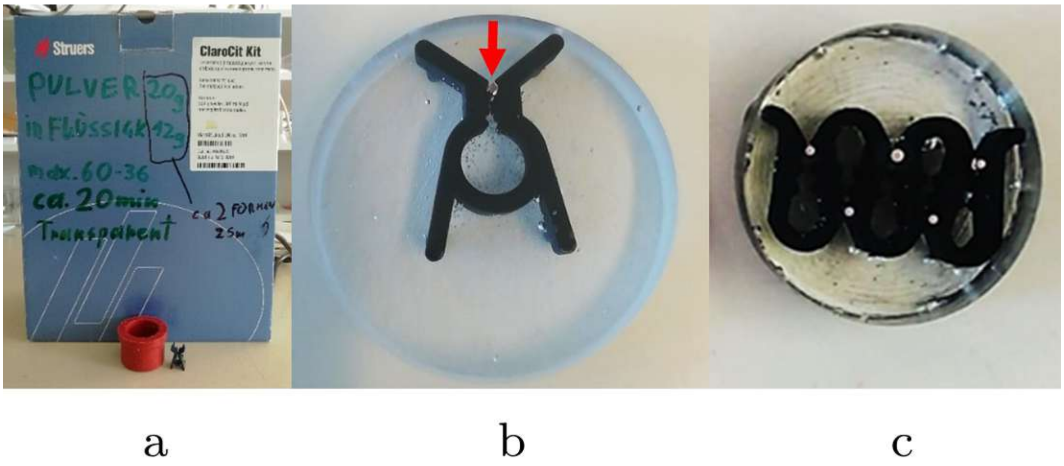

Figure 2.1: Typical embedding system: (a) box with embedding liquid and powder, red molder and embedding tool for holding the sample (black object); (b) one embedded wire (the red arrow shows the cross section of a wire); (c) five embedded wires whose cross–section is represented by the light spots.

Once the sample is embedded, it is ready for the fine grinding process. In particular, according to the embedding system size and shape, two different machines can be used. For the round shaped embedding system (d $\approx$ 4 cm) containing 4-5 wires (like the one shown in Figure 2.1c), an Allied MetPrep4 Grinding/Polishing machine was used (Figure 2.2a). All wires were mounted vertically in the holder, in order to prepare their cross section. This is the case of most of the Nb_3Sn wires analyzed and also of the MgB_2 ones. All wires embedded this way were first finely grinded by employing Silicon Carbide disks with grain size of 30 µm, 15 µm, 10 µm and 5 µm. The grinding times, depending on the disc grain size (the finer, the longer), were in the range between 15 s (for the coarsest discs) and up to 2 min (for the finest ones). All grinding steps were performed wet, under a steady flow of water, considering that water does not bring damage to the costituents of the material microstructure. The fine grinding was then followed by two polishing steps, perfomed with the same machine now supported by an additional device, an Allied AD-5 Fluid Dispenser as shown in (Figure 2.2b). The latter supplies diamond suspensions for the material final polishing, performed first on a 3 µm fabric disk for almost five minutes and then on 1 µm fabric disk for approximately ten minutes. Once the polishing process was finished, the embedded sample was cleaned by an ultrasonic cleaning machine, which simply uses water and air to wash and dry. As stated above, the described preparation method involved embedded systems containing up to five wires and intended directly for electron microscopy analyses. From now this method will be called „type A“. For some Nb_3Sn wires, intended first for scanning Hall probe microscopy (SHPM) measurements at TU Wien - Atominstitut (see Chapter 3), a disc of approximately 1 µm was cut from a multi-wire embedding system (similar to the one of Figure 2.1c) before starting the polishing steps. The thin disc was produced by using a Struers Accutom 50 precision cut-off machine. The wire pieces inside this disc were then isolated in single little squares (approx. 2 mm * 2 mm, according to the requirements for the SHPM machine setting), all cut by using a mini cut-off saw. The so separated embedded wires were then polished by using an Allied Multiprep polishing machine (Figure 2.2c) and different roughness Aluminum Oxide discs with grains of 9 µm at 125 RPM (rotations per minute), 6 µm at 100 RPM, 3 µm at 75 RPM and 1 µm at 50 RPM.Two other disks with grains of 0.5 µm and 0.1 µm were used together with lubricants for the final polishing steps. It must be said that in many cases these final steps did not bring any improvements to the cross–section of the Nb_3Sn wires: in fact, the different hardness of Nb, Nb_3Sn, Cu matrix and the typical presence of voids in the central region of the sub-elements reduce the surface quality during polishing, bringing scratches and smearing. From now on this method will be called „type B“. After being polished individually, each sample was cleaned in an acetone bath and mounted on the SEM stub (aluminum sample holder) using a carbon-based conductive adhesive tape. For the multi-wire system before described (type A preparation method), a dedicated metallic sample holder was used. Before starting the SEM analysis, the system consisting of sample and sample holder was inserted into a Quorum Q150T S Sputter Coater for the deposition of a 4 nm Au-Pd conductive layer.

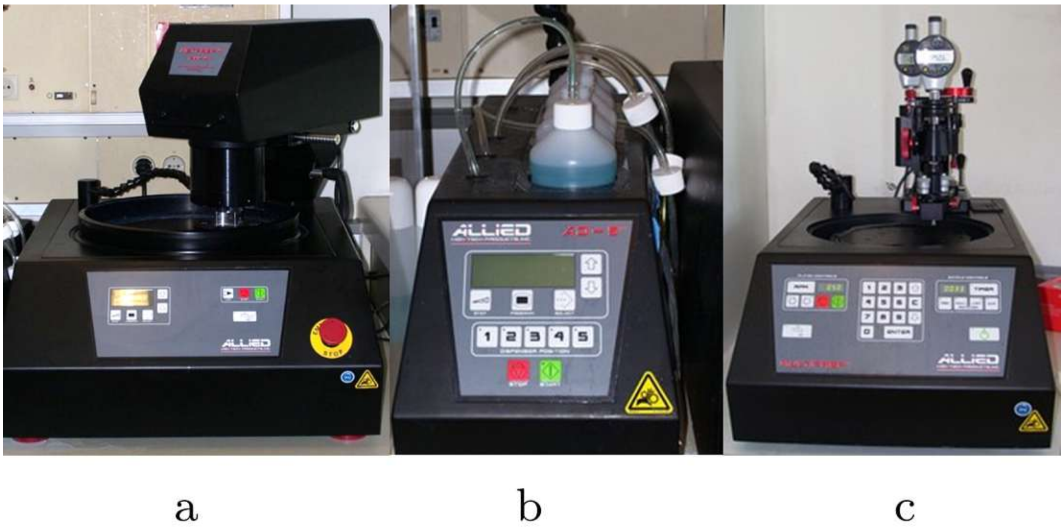

Figure 2.2: Grinding and polishing machines: (a) Allied MetPrep4 with an (b) Allied AD-5 Fluid Dispenser, both used for „type A“ sample preparation; (c) Allied Multiprep used for „type B“ sample preparation.

As for the Tl-1223 samples, they came in both pellet and thin-film form and no specific sample preparation was needed for their analysis. However, in an attempt to do an EBSD analysis, for a sample in the form of thin film, a Buehler Vibromet polishing system (Figure 2.3) was repeatedly used with different polishing times (1 h, 3 h, 18 h and 24 h). The Vibromet, being a vibratory polisher, removes minor deformation remaining after mechanical preparation, revealing the stress-free surface. This machine oscillates almost entirely horizontally, so as to maximize the time the sample is in contact with the polishing cloth. Silica suspensions are typically used as polishing liquid.

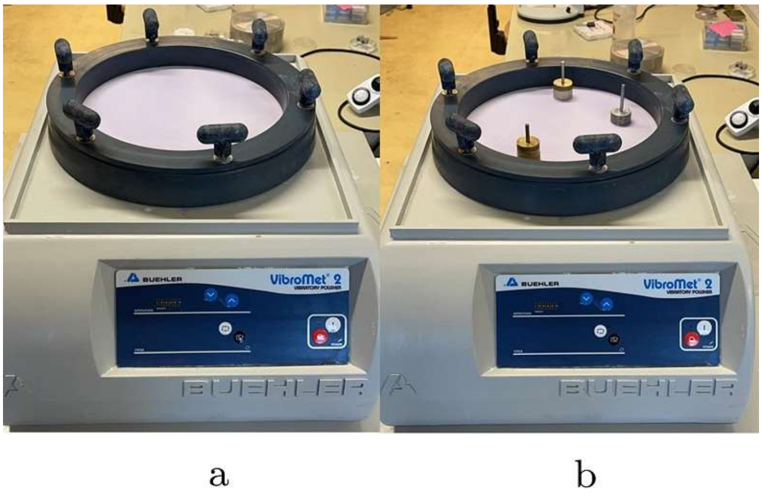

Figure 2.3: Buehler Vibromet polishing machine with (a) white fabric disk and (b) samples on it during the final polishing process.

2.1.2 Sample preparation for TEM analysis

As aforementioned, the samples intended for TEM analysis were prepared in the form of FIB-lamellas using the so called „lift-out“ technique. In particular, a FEI Quanta 200 3D DBFIB was employed. All materials analyzed with TEM were prepared using the same procedure.The main chamber of the FIB, intended to host the sample, is pretty similar to the one of a SEM: in this case, however, besides the electron column, there is a ion column. The entire process for the production of the lamella was monitored all the time by two screens, one from the point of view of the electrons (it works therefore as a SEM but with lower imaging resolution) and one from the point of view of the ions (in this case much more attention was paid to the voltage and current used in order not to damage the sample). Initially the stage with the sample holder containing the specimen was perpendicular to the electron column (0° tilt). After having identified the surface area for the cutting of the lamella, the stage was brought to 52°, hence perpendicular to the ion column (according to the configuration of the used machine). Once selected a proper area of the sample surface for cutting the lamella, a protective layer of Pt was deposited on top of it and hence on a region with dimensions of approximately 25 µm × 3 µm (length × width). After selecting a voltage of 30 kV in the ions screen-window, a current of 0.1 nA was chosen for depositing a first Pt protective layer of 300 nm and then a current of 0.5 nA to deposit a second protective layer of 3 µm. A focused beam of gallium ions was then used to etch away the regions around the protective layer, so as to begin to shape the lamella. Specifically, three areas around the sample were selected for material removal (as shown in Figure 2.4) and the first cuts were made by setting the voltage to 30 kV and the current to 20 nA.

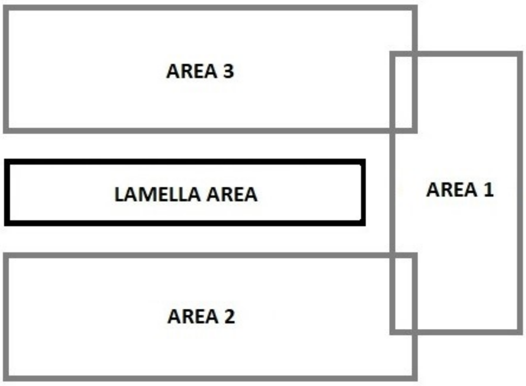

Figure 2.4: Schematic of the three regions selected to remove material surrounding the chosen lamella area (approx. 25 µm × 3 µm (length × width)).

The sample tilting degree (52°) was mantained to remove material from the area 1 (Figure 2.4). For the areas 2 and 3 the stage was further tilted by 8° with respect to 52° (best choice based on the experience of the most frequent users), thus working first at 44° and then at 60° to cut out a wedge shape. Once the three cuts were produced, other material was etched away with a current of 7 nA until the lamella became „free“, i.e. bound to the original sample on one side only and thus ready to be lifted. The process for the preparation of a FIB lamella described so far is well represented in 2.5(a,b,c). A micro-manipulator was first glued by tungsten to the free side of the lamella (see Figure 2.5d) and, after removing about 1 µm of material joining sample and lamella, the latter was moved away and attached to the sample holder (Figure 2.5e and 2.5f). This sample holder is a half ring with a diameter of 3 mm, showing three tiny vertical supports (Figure 2.6) and mainly made of Mo. Only in few cases a Cu sample holder was used. The reason why Mo was generally favoured over Cu is that during post-FIB ion thinning (often required depending on the type of analysis to perform), Cu from the sample holder can be sputtered onto the sample itself causing contamination. Once the lamella was attached to the sample holder, it was further thinned by using an initial current of 3 nA, gradually reduced down to 0.3 nA. Figure 2.5f shows one of the early phases of thinning. For lamella thicknesses of 200-300 nm, the final thinning step (aiming at reaching a thickness of 100 nm or even less) was either carried on with the FIB using very low currents or with a precision ion polishing system (model Gatan Inc. PIPS II), a machine that uses two Ar ion beams to thin the lamella from two opposite sides. In the latter case the following settings were generally used: an acceleration voltage of 1 kV-2 kV, a current of approximately 5 μA, a tilt angle of 8°-10° and a process time of 30–60 minutes. The best results were achieved by using higher angles and lower voltages as well as by cooling down the system with liquid nitrogen during the milling process. It is important to note that having a thin lamella (100 nm thick or less) is critical to achieve the best quality TEM analysis. Nevertheless, depending on the sample material and the properties to be explored, a thickness of about 200 nm may also be adequate (more details will be given in the next paragraphs).

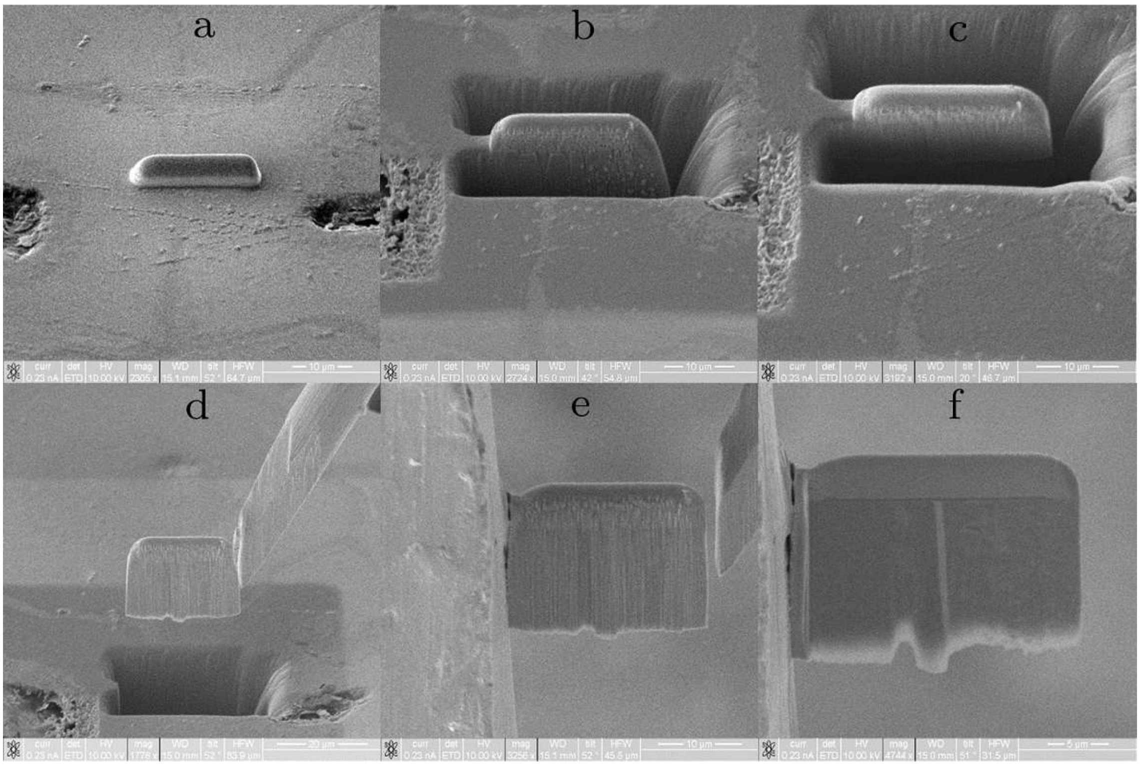

Figure 2.5: FIB-lamella preparation steps: (a) Pt protective layer deposition; (b) material removal from three areas sorrounding the region of the future lamella; (c) shaped lamella bound to the original sample on only one side and now ready to be lifted; (d) micro-manipulator lifting up the lamella and (e) attaching it to the sample holder; (f) a early step of the lamella thinning process.

Figure 2.6: A typically used Mo FIB-lamella sample holder.
Source: Microtonano.

2.1.3 Sample preparation for XPS analysis

The samples foreseen for X-ray Photoelectron Spectroscopy (XPS) were first prepared at USTEM, and then analyzed at Analytical Instrumentation Center (AIC), TU Wien (see Chapter 3). The chemical composition and bonding environments of differently prepared Nb3Sn wires embedded in a conducting graphite based mounting powder were to be assessed. Particular emphasis was to be put on the Sn/Nb ratio and possible differences between samples. The samples were received as dark grey pellets (approximately 10 mm in diameter, 1-2 mm in height) with the wire sample embedded in the disc center. Samples were fixed to the sample holder using double-sided Cu tape.

2.2 SEM analysis

All scanning electron microscopy (SEM) analyses were performed using a FEI Quanta 250 FEGSEM. This machine is equipped with energy-dispersive X-ray spectroscopy (EDX) detector (EDAX SDD Octane Elite 55), electron back scattered diffraction (EBSD) detector (high speed Hikari CCD EBSD Camera), an Everhart-Thornley detector for secondary electrons (SE) and a back scattered electron (BSE) detector. Both electon types, secondary and back scattered, were used to produce images. In the next subsections, a more detailed description of the employed SEM investigation techniques will be given.

2.2.1 Imaging techniques: SE and BSE

A good quality image is a crucial factor for the sample characterization, since it allows the most interesting parts of it to be more deeply explored. Though SE and BSE different information about the sample are obtained: the former give an idea of the sample surface topography. In particular, they are low energy (E) electrons (E $\geq$ approx. 50 eV) coming from the inelastic interactions between the primary beam and the sample atoms within the first few nanometers (approx. 10 nm) below its surface. More secondary electrons can escape the sample surface from edges and slopes rather than from flat areas and, of course, dimples: more signal is hence produced from edges and slopes and this is the reason why SE lead to images giving information about the surface topography. The location of the detector also plays an important role in this respect. It is usually positioned at an appropriate angle to optimize the detection of secondary electrons. However, sample edges and slopes that are not facing the direction of the detector will produce less signal. Surface features facing the direction of the detector will appear particularly bright. The BSE produce instead high contrast images which reflect the compositional differences in a specimen. They are high energy electrons (E $>$ approx. 50 eV) coming from the elastic interactions between the primary beam and the atoms nuclei in a region up to $\sim 1\,\mu\text{m}$ below the specimen surface. They are closely related to the atomic number of the elements (Z). In particular, electrons are backscattered stronger at heavy elements (high Z) comaperad to lighter elements (low Z). Thus, areas containing heavier elements appear brighter in the BSE signal. The gray scale cotrast of the image is thus what gives an approximate idea of the elemental composition. BSE were preferred for imaging the Nb_3Sn wire cross-sections, since a clear differentiation among the sub-element phases is fundamental for the wire characterization. Electron channeling imaging is also possible through BSE. It is an effect of the interaction of the primary beam electrons with crystalline materials, typically used to detect the crystallographic properties of a sample in an SEM image [104]. The orientation of the beam relative to the arrangement of atoms in the crystal affects the interaction of the beam electrons with the bulk sample and the resulting outputs [104], so helping for example the investigation of lattice defects close to the surface.

As the SE detector is known as "Everhart-Thornley detector", we will refer to it as "ETD". For BSE, we will simply use "BSE detector".
In Figure 2.7 a SE (a) and a BSE (b) image of a typical Nb_3Sn wire cross-setion are shown.

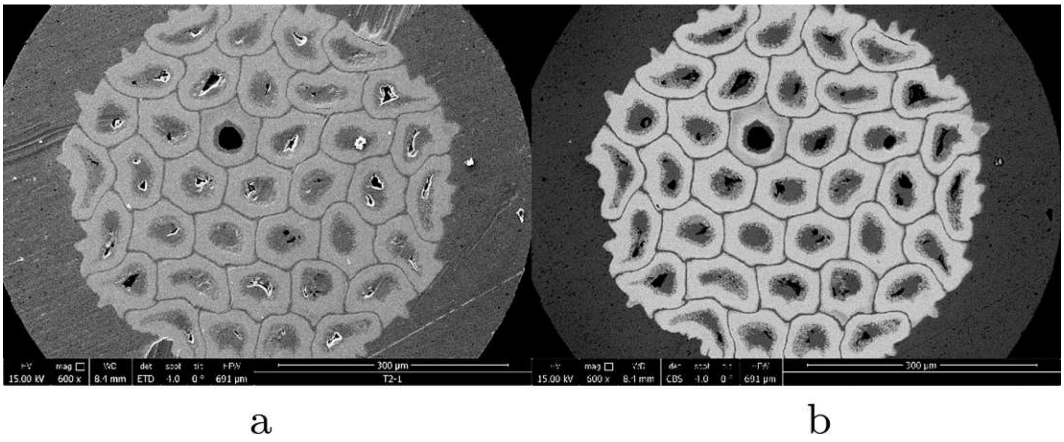

Figure 2.7: Same magnification SE (a) and BSE image (b) of a typical Nb_3Sn wire cross-setion.

2.2.2 Energy Dispersive X-ray Analysis (EDX)

The energy-dispersive X-ray spectroscopy (EDX) method allows to analyze the distribution of the chemical elements in a sample and it's strictly related to the characteristic X-rays production process: an electron belonging to an atomic inner shell is removed by an electron of the primary beam, so a vacancy is left. The atom is ionized and thus in excited state. The atom regains stability when an electron of the outer shells fills the vacancy, and an X-ray photon is emitted.The emission energy of such X-rays is characteristic of the difference in energy of the two electron shells involved, so providing a distinctive way to identify the atom type in the material.The produced X-rays are collected by a detector based on a semiconductor device (usually a crystal of silicon) and their energy is dissipated by the creation of electron-hole pairs in the semiconductor crystal. A high bias voltage applied across the crystal allows a charge signal to be produced, which is then transmitted to the pulse processor for further analysis. Figure 2.8 shows a schematic of a characteristic X-ray production and collection by EDX detector.

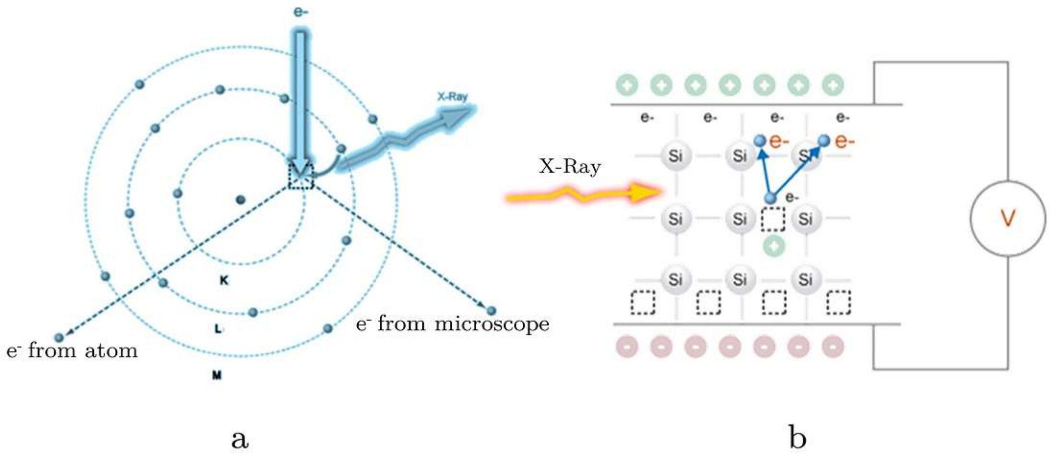

Figure 2.8: Schematic of (a) a characteristic X-ray production and (b) collection by a typical EDX silicon drift detector (SDD). *Adapted from Myscope.training: characteristic-production and detection-silicon.*

The intensity of the signal is proportional to the energy of the incoming X-ray. The pulse processor removes noise by averaging the signal received. The time spent averaging the signal can be varied by adjusting the time constant or process time of the detector system. Longer process time means the signal is averaged for longer and spectral peak resolution improves. However a longer process time also increases the so-called ”dead time” of the system. This is a parameter influencing the duration of the EDX spectra or maps acquisition. A high dead time implies that the pulse processor takes too long to analyze a certain signal, so it misses the next incoming one. In a typical EDX spectrum (Figure 2.9), sharp peaks are exhibited corresponding to the characteristic X-rays emitted by the atoms of the different elements present.

Further details about the performed SEM-EDX measurements will be given in the chapters related to each characterized material (Chapters 3, 4, 5).

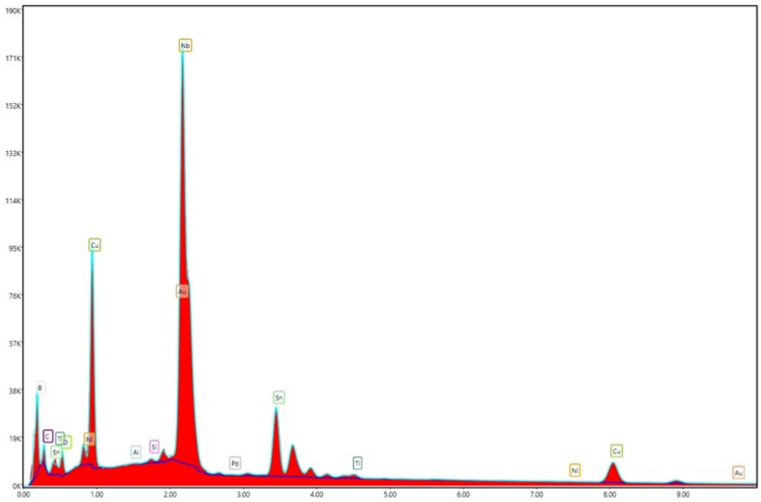

Figure 2.9: A typical EDX spectrum showing the number of X-rays detected versus their energies. The red spectrum stems from EDX measurements performed on a Nb_3Sn sample. The light blue line tracing the spectrum profile represents its fit.

2.2.3 Transmission Kikutchi Diffraction (TKD)

Transmission Kikutchi Diffraction (TKD), or Electron Backscatter Diffraction (EBSD) "in transmission mode", is a technique allowing the evaluation of grain size and orientation. According to classic EBSD, when an electron beam is diffracted by the surface of a crystalline material, in bulk-sample form, diffraction patterns are produced on a phosphor screen. The patterns reflecting the underlying crystal structure are thus recorded. In the case of TKD, thin specimens (e.g. FIB lamellas) are required, since they need to be electron transparent. A thin sample (below 100 nm) offers the advantage of higher spatial resolution, which is crucial for resolving and analyzing small grain sizes such as those of Nb_3Sn. In fact, depending on the manufacturing process and heat treatment, this material can have a grain size on the order of 20 nm. This topic will be further discussed in Chapter 3. TKD measurements are typically performed in SEM systems with an EBSD camera by using a specific sample-holder suitable for very thin samples. So, the technique working principle is the same as for EBSD, but the sample thickness and the experimental set-up are different: Figure 2.10 gives a general idea about the set-up differences between TKD and EBSD. More information about these techniques can be found in [105] and [106].

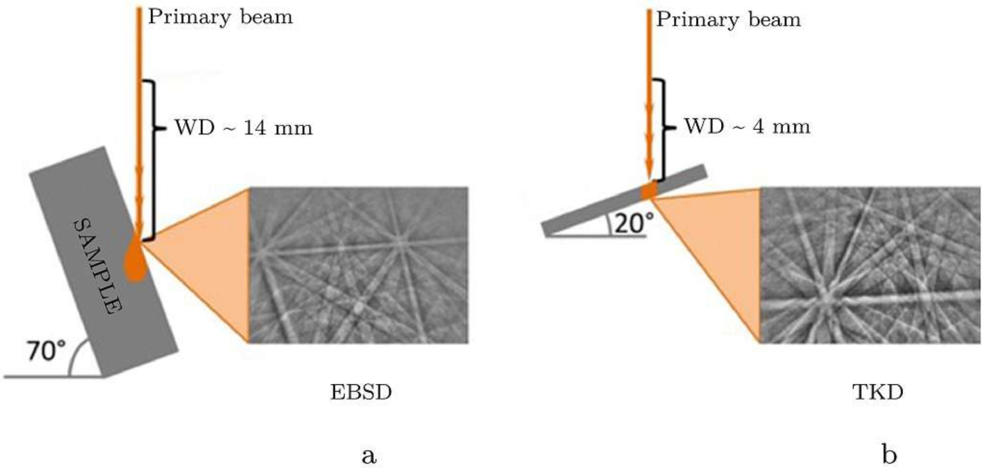

Figure 2.10: A typical example of experimental configuration for EBSD (a) and TKD (b) measurements. Note that WD is working distance, the distance between the lower pole piece of SEM system (where objective lens is located) and the sample. Specifically, it is the distance at which the image is focused and is varied depending on the type of analysis being performed and depending on the SEM configuration being used. *Adapted from Liang et al. [106].*

2.3 TEM analysis

The scanning electron microscopy (TEM) analyses were performed using a FEI TECNAI F20. Among its several components, this machine is equipped with a EDAX Apollo XLTW SDD detector for EDX and a GIF (GATAN imaging filter) Triediem camera, a setup of electron energy imaging filter which can be used to acquire EELS (electron energy loss spectra) by collecting dispersed electron spectra on a CCD camera. This TEM can be operated in two different ways: normal TEM and STEM (scannining-transmission electron microscope) mode. In the first case, the current flowing through the microscope electromagnetic lens coils is such that the electron beams are focused perpendicular to the plane of the sample, so they are parallel as they penetrate the sample. Through this operation mode bright field (BF) and dark field (DF) images can be obtained as well as high resolution (HRTEM) images by increasing the magnification. Under TEM operation conditions diffraction patterns can be recorded by selecting the proper apertures in the back focal plane of the objective lens. As for STEM, the current in the electromagnetic lens coils is changed is such a way that the elctron beam is focused into a narrow spot. The transmitted signal comes from different sample points according to the beam movement across the specimen itself, which is scanned as typically done with SEM. HAADF (high-angle anular dark-field) detector is used for achieving high contrast STEM imaging. More details about the imaging techniques used in this work will be given in the next subsection.

2.3.1 Imaging techniques: BF, DF, HRTEM, HAADF

This subsection describes the employed TEM imaging techniques.

2.3.1.1 TEM imaging: BF, DF, HRTEM

The main difference between BF and DF images is related to which electron type is selected for producing the image. BF is the most commonly used imaging technique with TEM and takes advantage of the transmitted electrons to create the image: non-scattered electrons are in fact selected by an objective aperture and the scattered ones are blocked. Considering a sample with uniform thin thickness (100 nm or less), crystalline regions and those with high mass material will appear dark, while vacuum and amorphous areas will appear bright. On the other hand, DF images are constructed from scattered electrons and usually have high contrast, which is useful for analyzing crystal lattice details, grain boundaries, grain size and shape, and so on [107],[108],[109]. Figure 2.11 shows an example of bright field (a) and dark field (b) image.

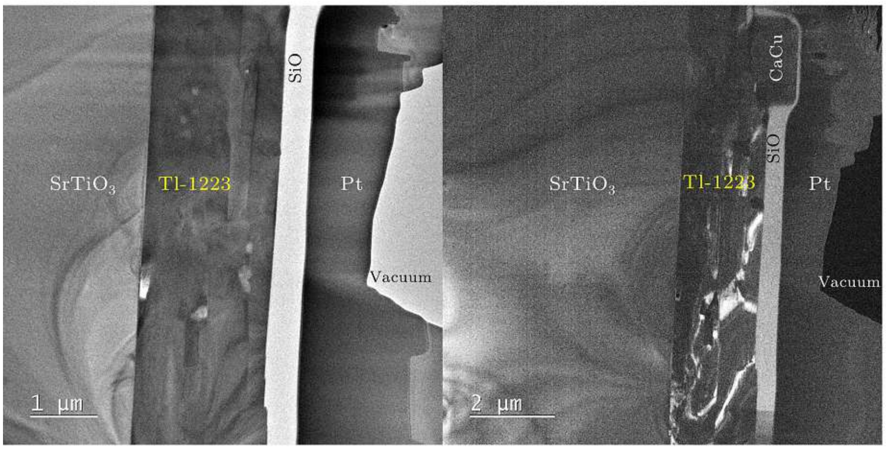

a b

Figure 2.11: FIB lamella cut from a Tl-1223 thin film deposited on a SrTiO$_3$ substrate: the same sample is shown in a BF image (a) with a magnification of about 6000x and a DF image (b) with a magnification of about 3000x. The lower magnification in (b) gives way to observe the various details (grain size, defects, etc.) across the film of Tl-1223.

HRTEM ist used for imaging the atomic structure of the sample, its lattice distances, interfaces with atomic resolution, defect and small precipitates. For this purpose magnifications in the order of 10^5 are employed. Contrarily to the former described BF and DF imaging techniques, no objective aperture is inserted into the back focal plane of the objective lens. Thus, all Bragg scattered electrons can act as coherent electron sources forming an interference pattern in the image plane of the objective lens. Because of the fact that the Bragg scattered electrons are scattered at the lattice planes, the reulting interference pattern represents the lattice plane distances, eventhough the intensity distribution depends on some other parameters, like the focus setting or the sample composition and thickness. An example of HRTEM image is shown in Figure 2.12. In this work, the HRTEM imaging technique was used for precipitates analysis in MgB_2 wires.

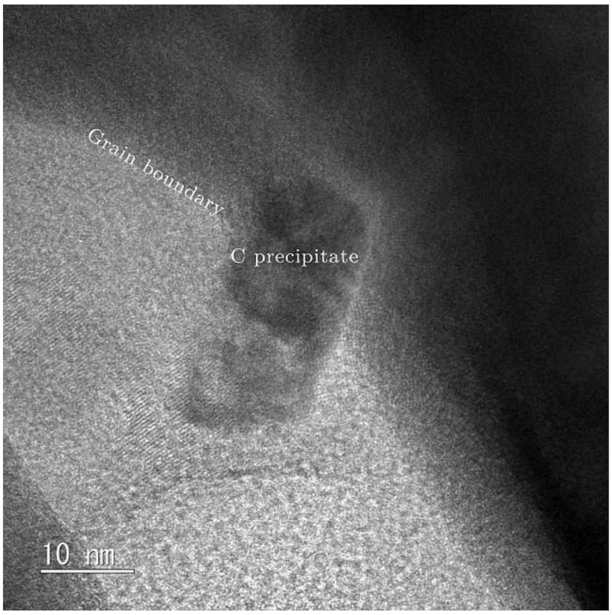

Figure 2.12: Example of a HRTEM image showing a C precipitate between two MgB_2 grains.

2.3.1.2 Imaging in the scanning mode of the TEM (STEM)

When operating the TEM in the scanning mode (STEM), the intensity in the diffraction plane is recorded with respect to the beam position scanning across the sample. In general, there are three different signals available: (i) the intensity in the central diffraction disc, which would give an Bright Field image. (ii) the collective intensity in the Bragg scattered electrons, which are detected using a ring-shaped detector circumfering the bright field detector. Such an image is called annular dark field (ADF) image. (iii) the collective intensity of Rutherford scattered electrons by employing a ring-shaped detector, too. Contrarily to the ADF detector, which collects electrons scattered at the crystal lattice and thus scattered to small angles, only, the Rutherford scttered electrons are scattered to large angles and the respective detector is an high-angle ADF (HAADF) detector. RUtherford scattering happenes when a swift electron passes by the nucleous potential. Consequently, its deflection depends on the strength of this potential and therefore on the atomic number Z. The HAADF-signal is therefore called Z-contrast, too [110],[111]. In this work, Z-contrast imaging is used for analyzing the density of dopants in teh APC-Nb3Sn matrix with respect to the varying heat treatment of several samples.

2.3.2 STEM-Energy dispersive X-ray analysis (EDX) and STEM-electron energy loss spectrometry (EELS)

Energy dispersive X-ray analysis (EDX) and electron energy loss spectrometry (EELS) measurements were both performed in STEM mode, since its spatial resolution depends on the size of the chosen scanning electron probe. They are complementary techniques that give a complete view of the elemental composition of the material. Additionally, the ionization edge fine structure in EELS strongly depends on chemical bonding and thus on the atoms valence state. In both techniques, the signal comes from inelastic scattering of electrons as the primary beam passes through the sample. The EDX working principle is the same described above for SEM analysis. The EDX detector is positioned in the vicinity of the sample for collecting characteristic X-rays. To optimize signal collection, according to our TEM configuration, the sample is typically tilted about 20° towards the detector direction. EELS is based on the energy distribution of the electron beam that has been scattered inelastically while passing through the sample. Due to the fact, that the inealstic scattering cross section [12,13] becomes smaller with increasing ionization edge energies and because heavier elements have their main ionization edges at higher energies, EELS works best for lighter elements. Contrarily, EDX performs better for heavier elements, because the X-ray yield increases with increasing atomic number Z. Electrons which have interacted with the outer-shell electrons of the sample atoms have low energy losses (< 50 eV) and bring information about the optical properties of the material. The low losses can also be employed for determining the sample thickness with respect to the inelastic mean free path length within the probed sample area. $\frac{t}{\lambda} = ln(\frac{I_0}{I_{ZLP}})$ with t being the sample thickness in nm, λ being the mean free path length (in nm), I_0 being the total incoming intensity, and I_{ZLP} as the intensity in the zero loss peak (ZLP). Measuring thickness in different areas of the sample is crucial when it comes to evaluating parameters such as particles density. The section on APC-Nb_3Sn wires (Chapter 3) will discuss this topic in more detail.

2.4 Scanning Hall probe microscopy (SHPM)

The local properties of Nb_3Sn wires with standard and three-cluster layout (see Chapter 3) were evaluated by Scanning Hall probe microscopy (SHPM) remanent-field scans at Atominstitut, TU Wien. In this way, the influence of the wire geometry on the local currents (local J_c values) through the cross-section was evaluated. Scanning a Hall probe across the surface of a superconductor allows a magnetic field map to be recorded. Remanent-field scans require the magnetization of the sample resulting in a spatially resolved map of the remanent magnetic field. Such magnetic field maps offer the opportunity to extract the current flow inside the sample by means of inversion of the

Biot–Savart law. This analysis depends on several parameters related to the machine configuration, and it is as accurate as the prepared sample is thin. We also carried out Meissner-state scans to infer the Sn concentration gradients through the evaluation of the sub-element radial-T_c distributions, and compare the obtained results to the SEM-EDX Sn gradients. This is possible by analysing the shielding effect of the sample at different temperatures. Such a shielding effect was measured by applying a field below B_{c1} of the superconductor at a fixed temperature. The SHPM device is operated in a helium flow cryostat, and this is why measurements covering a wide temperature range are enabled.

As described at the beginning of this chapter, the specimens intended for SHPM measurements were prepared by method B and the final polishing step was carried out until a thickness of 0.8 mm was reached.

Other information about this magnetometry-based technique can be found in [112], [20].

2.5 XPS analysis

The XPS investigation was carried out thanks to tge collaboration with AIC (TU Wien). XPS is a non-destructive surface analysis technique that provides information about elemental composition, chemical and electronic states of a material. This technique consists of illuminating the sample with X-rays that have enough energy to eject electrons (known as photoelectrons) from the material atoms. Such electrons are emitted from the top 1-10 nm of the specimen being analyzed. As ejected electrons are counted over a range of electron kinetic energies (depending on the X-ray photon energy and the electron binding energy), a spectrum of photoelectrons is produced. In particular, when atoms emit electrons of a particular characteristic energy, peaks appear in the recorded spectrum. The photoelectron peaks with their energies and intensities allow the identification and quantification of surface elements (except hydrogen). More information on this electron spectroscopy method can be found in [113], [114].

3 Nb_3Sn for the FCC-hh superconducting magnets

3.1 Standard and cluster Nb_3Sn wires

We investigated prototype internal tin (IT) Nb_3Sn wires developed by TVEL and the Bochvar Institute in Russia. Microstructure, chemistry and its superconducting performance were of interest and are described in the subsequent section. Table 3.1 and Figure 3.1 provide general information about the analyzed wires and a view of the sub-element structures, respectively.

Wire	T4: standard	T3: three-cluster	T7: six-cluster	T8: six-cluster
Wire Ø [mm]	0.7	0.7	0.7	0.7
Heat treatment	210 °C, 50 h 400 °C, 50 h 665 °C, 50 h	210 °C, 50 h 400 °C, 50 h 665 °C, 50 h	200 °C, 24 h 380 °C, 50 h 570 °C, 112 h 660 °C, 100 h	380 °C, 48 h 580 °C, 48 h 700 °C, 92 h

Table 3.1: Overview information about the studied wires.

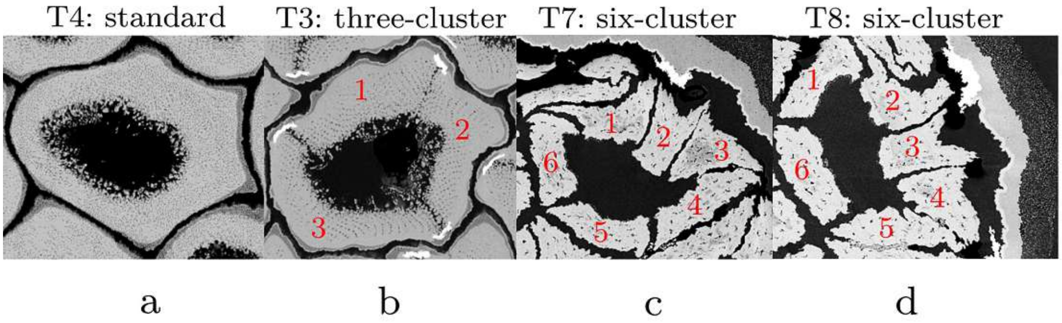

Figure 3.1: SEM BSE images of the sub-element structure for the standard wire T4 (a), three-cluster wire T3 (b), and six-cluster wires T7 (c) and T8 (d).

3.1.1 Purpose of microstructural characterization

We compared a sample with a standard layout and one with a three-cluster layout coming from the same heat treatment, and two samples with the same six-cluster layout coming from different heat treatments. Figure 3.2 shows the schematics of a cluster sub-element, more precisely a three-cluster sub-element, and of a standard one before heat treatment (a). The overviews and differences of the two wire types after being heat treated are compared in Figure 3.2b. The starting sub-element of a typical IT wire is characterized by a Cu matrix uniformly covered by Nb rods and showing a Sn core. As described in Chapter 1, the formation of the Nb_3Sn phase in possible due to a diffusion process activated by a proper heat treatment. If we think of this diffusion process, we can notice that the cluster layout has "free" ways for Sn diffusion from the core to the peripheral Nb barrier as the copper matrix (blue) is not entirely covered by the Nb filaments. This consideration is what we primarily focused on, as explained later on in this section. T4 and T3 samples, coming from the same heat treatment and showing a standard and a three-cluster layout respectively, are shown in Figure 3.3. Both wires present a Nb barrier distributed along the peripheral area of the sub-elements. Table 3.2 compares their main features. T7 and T8 with their six-cluster layout are displayed in Figure 3.4. The layout of the sub-element before heat treatment is the same as the three-cluster layout shown in Figure 3.3a as an example but shows six "free" paths for Sn diffusion to the periphery of the sub-element itself. The main features of T7 and T8 are presented in Table 3.3. The sub-elements of these wires do not exhibit a distributed Nb barrier over the peripheral region. In fact, these wires show a common Nb barrier that "packs" all sub-elements and is characterized by Ta insertions.

As visibile in the schematic of Figure 3.2, for cluster wires Cu rods were used to split each sub-element into cluster regions. This is, in fact, the case in sample T3, where exactly three Cu rods per sub-element result in its division into three clusters. These Cu separator inserts terminate with a bent sheet of Ta at the peripheral Nb barrier, to avoid it reacting and forming a continuous ring of Nb_3Sn [115]. The Ta sheets also prevent Sn from diffusing to the Cu stabilizers separating the wire sub-elements. For the T7 and T8 cases, six Cu separator inserts were used to split each sub-element into six clusters. Since the sub-element does not have a distributed Nb barrier, the bent Ta sheets are here located alongside a Cu-Nb shell (Figure3.4), interposed between the sub-elements region and the Nb common barrier (to improve the deformability of the latter)[116].

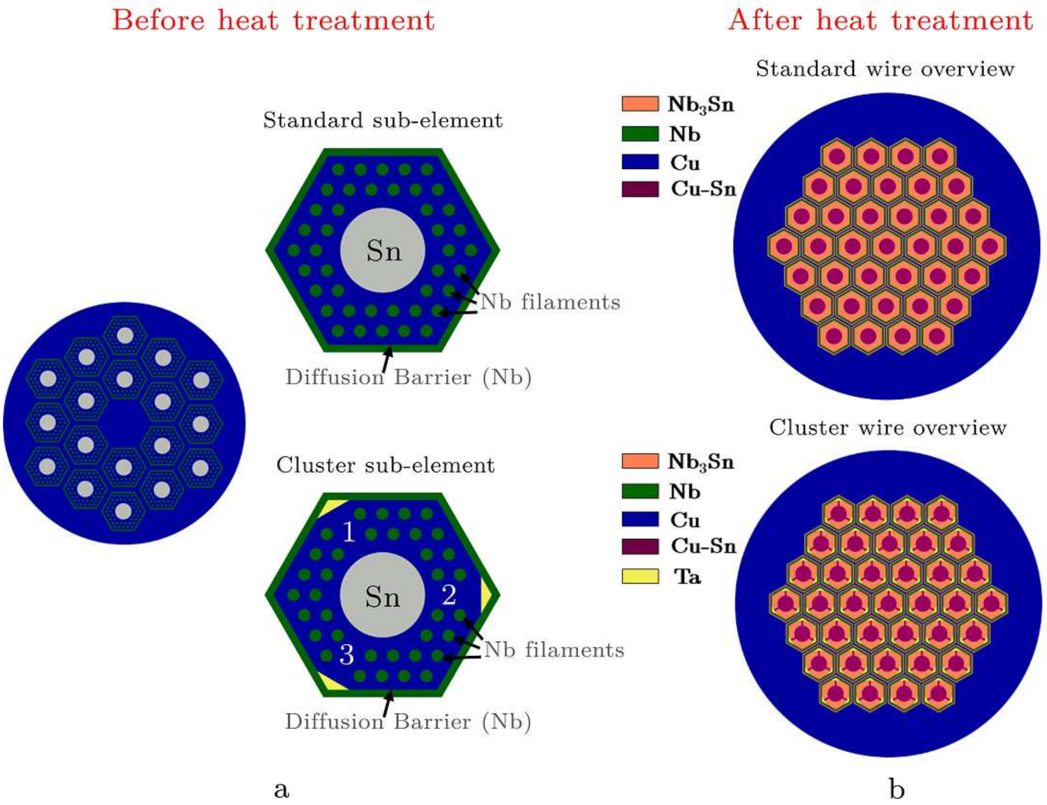

Figure 3.2: Standard and cluster sub-element layout before heat treatment (a) and overviews of a standard and cluster wire after heat tratment. The schematic of standard sub-element pre-heat treatment and standard wire post-heat treatment resembles the T4 configuration. The schematic of cluster sub-element pre-heat treatment and cluster wire post-heat treatment resembles the T3 configuration.

Why a cluster configuration? The main reason for dividing the sub-element into clusters is to reduce the ”effective” sub-element size, d_{eff}, and magnetization effects. The parameter d_{eff} corresponds approximately to the diameter around which a continuous superconducting path exists and it plays an important role because it affects the field quality of the final magnet. Previously, other research groups aimed at demonstrating the effectiveness of cluster layouts to reduce d_{eff} and magnetization effects, starting with B. A. Zeitlin, E. Gregory et al. [117], [118], [119] and up to P. A. Lukyanov et al. [116], who recently investigated wires with a six-cluster layout like T7 and T8. A. K. Gosh et al. studied cluster wires with a six-cluster layout and Nb barrier with Ta insertions distributed over the sub-elements peripheral area (a sort of mix of T7/T8 and T3 layouts). In their work, they confirmed the efficacy of cluster configurations for reducing magnetization in the analyzed strands, and their potential in reducing d_{eff}[115]. In the present work, we wanted to explore the potential of cluster layouts in terms of reducing the Sn concentration gradient over the wire cross-sections. Among people working on Nb_3Sn, it is well known that the reduction of Sn concentration inhomogeneities highly contributes to the J_c enhancement: the Nb_3Sn wires are in fact subjected to compositional gradients due to their production method, which influences their superconducting performance [18], [19], [20]. Therefore, this study focuses on the impact of the cluster configuration on the wire homogeneity in terms of Sn concentration gradient. Specifically, the Sn concentration gradient in the three-cluster layout (T3 in Figure3.3b) was investigated and compared to that of the standard one (T4 in Fig. 3.3a). As before mentioned, three-cluster layout means three free routes for Sn to diffuse through the Cu matrix during the heat treatment: it seems thus reasonable to think that these Nb-free pathways could help Sn homogeneously distribute over the wire cross-section. Moreover, such a configuration may lead to higher Sn content in the peripheral region of the subelement, which is usually Sn poor. By analyzing and comparing the same layout wires T7 and T8, produced with different heat treatments, we wanted to face the inhomogeneity issue from another perspective. We were also interested in understanding the role of a six-cluster layout in producing more homogeneous wires, considering the presence of six Nb-free pathways in this case. SEM and TEM microstructural characterizations helped us gain an initial insight into the role of cluster configurations in improving wire homogeneity.

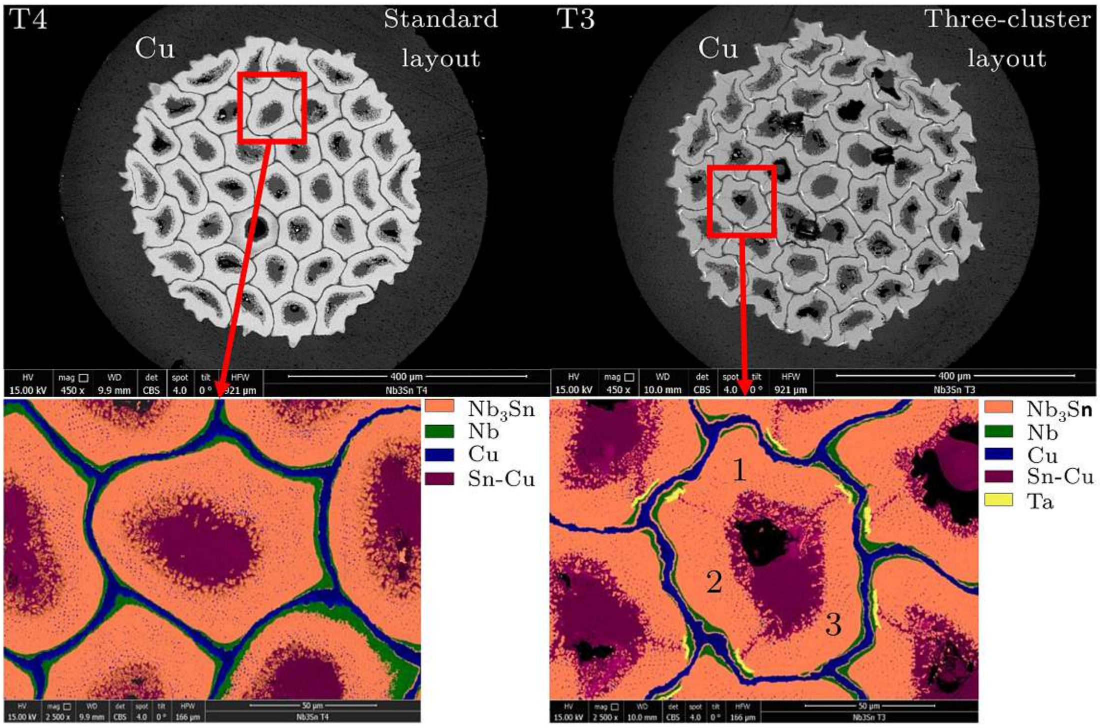

a b

Figure 3.3: SEM images of a standard (a) and a three-cluster (b) layout showing the wires overview (top) and the sub-element details (bottom). These images were taken with the BSE detector. The sub-element features were coloured by using the GIMP program to better differentiate the different phases.

Wire	Standard [T4]	Three-cluster [T3]
Wire Ø [mm]	0.7	0.7
Barrier	Distributed Nb	Distributed Nb + Ta-insertions
Dopant	Ti	Ti
Sub-elem. Ø [μm]	80	80
Sub-elem. Nr.	80	80
Heat treatment	210 °C, 50 h	210 °C, 50 h
	400 °C, 50 h	400 °C, 50 h
	665 °C, 50 h	665 °C, 50 h

Table 3.2: Characteristics of standard (T4) and three-cluster (T3) wires analyzed.

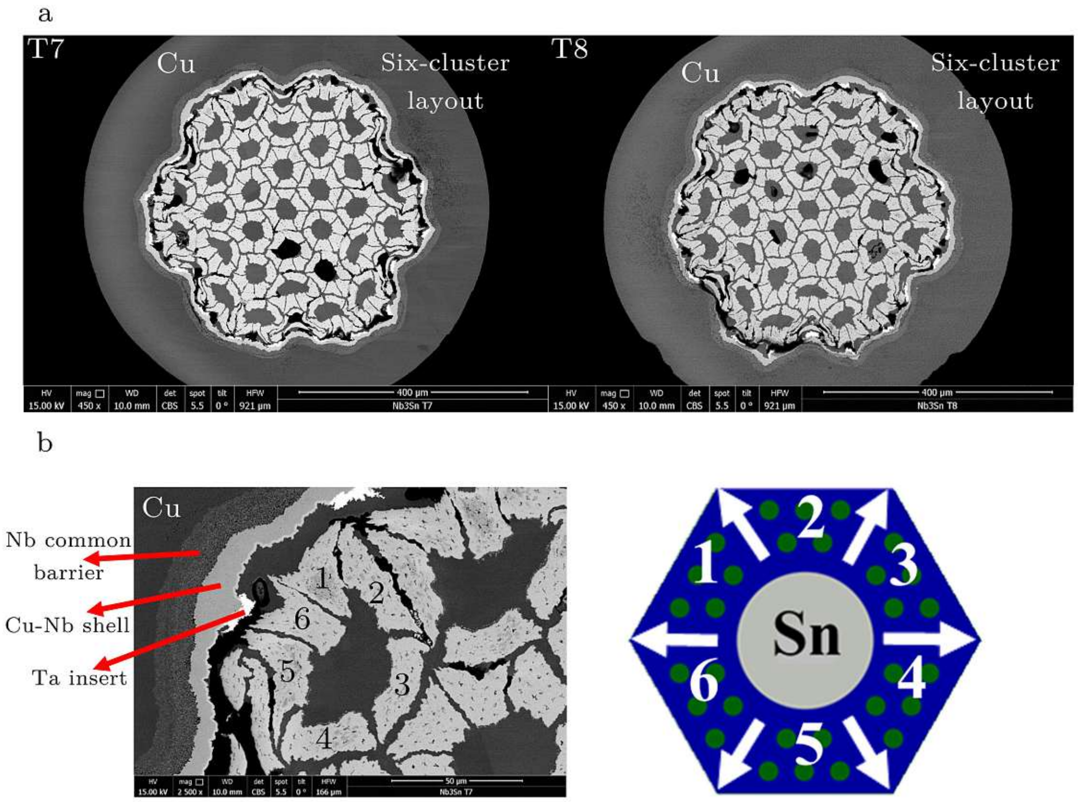

Figure 3.4: SEM images of (a) T7 (left) and T8 (right) six-cluster configuration, and (b) of the sub-element details. Next to it is a schematic of the initial sub-element (before heat treatment). These images were taken with the BSE detector.

Wire	Six-cluster [T7]	Six-cluster [T8]
Wire Ø [mm]	0.7	0.7
Barrier	Common Nb + Ta-insertions	Common Nb + Ta-insertions
Dopant	Ti	Ti
Sub-elem. Ø [μm]	70	70
Sub-elem. Nr.	31	31
Heat treatment	200 °C, 24 h 380 °C, 50 h 570 °C, 112 h 660 °C, 100 h	380 °C, 48 h 580 °C, 48 h 700 °C, 92 h

Table 3.3: Characteristics of six-cluster wires analyzed.

3.1.1.1 SEM investigation

All wires were investigated by SEM-EDX and prepared by using both method A (samples T4, T7 and T8) and method B (sample T3) described in the dedicated paragraph of Chapter 2). We performed EDX line scans over several wire sub-elements along the radial direction, from the sub-element periphery to the Cu-Sn core. The arrows in Figure3.5 and Figure 3.6 show typical EDX line scan positions for T3/T4 and T7/T8, respectively. We choose the thickest area per selected sub-element to measure T3 and T4, whereas the T7 and T8 EDX line scans were carried out and averaged over three clusters per selected sub-element. In particular, we tried to select those that were least deformed and closest in size. For all SEM measurements, we used a working distance of 10 mm, an electron beam energy of 15 keV, an aperture (placed before the microscope objective lens) of 30 μ, and a beam spot size (width of the electron beam that comes from the filament) of approx. 4 nm. The EDX spectra were collected with a dwell time (inspection time spent by the beam on a certain point of the sample) of 5 s per point of the selected analysis line. A step width of 200-300 nm was chosen (distance between two analysis points), depending on the sample and the thickness of its Nb_3Sn region. We made a statistical analysis comparing first the Sn concentration gradients of T3 and T4, respectively three-cluster and standard wire coming from the same heat treatment, and then those of T7 and T8, wires with the same six-cluster layout and coming from different heat treatments. For data analysis we used EDAX-TEAM software .

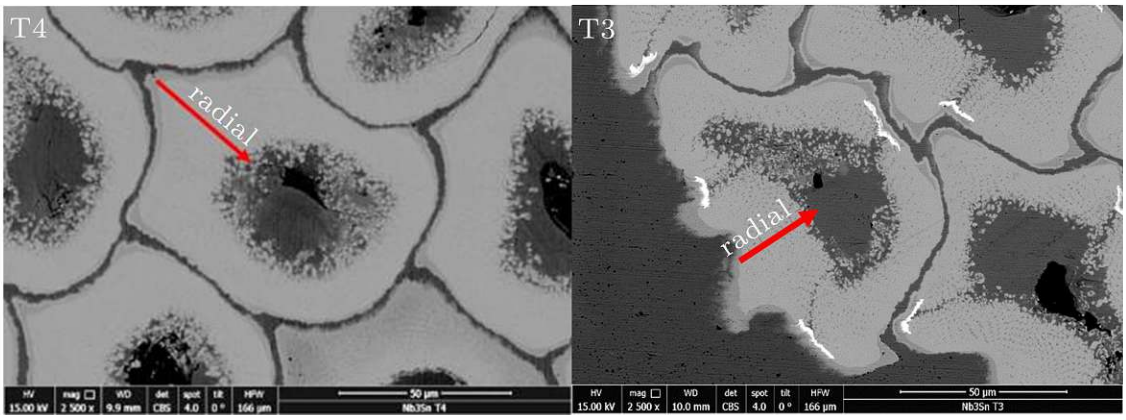

Figure 3.5: Example of a typical EDX line scan (red arrow) from the Nb barrier to the Cu-Sn core for (a) the standard wire T4 and (b) the three-cluster wire T3. This image was taken with the BSE detector.

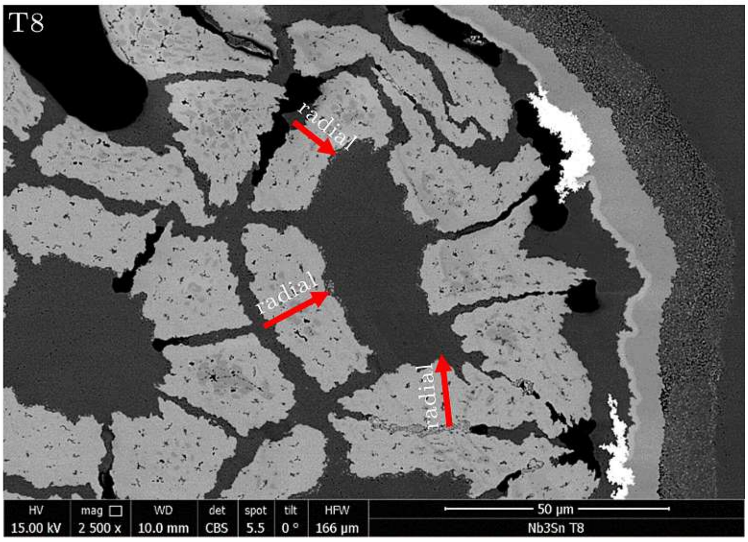

Figure 3.6: Example of typical EDX line scans (red arrows) from the sub-element periphery to the Cu-Sn core for both wires with a six-cluster layout (T7 and T8). This image was taken with the BSE detector.

3.1.1.2 TEM investigation

We made a TEM-EDX analysis for the three-cluster sample T3 and standard sample T4, and we compared these two wire types in terms of Sn concentration gradient across the Nb_3Sn grains. For this purpose, a lamella sample of both wires (about 100 nm thick) was prepared by Focused Ion Beam (FIB) and analyzed in scanning mode of the TEM with a spatial resolution 10 nm. As shown in Figure 3.7, TEM-EDX line scan measurements were carried out over several Nb_3Sn grains from one grain boundary to the opposite one. For such measurements, we selected approximately round-shaped grains since grain morphology is closely connected to Sn content. Specifically, equiaxed grains are related to higher Sn contents [120], [121], [122]. It must be said, however, that according to previous studies by Lee and Larbalestier [123], and Uglietti et al. [124], the totality of grains in high non-Cu J_c Internal Sn wires is equiaxed. For all STEM-EDX measurements, an operating beam energy of 200 keV was used and the EDX spectra were collected with a dwell time of 5 s per analyzed point along the measurement line from one grain boundary to the opposite one. Moreover, we choose very thin lamella regions, approximately 50 nm thick, to avoid overlapping of grains and therefore a distorted analysis. Also for the TEM characterization, we performed a statistical analysis to compare the Sn gradients of the two wires. Also in this case, we used EDAX-TEAM software for data evaluation.

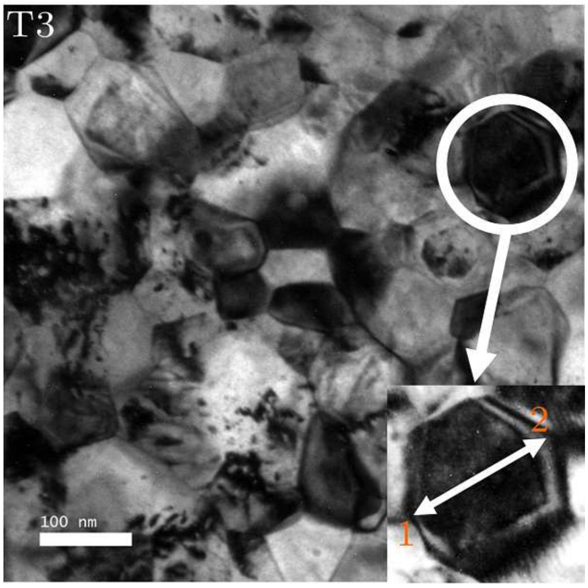

Figure 3.7: HAADF-STEM image showing different T3 Nb3Sn grains. The close-up at bottom right is showing a typical EDX line measurement, from one grain boundary (1) to the opposite one (2).

3.1.1.3 SHPM investigation

We employed SHPM at Atominstitut (TU Wien) to get an impression about the transport properties of the analyzed three-cluster and standard specimens. In particular, we aimed at evaluating the influence of the cluster and standard sub-element geometry on the local currents flowing over the cross-sections. To obtain spatially resolved maps of the remanent magnetic field, and thus extract the currents flowing through the wire cross-section, we magnetized our 0.8 mm thick samples by applying and removing a field of 2 T. The current densities profile of the samples was evaluated at 10 K and self-field. We also performed Meissner-state scans over the transversal cut of the wires above T_c of Nb (at 10 K) with an applied field of 5 mT, and the Hall probe 3 μm above the sample surface. In this way, we wanted to determine the sub-element radial-T_c distributions, from which it is possible to infer the Sn-concentration gradients to be compared with the ones obtained through SEM-EDX.

3.1.1.4 XPS investigation

XPS measurements on T3 and T4 samples and related data analysis were conducted at AIC (TU Wien). We aimed at understanding which wire had a higher Sn content to eventually have a further confirmation of the SEM-EDX results. For survey and detail spectra, pass energies (PE) of 100 eV and 30 eV, and energy resolutions of 1 eV and 100 meV were used, respectively. The PE is the energy of the photoelectrons entering the spectrometer and it sets a constant energy resolution for the whole spectrum. Higher PE means higher flux of photoelectrons and better signal to noise ratio, but the resolution is worsened. On the other hand, spectra recorded with low PEs have a better resolution, but a worse signal to noise ratio. For our XPS measurements the following settings were used: excitation energy of 1486.6 eV, beam energy and spot size of 70 W onto 500 μm, mean angle of 51° to sample surface normal, and a pressure of 6×10^{-9} mbar. Data analysis was performed using CASA XPS software, employing Shirley/Tougaard backgrounds [125],[126] and Scofield sensitivity factors [127].

3.1.2 Results and discussion

3.1.2.1 SEM-EDX: Sn content gradient evaluation

For both T3 and T4 wires, we obtained a Sn concentration gradient slightly ascending towards the core at the limit of the measurement accuracy (See Fig. 3.8). This slightly ascending trend is consistent with the fact that the Nb_3Sn phase is formed through the diffusion of Sn from the core region. In particular, the Sn gradient slope is more pronounced in the case of the T4, suggesting a more homogeneous Sn distribution over the T3 cross-section. The T3 Sn gradient is (0.015 ± 0.004) at%/μm^2 and thus reduced by a factor of 1.6 with respect to the T4 one which is (0.025 ± 0.004) at%/μm^2.

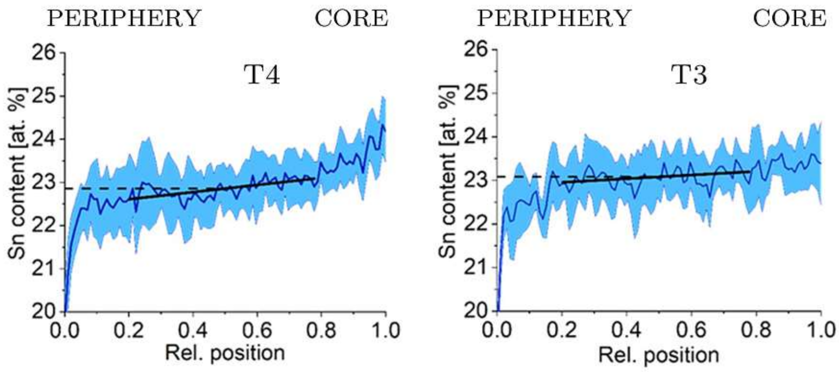

Gradient: (0.025 ± 0.004) at. %/µm

a

Gradient: (0.015 ± 0.004) at. %/µm

b

Figure 3.8: Sn content gradient along the radial direction, from the Nb barrier to the Sn-Cu core, for both the standard wire T4 (a) and the cluster wire T3 (b). The coloured background stems from the single measure-ments performed over several sub-elements. The dashed lines repre-sent the average Sn content [at%] value taken at 0.5.

Besides the Sn content variation being smaller for T3, also the average value of the absolute Sn content (taken at 0.5) is higher for the cluster wire than for the standard one within the experimental margin of error. The absolute value is also very important for the optimization of the superconducting properties, not just the gradient [18], [128]: a perfectly homogeneous wire with 18 at% Sn would be useless. It must be said that EDX itself is not the most reliable technique due to its huge relative error of up to 10%. To confirm these results, it would be hence useful to do a countercheck using other techniques, e.g. Auger spectroscopy (AES) due to its spatial resolution up to approx 10 nm (the A15 region of this study samples is between 20 μm and 30 μm, depending on the wire type and sub-element shape). However, based on the obtained results, the cluster sub-elements seem to have a great potential in terms of producing wires with higher homogeneity, so contributing to a better superconducting performance.

What if the starting sub-element layout had more Nb-free routes than just three? The results achieved for the T3 suggested to us that a higher number of clusters, and therefore of free routes for the initial Sn to diffuse, could further help Sn to homogeneously distribute from the core to the peripheral barrier. For understanding this better, we analyzed the six-cluster layouts of T7 and T8 as we did for T3 and T4. In this case, we are not only dealing with two six-cluster wires, but we also have to consider the different heat treatments they come from and understand the influence of temperature onto the homogeniety of the wire. As displayed in Fig. 3.9, both slopes of the Sn gradient are slightly descendent at the limit of the measurement accuracy, and the T7 one is more pronounced. The Sn distribution is thus more homogeneous over the T8 cross-section. The descending slopes of the Sn gradient also suggest that having more Nb-free pathways might actually ”speed up” Sn diffusion by allowing the peripheral part of the sub-element to have a Sn content very close to or even slightly higher than the core region. And speaking of that, the T8 data shaping a hinted “U” trend seem to confirm that these six free diffusion routes help Sn to better flow towards the subelement periphery and equitably distribute between core and periphery. The Sn content in these two sub-element regions appears, in fact, very similar. Moreover, considering the smaller Sn gradient for the T8, it can be inferred that its heat treatment (380 °C - 48 h, 580 °C - 48 h, 700 °C - 92 h) is more effective in leading to higher homogeneity.To further support this statement, the kinetics of Nb_3Sn growth at the different heat treatment stages should be singularly investigated. M. V. Krylova et al. found such Nb-free Cu channels to be accelerating the formation of the superconducting phase by intensifying the diffusion of Sn [129]. Nevertheless, the precise role of these resistive separators in producing a balance between the Sn concentration near the core and that near the periphery has yet to be studied and understood in more detail.

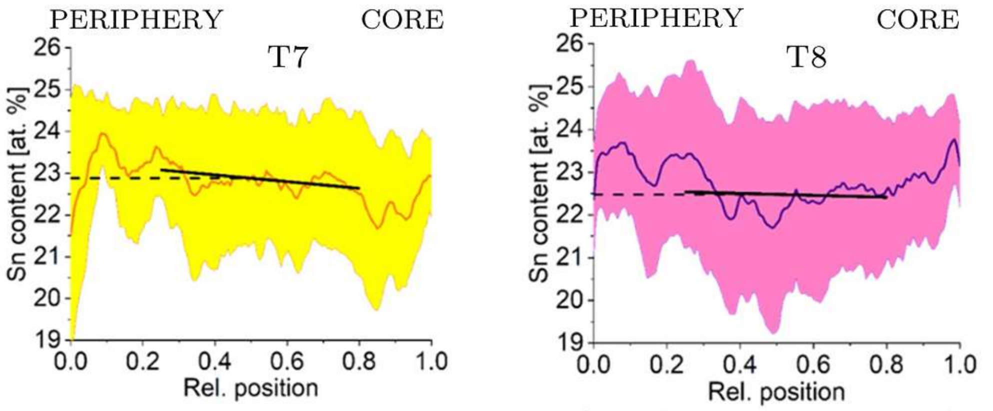

Gradient: (-0.040 ± 0.006) at. %/µm Gradient: (-0.010 ± 0.001) at. %/µm

a b

Figure 3.9: Sn concentration gradients along the radial direction of T7 (a) and T8 (b). The background, yellow and pink for T7 and T8 respectively, stems from the single measurements performed over several clusters. The dashed lines represent the average Sn content [at%] value taken at 0.5.

It should be noted that the noise in both T7 and T8 data trends is due to the presence of Cu inclusions in the Nb_3Sn volume. These graphs are suggesting that the Cu content of the Nb_3Sn region is higher for T7 and T8 than T3 and T4. This might be due to the different barrier configuration and the heat treatment steps at 380 °C and 400 °C steps. According to previous works of other research groups, the approximately 200 °C step is inconsequential, whereas the 380 °C or 400 °C step is expected to result in a less Sn-rich core (inward Cu diffusion) and convert η phase (Cu_6Sn_5) to ϵ phase (Cu_3Sn) before it melts [130], [131], [132]. The interfilamentary Cu (separating the sub-elements) is therefore more depleted, i.e. sucked to the Sn-rich core, for distributed barrier (T3/T4) than for common barrier (T7/T8) wires, and for 400 °C compared to 380 °C, based on the study by S C. Hopkins et al [132]. This could result in more interfilamentary voids for T3 and T4, and more Cu for T7 and T8.

Even though T8 has a smaller Sn gradient, the average Sn content taken at 0.5 is slightly higher for T7 at the limit of the measurement accuracy and the Sn content value near the core is very similar in both samples. It is thus still not clear which heat treatment would be more efficient in producing cluster wires with optimized superconducting properties. Previous studies on other six-cluster layouts suggested a less homogeneous Sn distribution than found here for T7 and T8 [116]. The behaviour clearly depends sensitively on sub-element design, deformed geometry and heat treatment conditions, and further study is needed to confirm the best approach for achieving a higher superconducting performance.

3.1.2.2 TEM-EDX: Sn content gradient evaluation

As the previous SEM-EDX analysis suggested a higher homogeneity over the cross-section of the three-cluster sample, we aimed at further confirming this through a TEM investigation. Figure3.10 shows that the T3 and T4 Sn gradients over the Nb_3Sn grains are very small within the experimental margin of error. A TEM lamella was cut from the central part of the A15 region for both T3 and T4 to make the data as comparable as possible. The Sn gradient slope of these wires is slightly descending at the limit of measurement accuracy and it is more pronounced for T4, as found through SEM investigation of the wire cross-section. And similarly to as observed for the SEM analysis, the value of Sn taken at 0.5 is slightly higher for the three-cluster sample. Thus, this preliminary TEM investigation seems to confirm that the three-cluster layout has an interesting potential for obtaining more homogeneous wires overall. However, it should be noted that especially the noise for T4 is quite high. This could be due to the fact that we selected a limited number of grains, i.e., those with a shape as round as possible (as described in a previous section). Also, this noise could be reduced by investigating more TEM lamellae per sample, as this would allow for higher statistics. We are planning further investigations, which is why we have referred to the current TEM analysis as "preliminary".

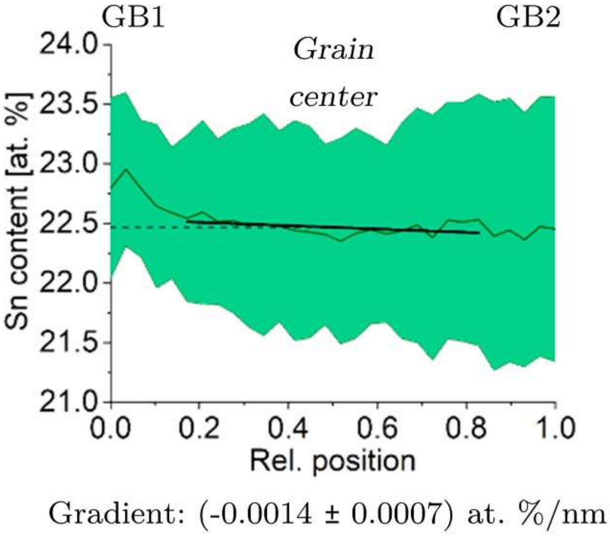

Figure 3.10: Sn gradient for a T3 TEM-lamella sample. The coloured background stems from the single measurements performed over several grains, from one grain boundary (GB1) to opposite one (GB2). The dashed line represents the average Sn content [at%] value taken at 0.5.

As aforementioned, EDX-Sn value is not really reliable and further confirmatory analysis should be performed. Auger spectroscopy (AES) would be a good contrast method to use, as demonstrated by previous analyses of other groups, who evaluated composition gradients through Nb_3Sn grains by means of this technique [133], [134], [18].

3.1.2.3 SHPM: preliminary J_c evaluation

The three-cluster and standard wires, T3 and T4 respectively, were fully magnetized and scanned in self-field. The remanent field scan of sample T3 is reported in Figure 3.13 as an example.

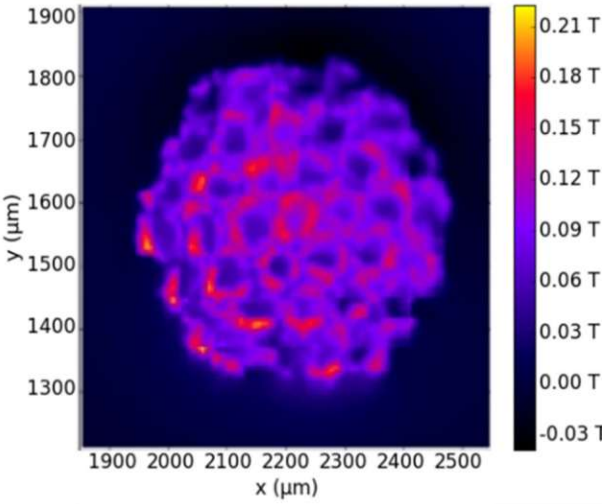

Figure 3.11: Scan of the remanent-state of sample T3 after applying and then removing 2 T (sample fully magnetized).
Credits: M. Ortino, Atominstitut (TU Wien)

Two single lines were always extracted from these area-scans, typically in the centre, as fixed y and x directions. In Figure 3.12 only the central y-line scans are shown, as the x-line scans led to analogous results. The peaks of the graphs in Figure 3.12 correspond to the individual contribution of the sub-elements and a tendency of such peaks to sum up towards the central peak can be noticed. This is suggesting a coupling of the sub-elements inside the wire, so that the supercurrents can flow between them. For both the standard and the three-cluster layouts, the inter sub-element coupling can clearly be observed: the highest signal is in the middle. This outcome means that part of the current is flowing over the entire sample cross-section contributing to a bigger signal at the centre. We can explain this if we look at the Cu resistive separators, which appear too thin for an efficient separation of the sub-elements, also resulting in a weak partition of the clusters. And this is also explaining the total screening seen in the Meissner-state scans of both samples, which is highly related to the wire architectures. Therefore, we could not evaluate Sn gradients at different temperatures for comparison with SEM-EDX data. In both T3 and T4, we observed a screening effect as depicted in Figure 3.13 (it's not possible to distinguish the single sub-elements).

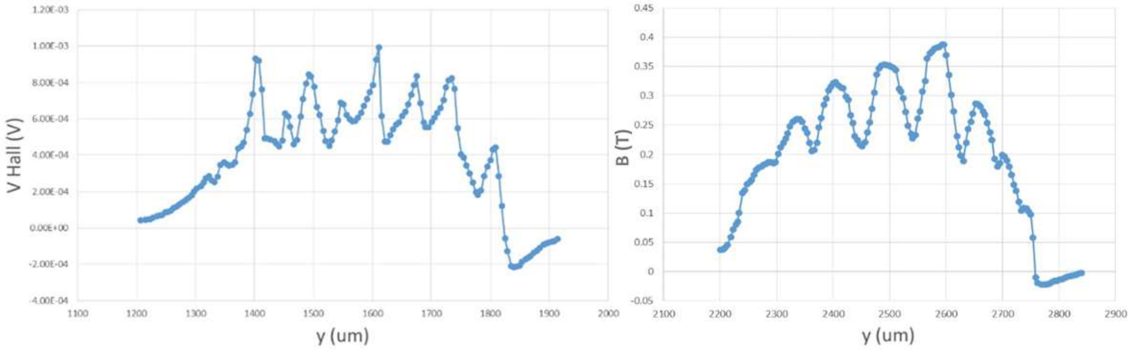

a b

Figure 3.12: Central y- line scans of the remnant-state of the sample T3 (a) and T4 (b). The voltage on the Hall-probe is shown in (a) and in (b) it is converted to field values after calibration.
Credits: M. Ortino, Atominstitut (TU Wien)

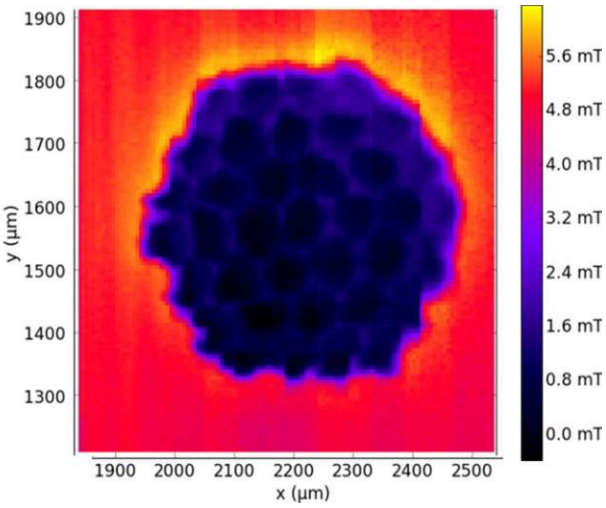

Figure 3.13: SHPM Meissner-state scan at 10 K and 5 mT of the T3 sample.
Credits: M. Ortino, Atominstitut (TU Wien)

We tried to overcome this "screening effect" problem by etching away Cu, then the outer Cu crown, and resistive separators. Figure 3.14a shows the Cu etching system used. We immersed the sample in a solution of distilled water and HNOtextsubscript3 (1:1). A magnet was placed inside the container with the solution to keep it well mixed through its movement. Figure 3.14b (left) shows the cross-section of sample T4 post Cu-etching, once polished to a thickness of 1 mm. Since the thickness of the sample is very important for performing accurate SHPM measurements, we continued to polish the sample surface to a thickness of about 200 μm (figure:etchingb - right). As we went down in thickness the Cu came out again in the core of the sub-elements and only in small portions of the region of interest, the one between the sub-elements (red circles). This allowed us to proceed with the new SHMP measurements, which did not bring clear improvements. Since the sub-elements are highly deformed (and thus lead to their coupling), further work on the manufacturing process and heat treatment would be useful.

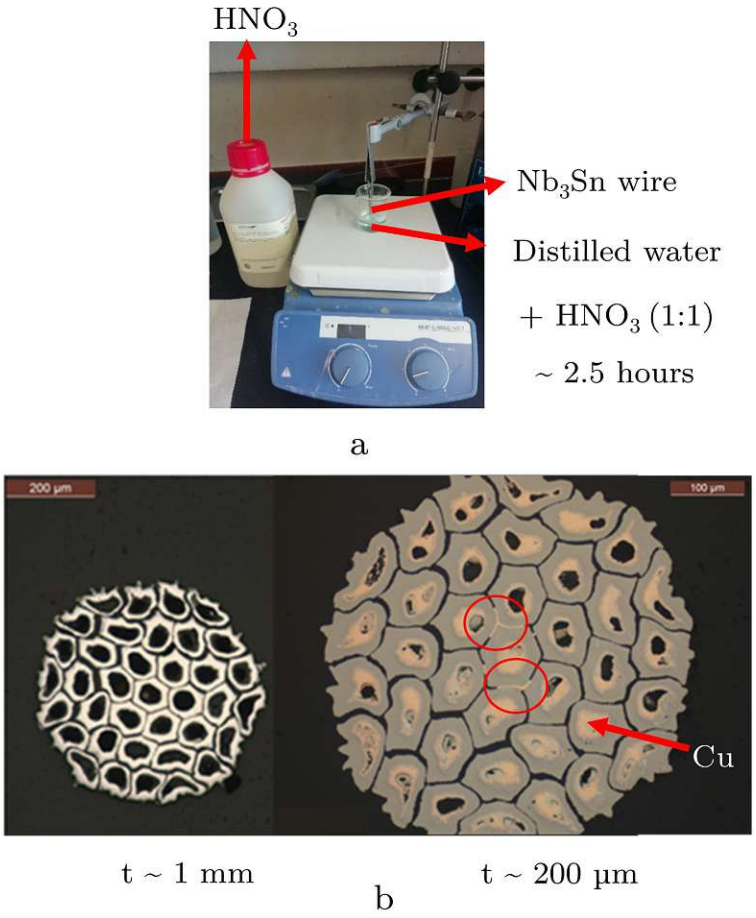

Figure 3.14: (a) Cu etching system; (b) light microscope images showing the cross section of the T4 after Cu-etching, polished to 1 mm thickness (left) and 200 mum (right). The red circles point out the Cu coming out in small portions of the region of interest (between the sub-elements).

By inverting the remanent field profile (seen in the example of Figure 3.11), it is possible to evaluate how each sub-element with its geometry contributes to the local currents flowing over the cross-section. The current densities profile of sample T3, evaluated at 10

K and self-field, is presented in Figure 3.15 as an example since we obtained very similar results for the sample T4. The maximum values achieved for both T3 and T4 are in line with the commercial RRP wires (HL-LHC target) at the same conditions (about 4.8×10^4 A/mm2). As previously mentioned, the strongly deformed sub-element shapes, also contributing to the very thin thickness of the resistive separators, and the irregularities of the barriers (Nb and Ta for T3, and Nb for T4), let us think that there is still room for improvements. Thus, the J_c values can be raised by acting on the manufacturing process and heat treatment parameters.

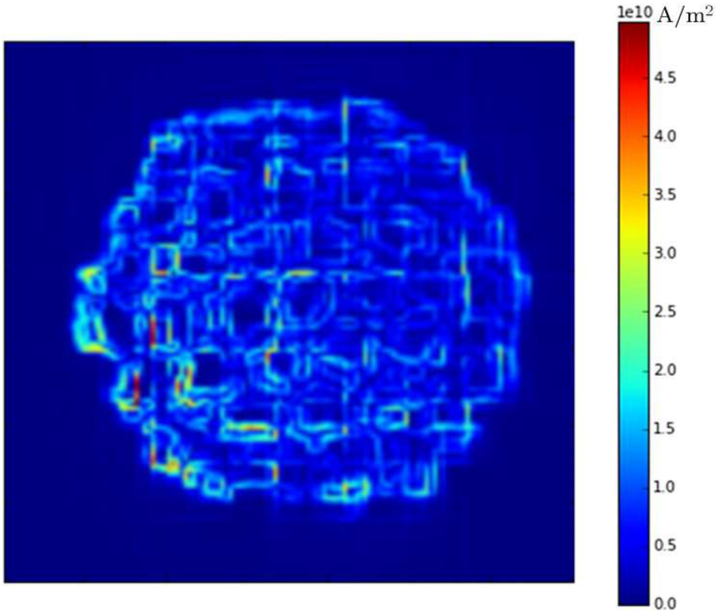

Figure 3.15: T3 current densities profile at 10 K and self-field.
Credits: M. Ortino, Atominstitut (TU Wien)

Based on studies by other groups, there is a substantial drop of J_c in RRP® wires with reduced D_{eff} (below 50 μm), and the reasons for it still have to be better clarified [135], [131]. This could especially affect samples T3 and T7/T8 since their cluster layouts (cluster sizes of 47 μm and 25 μm, respectively) were originally intended for D_{eff} reduction. According to Sanabria et al.,*"J_c can be raised by redesigning the intermediate heat treatment stages to minimize $Nb_{0.75}Cu_{0.25}Sn_2$ ("Nausite") formation and maximize Cu diffusion into the core"* [131]. The authors of [131] demonstrated the very positive impact of their heat treatment on J_c for samples with D_{eff} of approx. 35 μm. However, the best heat treatment steps for improving the performance of cluster specimens are yet to be thoroughly investigated and understood.
Results in the literature comparing six-cluster wires, like T7 and T8, to standard wires, like T4, found the latter to have a higher J_c [116]: the authors attributed this to compositional factors and microstresses, but it should be noted that results for different sub-element designs and heat treatments are not directly comparable. Moreover, previ-

ous research works investigating wires with the same standard structure as T4 (produced by the same manufacturer) showed J_c values in line with the HL-LHC specifications [17].

3.1.2.4 Sn content evaluation through XPS

Since AES at TU Wien is not currently available, we decided to examine the three-cluster T3 and the standard T4 with XPS, which, however, has a lower spatial resolution than AES.The original idea was to verify the absolute values of Sn content for both samples. The XPS beam diameter used as a standard at AIC is 500 μm and the A15 region per sub-element/cluster between 20 μm and 30 μm: we therefore decided to perform a comparative relative analysis of T3 and T4 only to further confirm a higher overall Sn content for the former. All samples had Sn oxides on the surface. Ar-ion sputtering was hence used to remove oxides for assessing Nb and Sn signals. After 45 s of sputtering most oxides were removed. Fig. 3.16 shows low pass energy (PE=30) Sn 3d and Nb 3d detail spectra of T3 and T4 after sputtering times of 45 s, 300 s and 900 s.

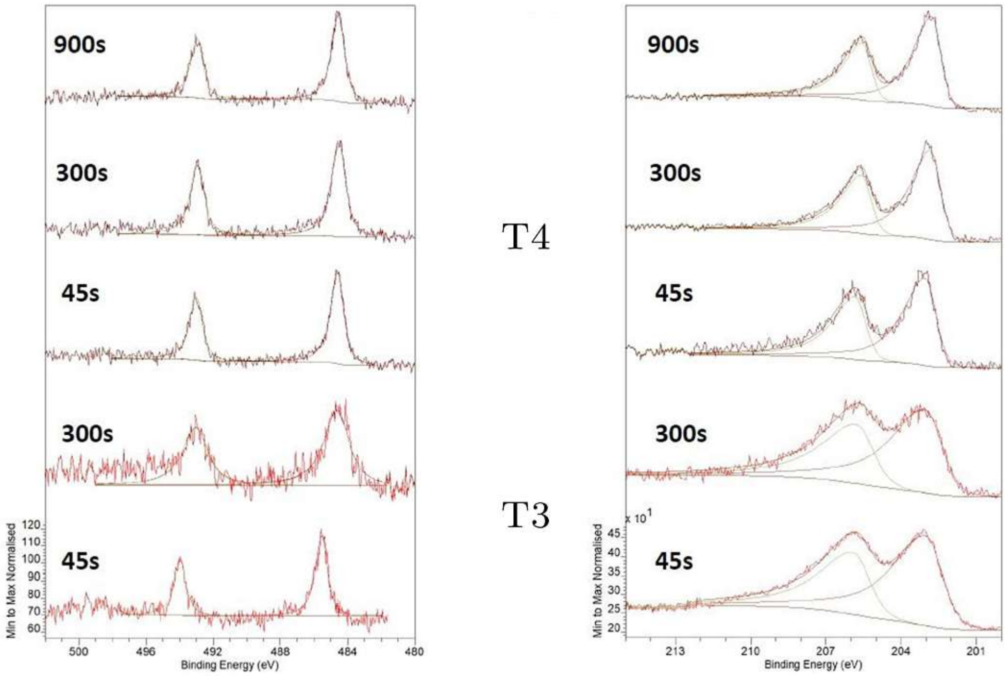

a b

Figure 3.16: XPS Sn 3d (a) and Nb 3d (b) detail spectra of T3 (bottom) and T4 (top). PE: 30 eV, Step 0.05 eV, Dwell 0.1 s. *Credits: M. Sauer and A. Foelske, AIC (TU Wien).*

A Sn content and Sn/Nb ratio analysis was carried out by comparing the signal intensity of high pass energy spectra (PE = 100eV) in Fig. 3.17, considering that high pass energies allow for higher signal to noise ratios (see previous paragraph generally describing the XPS investigation).

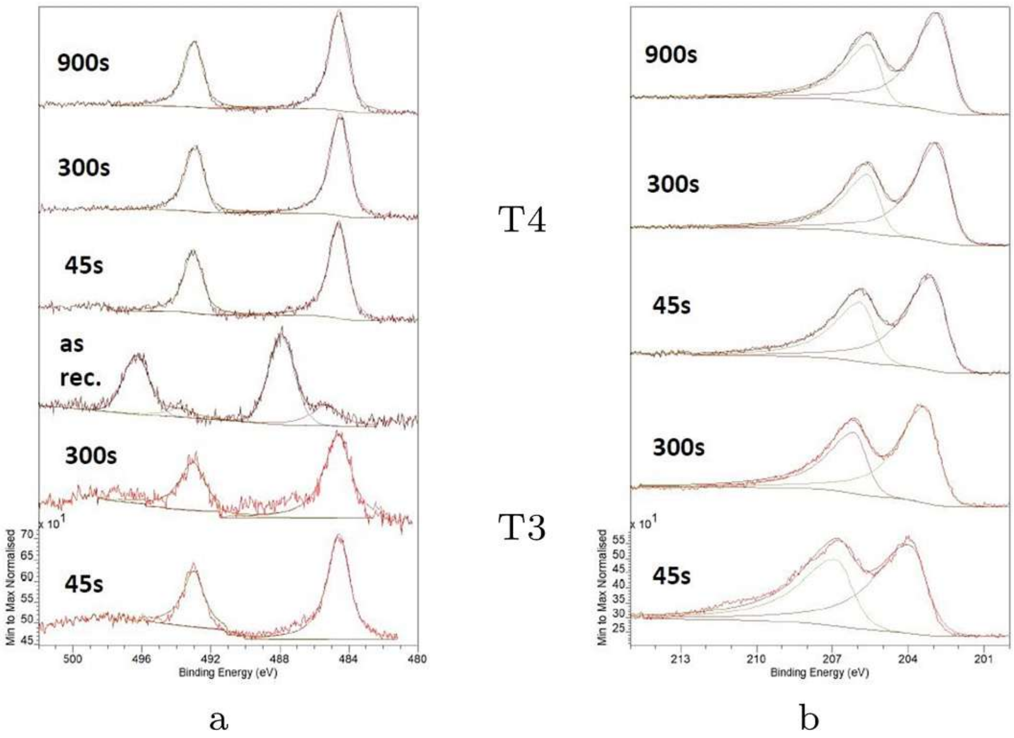

Figure 3.17: XPS Sn 3d (a) and Nb 3d (b) detail spectra of T3 (bottom) and T4 (top). PE:100 eV, Step 0.05 eV, Dwell 0.1 s,
Credits: M. Sauer and A. Foelske, AIC (TU Wien).

After a sputtering time of 45 s, Sn/Nb ratios of approx. 0.30 and 0.28 were found for T3 and T4, respectively. The found T3 Sn content is 23.2 at% versus a T4 Sn content of about 22.2-23.2 at%. As mentioned, we didn't focus on these absolute values since XPS measurement accuracy is comparable to EDX one. Despite that, this analysis is suggesting that the T3 has a higher overall Sn content than the T4, so confirming the SEM-EDX results. In contrast, after 300 s of ion sputtering a Sn content of about 18.7 at% was achieved for the T4, higher than the T3 one (16.5 at%) seems to be higher for the T4. However, the obtained Sn/Nb ratios for T3 and T4 after 300 s of sputtering are respectively about 0.20 and 0.23 and therefore not attributable to Nb_3Sn. Ar-ion sputtering thus changes the Sn/Nb ratio according to the process time and probably by preferential sputtering of Sn.

3.2 APC–Nb_3Sn wires

We received five powder in tube (PIT) Nb_3Sn wire samples with artificial pinning centers (APC), manufactured by Hyper Tech Inc. (Ohio, US) and Fermilab (Batavia, US) [136],[22],[137],[138], [67]. Previously, a magnetic and superconducting characterization was performed at TU Wien-Atominstitut and Hyper Tech Inc. At TU Wien - USTEM we took care of the sample microstructural characterization to understand how the latter is correlated to the different heat treatments performed.

3.2.1 Purpose of microstructural characterization

Through this study, we wanted to explore the physics behind the high-performance of internally-oxidized APC samples by observing eventual microstructural changes due to the presence of different dopants (Zr and Hf) and heat treatment differences in terms of temperature and time. In the previous analaysis regarding internal tin Nb_3Sn wires, we showed that the starting sub-element layout (pre heat treatment) has Nb filaments uniformly distibuted trough the Cu matrix. In the case of internally-oxidized APC samples, the filaments consist of a Cu-clad Nb-Ta-Zr or Nb-Ta-Hf tube filled with a mixture of Sn, Cu, and oxide powders.*"Numerous filaments are stacked together with Cu rods in a Cu can and co-drawn to form a composite strand. Numerous filaments are stacked together with Cu rods in a Cu can and co-drawn to form a composite strand"* [138]. The strand is heat treated in such a way that first O and then Sn diffuse into the Nb alloy to form Nb_3Sn. ZrO_2 or HfO_2nanoprecipitates (with Cu-clad Nb-Ta-Zr or Cu-clad Nb-Ta-Hf, respectively) occur during diffusion due to insolubility of O in Nb_3Sn [22],[69],[138]. Such precipitates are the "main ingradient" of this wire type since they should be able to inhibit grain growth and working as point-type flux pins, so contributing to their high performing J_c [136], [70], [139], [140].
STEM-HAADF and SEM-TKD analyses were carried out on the samples listed in Table 3.4 to evaluate respectively size and density of ZrO_2/HfO_2 nanoprecipitates, and the Nb_3Sn grain size.
Our main objective was to study the correlations between PP size-density and heat treatment, and Nb_3Sn grain size and heat treatment. We also sought to understand which typology of nanoprecipitate (ZrO_2 or HfO_2) led to better results.

Wire	T3935-675×380	T3914-685×228	T3912-700×71	T3914-675×317	T3914-700×120
Designation	S1	S2	S3	S4	S5
Wire Ø [mm]	0.84	0.7	0.7	0.84	0.7
Dopant	Ta, Zr	Ta, Hf	Ta, Zr	Ta, Hf	Ta,Hf
Nanoprecipitate	ZrO_2	HfO_2	ZrO_2	HfO_2	HfO_2
Heat treatment	675 °C, 380 h	685 °C, 228 h	700 °C, 71 h	675 °C, 317 h	700 °C, 120 h

Table 3.4: Characteristics of the five APC-Nb_3Sn wires.

3.2.1.1 SEM investigation

We prepared FIB-lamellae from the embedded surfaces of each sample to perform TKD measurements and evaluate the grain size. To make our analyses as comparable as possible, we cut all lamellae along the radial direction (Nb_3Sn region) of a sub-element belonging to the wire central crown of sub-elements (see Figure 3.18). On these lamella-samples we also performed a STEM-HAADF investigation, which will be described in the next sub-section. For the grain size investigation, we used a TKD sample holder produced by TSL Solutions. Furthermore, we selected the following microscope settings: a working distance of almost 5 mm, a voltage of 25 kV, a SEM stage tilt angle of 60°, a sample holder pre-tilt angle of 90° (thus, a resulting sample holder tilt angle of -30°), a beam spot size of about 4 nm, an aperture of 50 μm,a binning size (which is roughly the size of the cluster of pixels combined) of 4 × 4, and a step size of 10 nm. Figure 3.19 represents a schematic of our TKD measurement system. The average thickness of the lamella was approx. 100 nm. For the data analysis, we used TSL Orientation Imaging Microscopy (OIM) Software (EDAX).
More information about TKD measurements and related data analysis can be found in [141], where a similar TKD analysis was carried out.

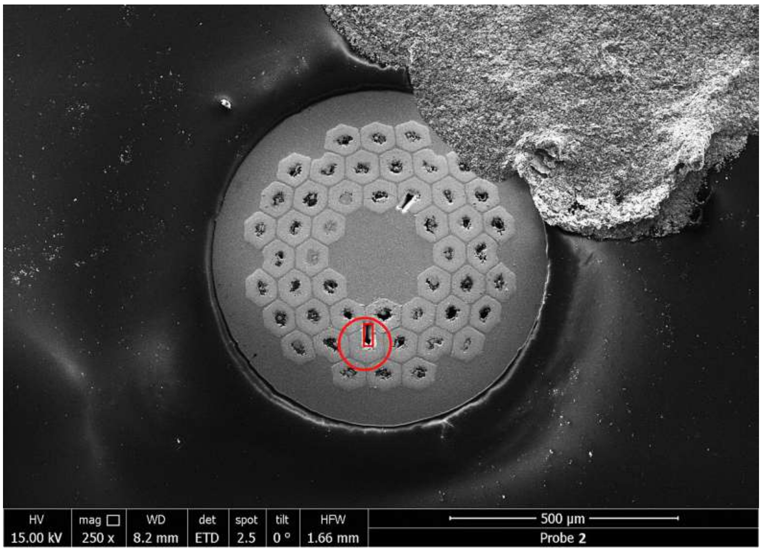

Figure 3.18: SEM overview image of an APC sample produced by the secondary electrons (SE). The red circle shows the typical position of the sub-element from which the lamella was cut (in the central sub-elements crown of the wire), and the red rectangle indicates the exact position of the lamella (along the radial direction of the Nb_3Sn region). The image was taken with the ETD as the BSE detector wasn't available at that time.

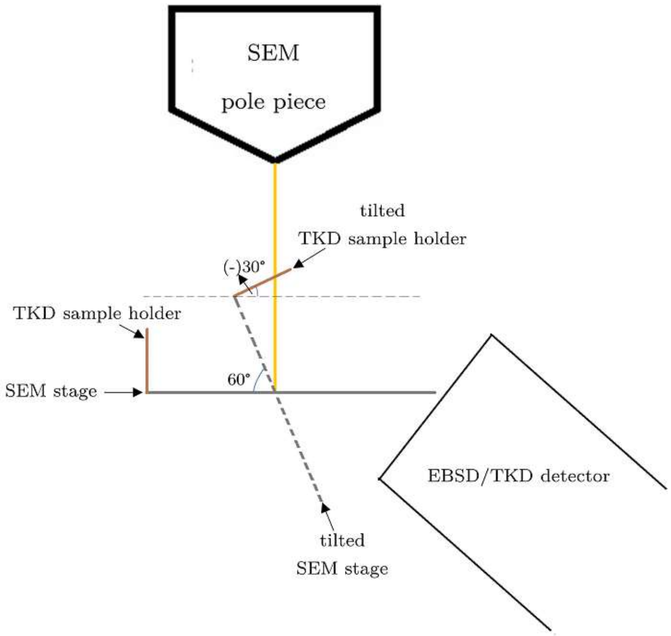

Figure 3.19: Schematic of the used TKD measurement system.

3.2.1.2 TEM investigation

All FIB-lamellae were investigated with STEM-HAADF to observe the distribution of the nanoprecipitates within the Nb_3Sn matrix and evaluate their size.In particular, we always analyzed regions located in a central zone of the lamella, thus not too close to the core of the sub-element or to its peripheral part (an example is shown in Figure 3.20). STEM-EELS helped us calculating the thicknesses of the recorded lamella regions, those with an evident distribution of the nanoparticles. By recording such images and averaging the area thickness over five points of the selected region, we were not only able to investigate the particle size, but also evaluate the particles density. Such five points were carefully selected where only a Nb_3Sn matrix was present. To measure the thickness, EELS measurements with a camera length of 100 mm were carried out. For the nanoparticles identification and image recordings, we worked in "Z contrast" using STEM-HAADF with low camera lenghts (see "STEM-HAADF" in Chapter 2). Considering that the average atomic numbers of Nb_3Sn (matrix), ZrO_2, and HfO_2 are respectively 43.25, 18.67, 29.33, different contrast images were produced. ZrO_2 nanoprecipitates appeared darker than the Nb_3Sn matrix, being clearly distinguishable (Figure 3.21a) with respect to those of HfO_2 (Figure 3.21b). The latter appeared in the matrix with much lower contrast and were therefore not easy to identify.

Data analysis was performed with Gatan Microscopy Suite 3 (GMS3) Software. To estimate the size of the precipitates, we drew lines along the diameter of the particles themselves. An example is shown in Figure 3.22. By using a proper script in GMS3 we were then able to count these nanoparticles and obtain a size distribution through a statistical analysis. Most of the precipitates could be approximated to circles, but some exceptions reported an elliptical shape. In this case the longest diameter was selected. This should be considered in the results of the statistical analysis as a contributor to measurement inaccuracy. Along with this aspect, some particles below 3 nm may not have been counted, as they were not directly visible (especially in the HfO_2 case), or some may have been found in deeper layers of the region under analysis. To reduce this risk, we analysed areas of the lamella of around 100 nm thickness and, where possible, even thinner, trying to avoid grains overlapping as much as possible (as done for TEM analysis of internal tin samples). We assessed the density of precipitates by dividing the number of these particles over the volume of the chosen region. Specifically, the density obtained is the result of a weighted average over the volumes of three regions per lamella. A very similar investigation (nanoparticle size and density) was done and described in [141].

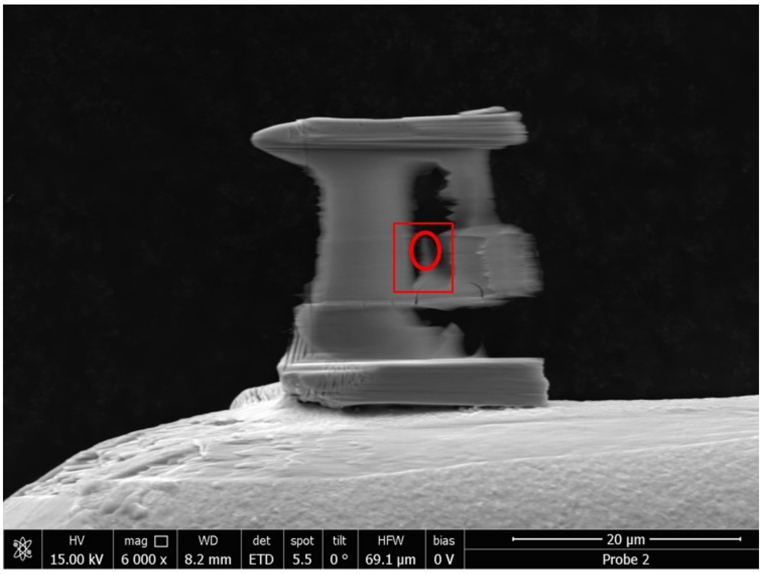

Figure 3.20: SEM overview image of an APC- Nb_3Sn lamella chosen as example for explaining the selection of the regions to analyze. The red rectangle shows the central zone ispected for selecting the analysis regions, those with a clear nanoparticle-distribution. The red circle represent the area where we could find evident nanoparticle-distributions in that specific sample. This image was taken with the ETD.

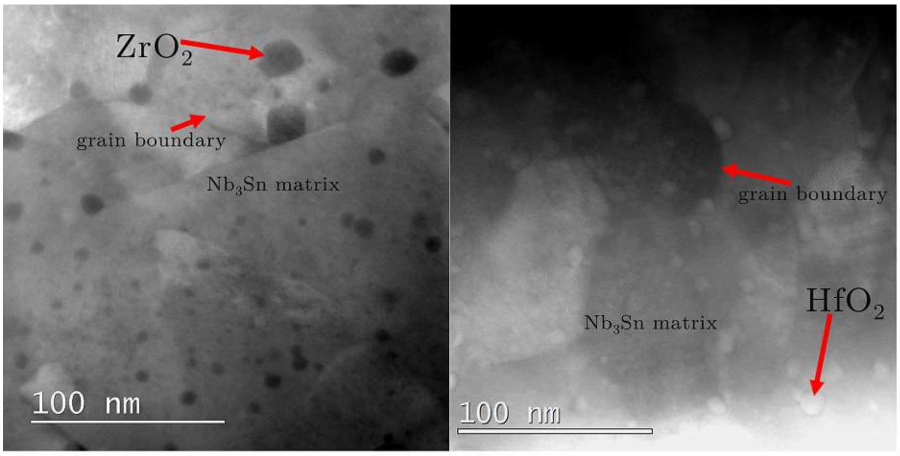

a b

Figure 3.21: Different contrast HAADF-STEM images showing (a) ZrO_2 nanoprecipitates (atomic number = 18.67) and (b) HfO_2 nanoprecipitates (atomic number = 29.33) within a Nb_3Sn matrix (atomic number = 43.25).

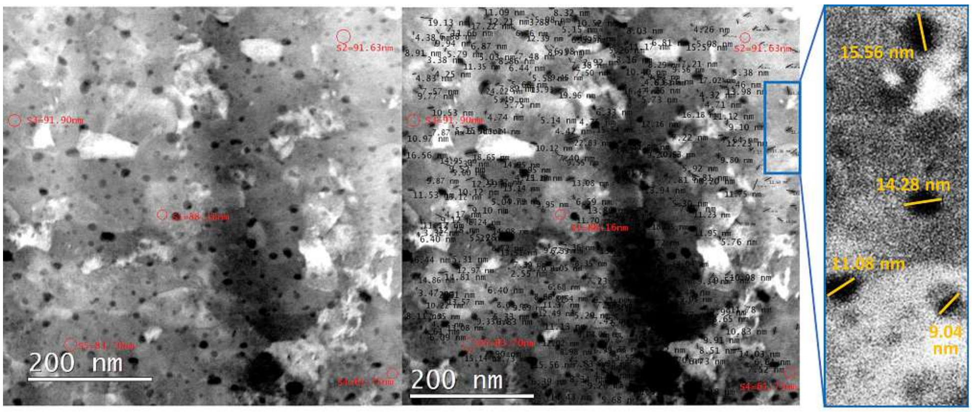

a b c

Figure 3.22: HAADF-STEM images as example of nanoparticles size and density evaluation: (a) a lamella region with evident particles distribution was chosen and its thickness was measured over five points (red circles in the image) of the Nb_3Sn matrix; (b) all particle sizes were evaluated by drawing a line along the longest diameter (if the particle was elliptical-shaped); (c) close-up of a small area to more clearly show the method used for nanoparticle size assessment.

We played with the brightness, contrast and gamma commands in GMS3 with the aim of highlighting all the nanoprecipitates present in the analyzed region and to better distinguish such particles and possible defects resulting from the FIB preparation.

As for the HfO_2 nanoprecipitates, it was more difficult to differentiate them from any defects resulting from the preparation, given the low contrast between the Nb_3Sn matrix. Figure shows a region where nanoprecipitates identification was particularly difficult due to the widespread presence of dense, very low contrast particles compared to the Nb_3Sn matrix and HfO_2 nanoprecipitates. Areas of this type were therefore not considered in the final analysis.

The presence of a dark region at the side of HfO_2 nanoparticles (width = about 1 nm), which we found to be Cu-rich, gave us a way to overcome the identification issue (see Figure 3.24).

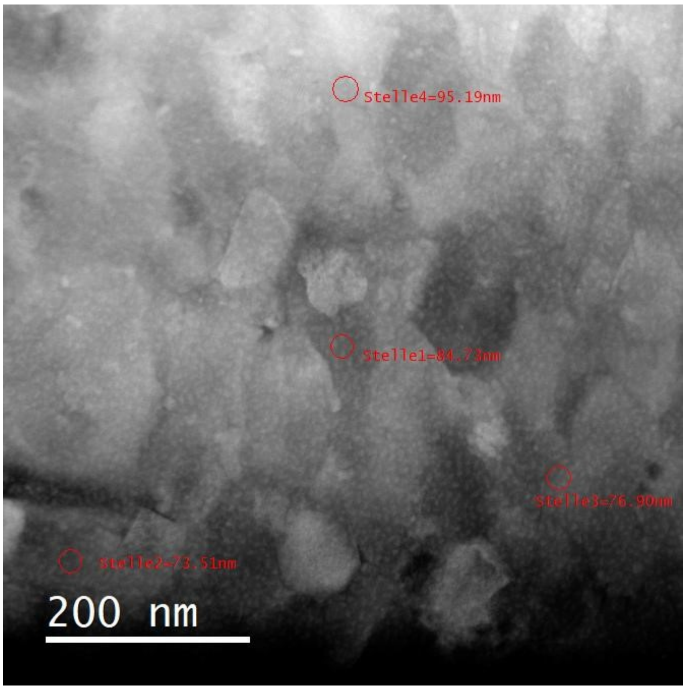

Figure 3.23: HAADF-STEM image showing a region where nanoprecipitates identification was particularly difficult due to the widespread presence of dense, very low contrast particles compared to the Nb_3Sn matrix and HfO_2 nanoprecipitates. The red text refers to the performed thickness measurements.

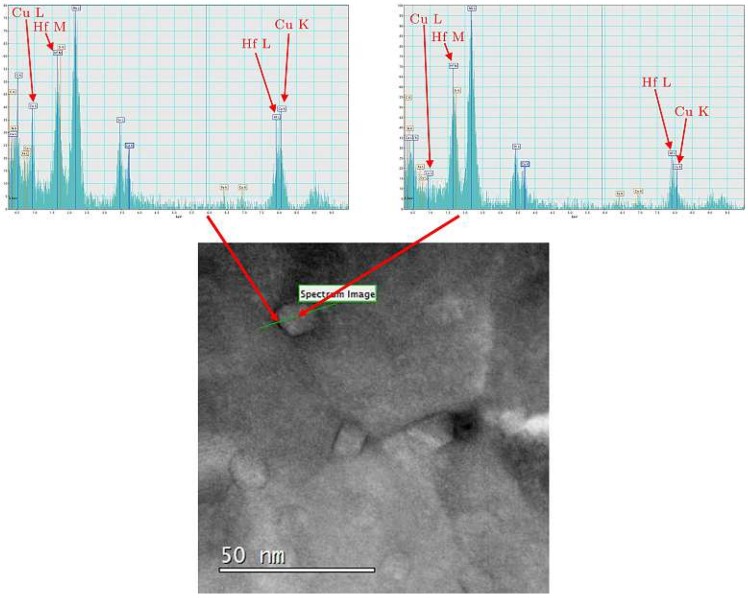

Figure 3.24: HAADF-STEM image with EDX line scan over a HfO_2 nanoprecipitate: as shown in the spectrum on the left, the dark region on the side of the particle (width: approx. 1 nm) represents a Cu-rich zone. The spectrum on the right, recorded in the middle area of the HfO_2 nanoparticle, highlights a Cu-poor zone, thus giving an idea of Cu-presence evolution.

In general, we have observed that HfO_2 tend to be present at the grain boundaries, whereas ZrO_2 does not show a preferential position. In both sample types, we did not find a homogeneous distribution of nanoprecipitates all over the lamella.

3.2.2 Results and discussion

For convenience, in the following paragraphs we will use ”PP” to refer to nanoprecipitates, which stands for ”point particles” because of the type of pinning they lead to (point-type flux pinning).

3.2.2.1 SEM-TKD: grain size evaluation

Among people working with Nb_3Sn, it is widely known that the grain size and, in particular, its refinement is key to enhancing the Jc. In simple words, the decrease in grain size results in an increase in grain boundaries and the latter represent the main flux line pinning centres in Nb_3Sn [22],[142],[143]. For TKD data analysis, grains are typically defined on “the criterion of orientation difference” [144], [145]. According to such a criterion, successive pixels whose orientation differs not more than a certain minimum value (defined by the user) are considered as part of one single grain. The definition of grain in OIM (orientation imaging microscopy) analysis therefore depend on user-specified values. Once the aforementioned minimum value is defined, the neighbours of each point in the

OIM scan are checked to see if their orientation is within the grain tolerance angle (5°) of that point. All neighbouring points with orientations falling within the tolerance angle belong to the same grain. In a OIM TKD grain size map, all grains of the same size are represented with the same colour. The maps and graphs shown in this section represent the acquired TKD grain size maps together with the statistics of grain size distribution. The observable blanks in the TKD maps are due to the existence of unallocated points: the analysis software couldn't identify such points because of a too poor quality of the diffraction pattern or due to groups of points forming too small grains (smaller than the minimum grain size specified by the user). In the graphs representing the statistics of grain size distribution, only grain sizes up to 400 nm were considered, since larger grains are not relevant for the superconducting properties [146],[60]. The graph of grain size statistics is displayed in terms of both number fraction and area fraction. The former describes the number of grains showing a certain grain size, while the latter refers to the portion of the total lamella area occupied by grains of a specific size. For these types of samples, the area fraction plot might be more informative as it gives a better idea of how different grains are distributed over the lamella itself and it's representative of the sample portion carrying current (the one characterized by smaller grains). If there are one or two large grains occupying most of the area, this is something only visible through the area fraction, whereas the number fraction would barely consider it.

Figures 3.25, 3.26, 3.27, 3.28, and 3.29 show the TKD grain size maps and statistics of grain size distribution for respectively S1, S2, S3, S4, and S5.

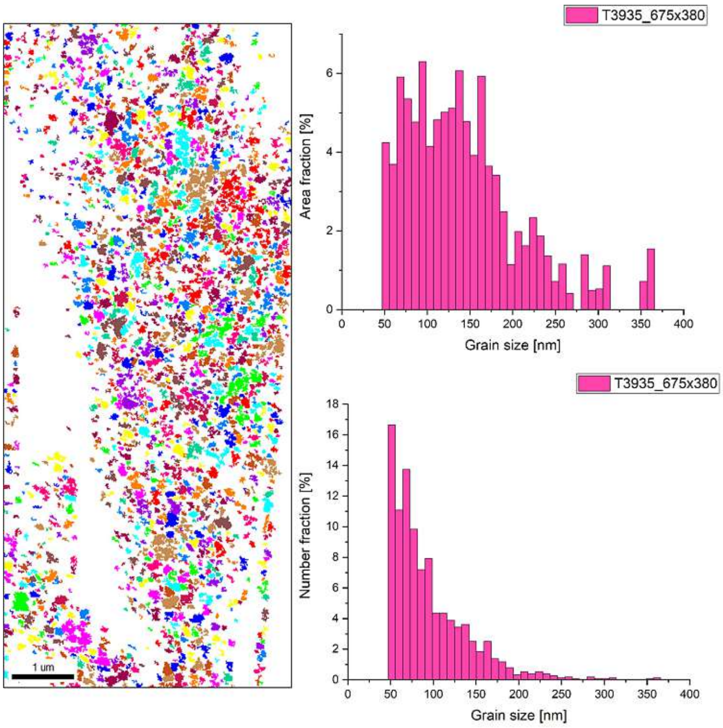

Figure 3.25: S1: TKD grain size map (left) and statistics of grain size distribution (right).

In TKD, the average grain size is typically associated to both a conventional numerical average and a value being averaged by the area of each grain. If the grain size is uniform, these two values should be close to each other. Large grains ($\geq$ 400 nm) have a significant impact on area weighted average. These grains are outliers as they do not conduct supercurrent [146],[60], so we will only consider the numerical average (NA). This value is shown for each sample in Table 3.5, along with the modal values of the grain size vs. number fraction plot.

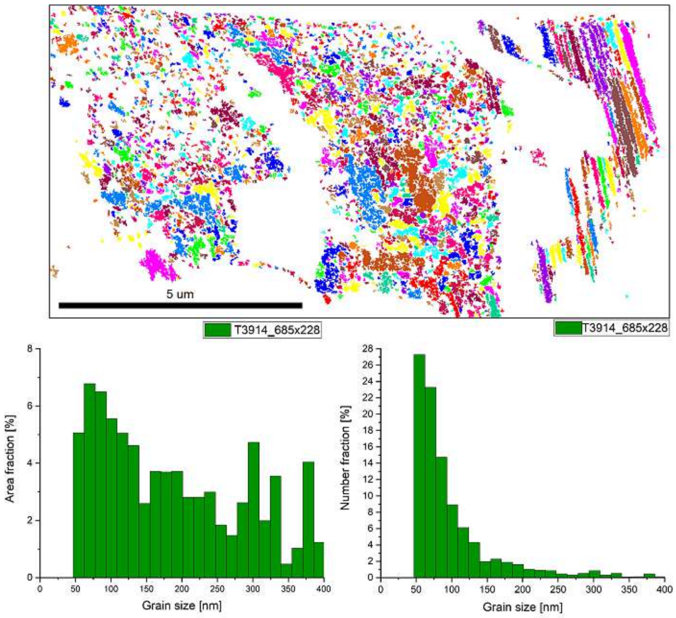

Figure 3.26: S2: TKD grain size map (top) and statistics of grain size distribution (bottom).

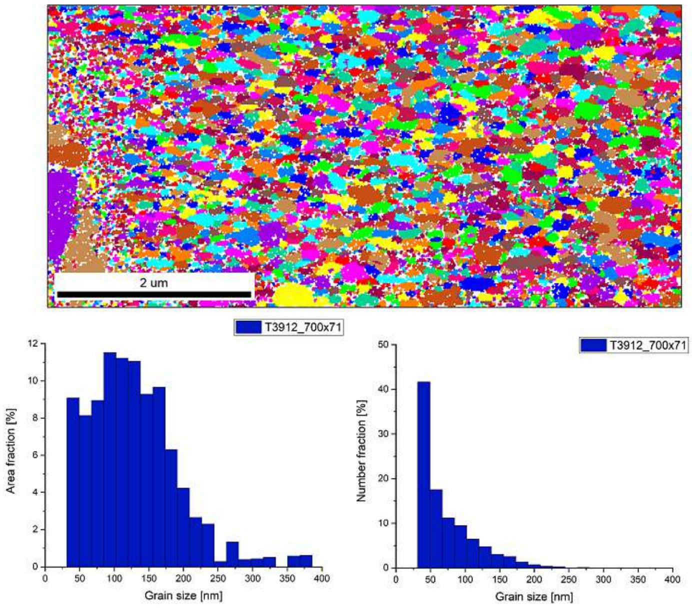

Figure 3.27: S3: TKD grain size map (top) and statistics of grain size distribution (bottom).

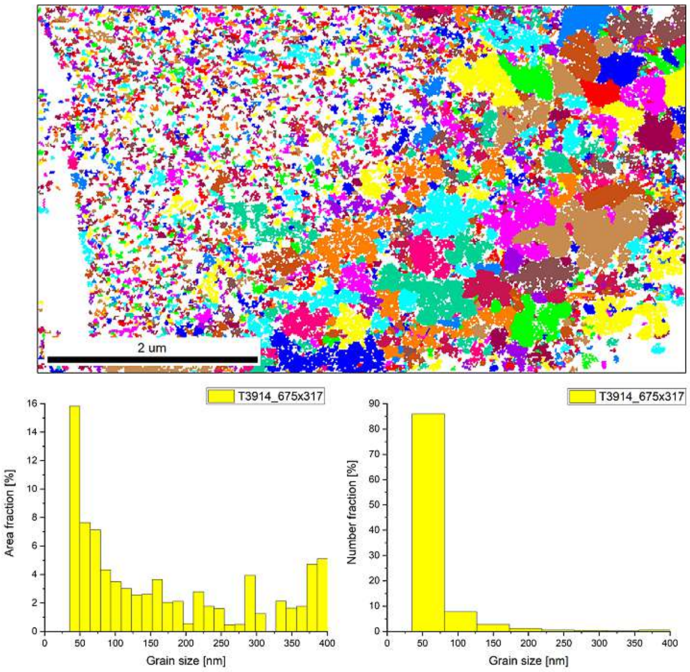

Figure 3.28: S4: TKD grain size map (top) and statistics of grain size distribution (bottom).

When performing TKD mappings, it is not possible to choose a precise location for the grain size evaluation. Based on sample preparation and lamella thickness uniformity, the TKD signal may come from different parts of the lamella as you switch from one sample to another, making the measurements not directly comparable. Along with this, sometimes the signal only comes from a small portion of the sample: in S1 the mapping concerns a portion only 4 μm wide in the central part of the lamella. The widest TKD mapping was possible in S2 (about 12 μm wide), in a region between the center of the lamella and the core area. In the other samples (S3, S4, S5) a mapping about 6 μm wide was possible.

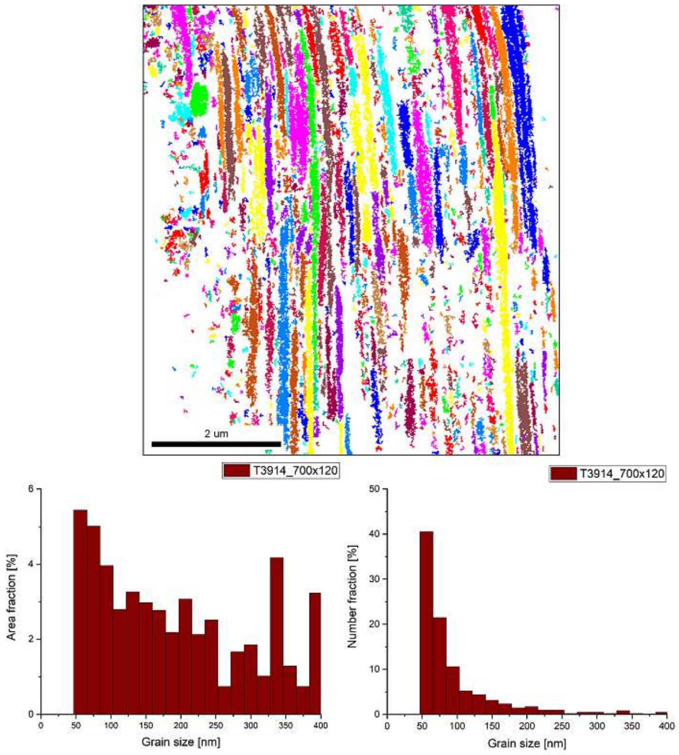

Figure 3.29: S5: TKD grain size map (top) and statistics of grain size distribution (bottom).

Wire	S1	S2	S3	S4	S5
NA [nm]	96 ± 46	102 ± 76	73 ± 44	64 ± 53	111 ± 106
Modal value [nm]	50 ± 5	55 ± 10	40 ± 10	60 ± 20	55 ± 10

Table 3.5: Grain size numerical average (NA) and modal values (grain size vs. number fraction graph) obtained for the five samples through SEM-TKD analysis.

In addition to what mentioned above, the presence of lamella areas with unallocated points makes it difficult to perform a fully reliable analysis of the grain size dependence on dopant type and heat treatment.

Grain size in the HfO_2-doped samples (S2, S4, and S5) appears to be highly non-uniform: S2 and S5 show regions with atypical elongated grains, and S4 appears to show a clear separation between area portion with small grains and portion with large grains. The latter are typically close to the core of the sub-element [147], [148]. Atypical elongated grains in S2 and S5 were also observed near the core. Unlike S2 TKD mapping, S5 one was possible in a zone with only elongated grains near the core and about 6 μm wide, as previously mentioned.

All these factors could contribute to the large measurement uncertainties that are par-

ticularly evident for S4 and S5. The fact that the lamellae were prepared by different operators most likely played a role. To make the analyses more reliable and comparable, it will be useful to prepare new lamellae as similarly as possible and to try to make them as uniformly thin as possible.
It should be considered that this analysis is part of a work which is currently in progress as new samples have recently arrived. It is thus a very preliminary analysis on grain size. The achieved results will be included in a larger study of APC wires produced by Hyper Inc. that will provide a clear understanding of the role of dopant and heat treatment temperature in grain size evolution.

3.2.2.2 STEM-EELS: PP density and size evaluation

For each of the listed samples (see first paragraph of this section), we report three analyzed areas and the related analyses (nanoparticles size and density). To evaluate the size of the nanoparticles, we considered the mean value of the lognormal distribution [149], [150] obtained from a statistical analysis by distribution fit. To obtain better lognormal distribution fits, it might be helpful to produce higher statistics by analyzing several lamellae per sample taken from different sub-elements (which is time-consuming and, therefore, only to be done if essential).

S1

Area 1 in Figure 3.30 was found to have a size of 647 nm × 647 nm. The averaged thickness of this area is 100 nm. The number of PP counted in this area is 487. From the histograms showing the PP size distribution, we observed a modal value of (4.5 ± 0.5) nm and considered (7.2 ± 1.7) nm as mean value of the PP size determined by lognormal distribution fit.

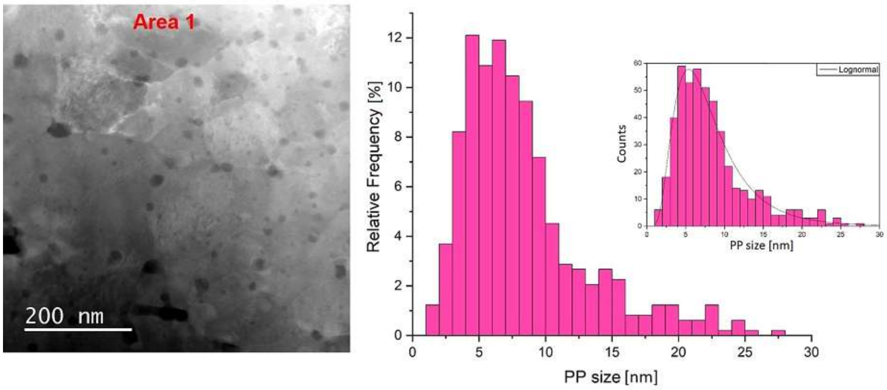

Figure 3.30: HAADF-STEM image representing the ZrO_2 PP distribution in Area 1 (left) and statistics of PP size distribution (right); the graph on top right represents the obtained lognormal distribution fit.

Area 2 in Figure 3.31 was found to have a size of 647 nm × 647 nm. The averaged thickness of this area is 94 nm. The number of PP counted in this area is 408. From the histograms showing the PP size distribution, we observed a modal value of (4.5 ± 0.5) nm and considered (5.5 ± 1.8) nm as mean value of the PP size determined by lognormal distribution fit.

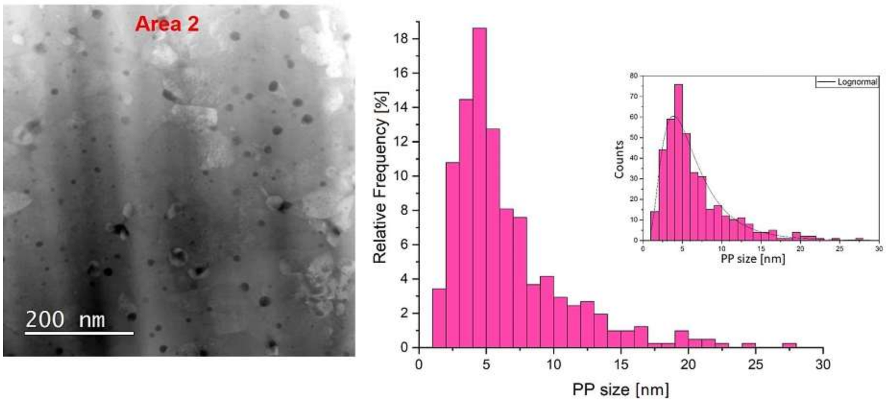

Figure 3.31: HAADF-STEM image representing the ZrO_2 PP distribution in Area 2 (left) and statistics of PP size distribution (right); the graph on top right represents the obtained lognormal distribution fit.

Area 3 in Figure 3.32 was found to have a size of 647 nm × 647 nm. The averaged thickness of this area is 95 nm. The number of PP counted in this area is 444. From the histograms showing the PP size distribution, we observed a modal value of (4.5 ± 0.5) nm and considered (6.4 ± 1.8) nm as mean value of the PP size determined by lognormal distribution fit.

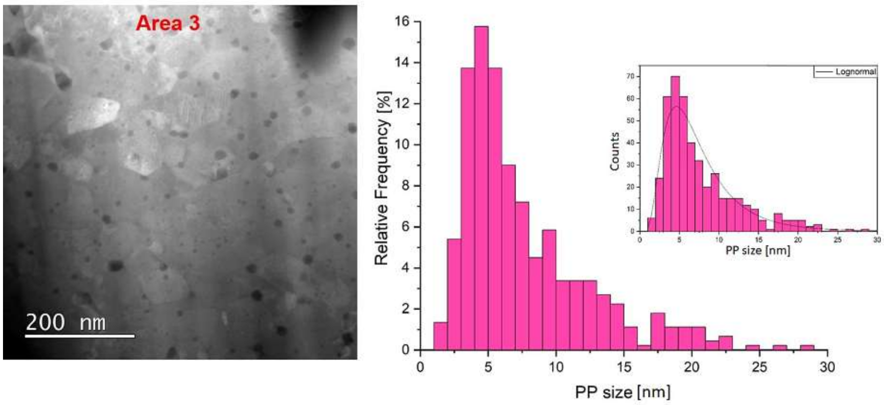

Figure 3.32: HAADF-STEM image representing the ZrO_2 PP distribution in Area 3 (left) and statistics of PP size distribution (right); the graph on top right represents the obtained lognormal distribution fit.

Considering the PP size values obtained by lognormal distribution fit for these three areas, we found (6.4 ± 1.8) nm to be the average PP size for S1, which is totally in line with the found average median value (6.1).
The average PP density for this sample is 10637 μm^{-3}.

S2

Area 1 in Figure 3.33 was found to have a size of 323 nm × 323 nm. The averaged thickness of this area is 113 nm. The number of PP counted in this area is 219. From the histograms showing the PP size distribution, we observed a modal value of (3.5 ± 0.5) nm and considered (4.7 ± 1.5) nm as mean value of the PP size determined by lognormal distribution fit.

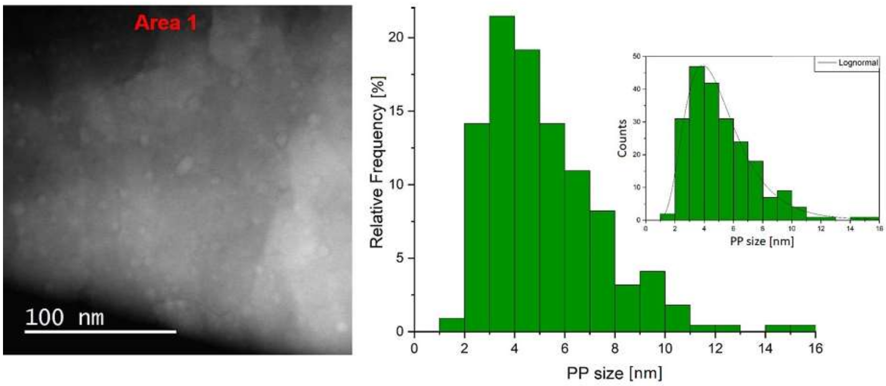

Figure 3.33: HAADF-STEM image representing the HfO_2 PP distribution in Area 1 (left) and statistics of PP size distribution (right); the graph on top right represents the obtained lognormal distribution fit.

Area 2 in Figure 3.34 was found to have a size of 323 nm × 323 nm. The averaged thickness of this area is 115 nm. The number of PP counted in this area is 336. From the histograms showing the PP size distribution, we observed a modal value of (5.5 ± 0.5) nm and considered (5.9 ± 1.5) nm as mean value of the PP size determined by lognormal distribution fit.

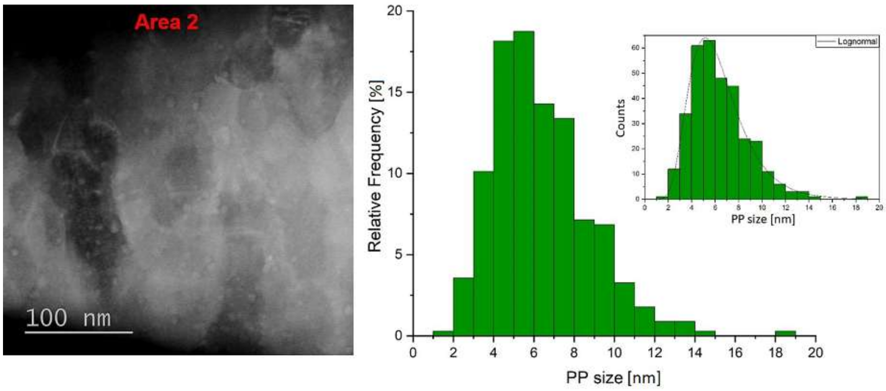

Figure 3.34: HAADF-STEM image representing the HfO_2 PP distribution in Area 2 (left) and statistics of PP size distribution (right); the graph on top rights represent the obtained lognormal distribution fit.

Area 3 in Figure 3.35 was found to have a size of 323 nm × 323 nm. The averaged thickness of this area is 117 nm. The number of PP counted in this area is 197. From the histograms showing the PP size distribution, we observed a modal value of (4.5 ±

0.5) nm and considered (6.4 ± 1.4) nm as mean value of the PP size determined by lognormal distribution fit.

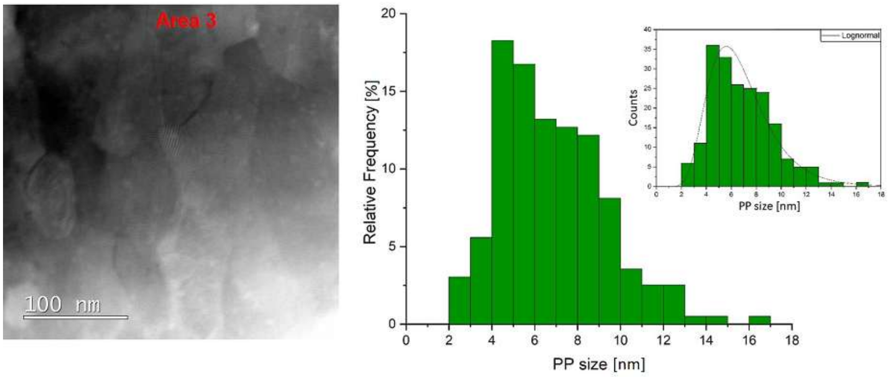

Figure 3.35: HAADF-STEM image representing the HfO$_2$ PP distribution in Area 3 (left) and statistics of PP size distribution (right); the graph on top right represents the obtained lognormal distribution fit.

Considering the PP size values obtained by lognormal distribution fit for these three areas, we found (5.7 ± 1.5) nm to be the average PP size for S2, which is totally in line with the found average median value (5.6).
The average PP density for this sample is 20405 μm^{-3}.

S3

Area 1 in Figure 3.36 was found to have a size of 647 nm × 647 nm. The averaged thickness of this area is 49 nm. The number of PP counted in this area is 910. From the histograms showing the PP size distribution, we observed a modal value of (4.5 ± 0.5) nm and considered (5.3 ± 1.5) nm as mean value of the PP size determined by lognormal distribution fit.

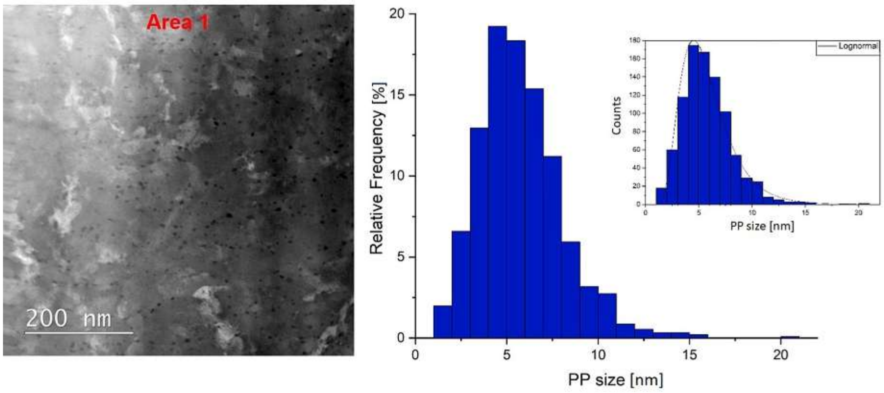

Figure 3.36: HAADF-STEM image representing the ZrO_2 PP distribution in Area 1 (left) and statistics of PP size distribution (right); the graph on top right represents the obtained lognormal distribution fit.

Area 2 in Figure 3.37 was found to have a size of 653 nm × 653 nm. The averaged thickness of this area is 41 nm. The number of PP counted in this area is 300. From the histograms showing the PP size distribution, we observed a modal value of (3.5 ± 0.5) nm and considered (4.1 ± 1.5) nm as mean value of the PP size determined by lognormal distribution fit.

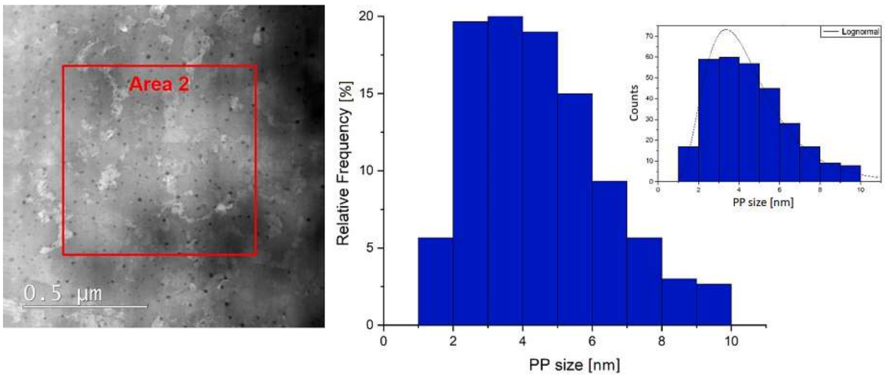

Figure 3.37: HAADF-STEM image representing the ZrO_2 PP distribution in Area 2 (left) and statistics of PP size distribution (right); the graph on top right represents the obtained lognormal distribution fit.

Area 3 in Figure 3.38 was found to have a size of 647 nm × 647 nm. The averaged thickness of this area is 66 nm. The number of PP counted in this area is 421. From the histograms showing the PP size distribution, we observed a modal value of (3.5 ± 0.5) nm and considered (3.2 ± 1.5) nm as mean value of the PP size determined by lognormal distribution fit.

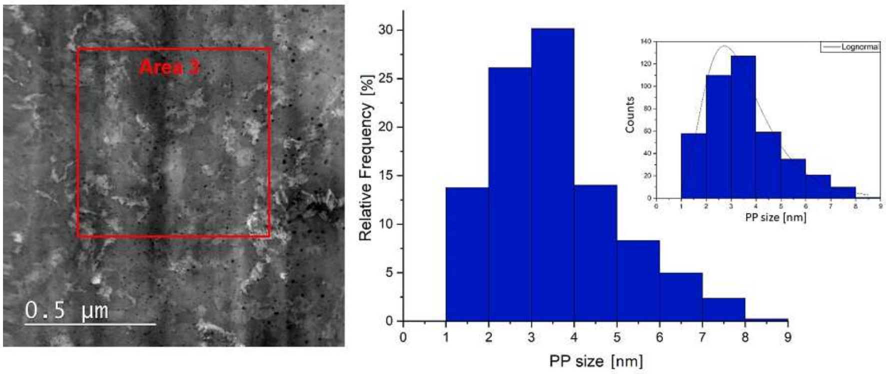

Figure 3.38: HAADF-STEM image representing the ZrO$_2$ PP distribution in Area 3 (left) and statistics of PP size distribution (right); the graph on top right represents the obtained lognormal distribution fit.

Considering the PP size values obtained by lognormal distribution fit for these three areas, we found (4.2 ± 1.5) nm to be the average PP size for S3, which is totally in line with the found average median value (4.4).
The average PP density for this sample is 19560 μm^{-3}.

S4

Area 1 in Figure 3.39 was found to have a size of 230 nm × 230 nm. The averaged thickness of this area is 55 nm. The number of PP counted in this area is 279. From the histograms showing the PP size distribution, we observed a modal value of (3.5 ± 0.5) nm and considered (4.6 ± 1.5) nm as mean value of the PP size determined by lognormal distribution fit.

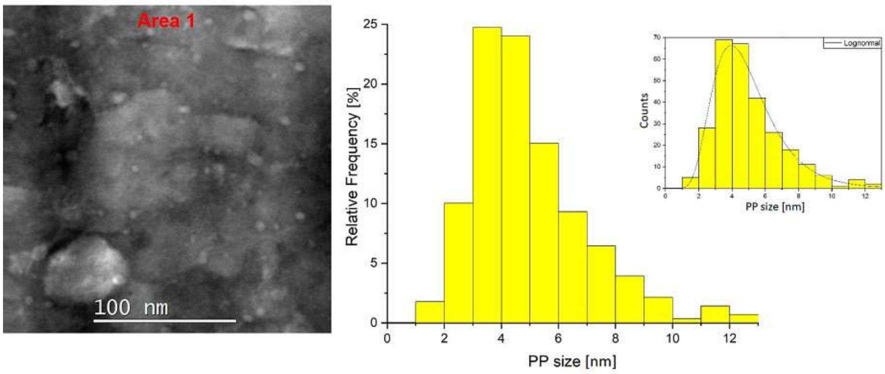

Figure 3.39: HAADF-STEM image representing the HfO_2 PP distribution in Area 1 (left) and statistics of PP size distribution (right); the graph on top right represents the obtained lognormal distribution fit.

Area 2 in Figure 3.40 was found to have a size of 647 nm × 647 nm. The averaged thickness of this area is 45 nm. The number of PP counted in this area is 201. From the histograms showing the PP size distribution, we observed a modal value of (7.5 ± 0.5) nm and considered (7.4 ± 1.5) nm as mean value of the PP size determined by lognormal distribution fit.

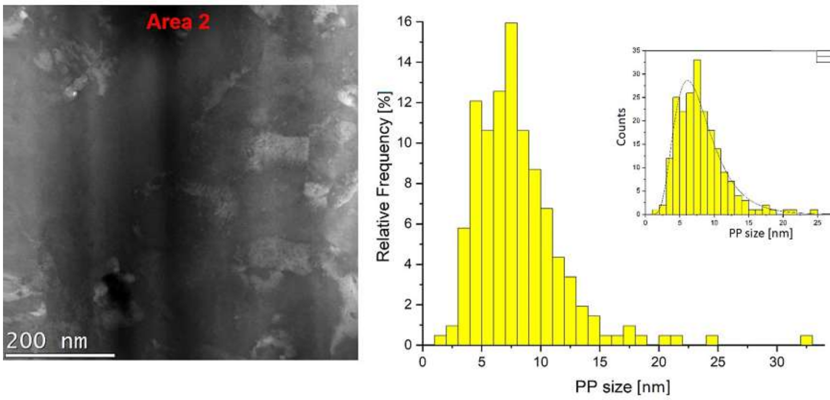

Figure 3.40: HAADF-STEM image representing the HfO_2 PP distribution in Area 2 (left) and statistics of PP size distribution (right); the graph on top right represents the obtained lognormal distribution fit.

Area 3 in Figure 3.41 was found to have a size of 323 nm × 323 nm. The averaged thickness of this area is 31 nm. The number of PP counted in this area is 140. From the histograms showing the PP size distribution, we observed a modal value of (3.5 ± 0.5) nm and considered (4.6 ± 1.7) nm as mean value of the PP size determined by lognormal distribution fit.

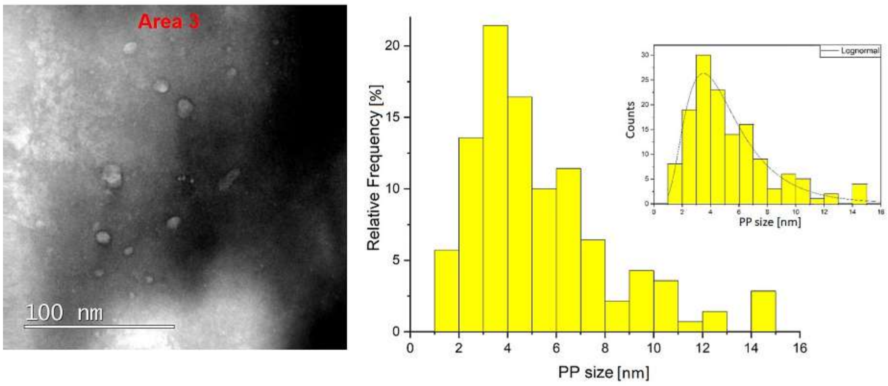

Figure 3.41: HAADF-STEM image representing the HfO_2 PP distribution in Area 3 (left) and statistics of PP size distribution (right); the graph on top right represents the obtained lognormal distribution fit.

Considering the PP size values obtained by lognormal distribution fit for these three areas, we found (5.5 ± 1.6) nm to be the average PP size for S4, which is totally in line with the found average median value (5.5).
The average PP density for this sample is 11077 μm^{-3}.

S5

Area 1 in Figure 3.42 was found to have a size of 323 nm × 323 nm. The averaged thickness of this area is 48 nm. The number of PP counted in this area is 140. From the histograms showing the PP size distribution, we observed a modal value of (3.5 ± 0.5) nm and considered (4.7 ± 1.6) nm as mean value of the PP size determined by lognormal distribution fit.

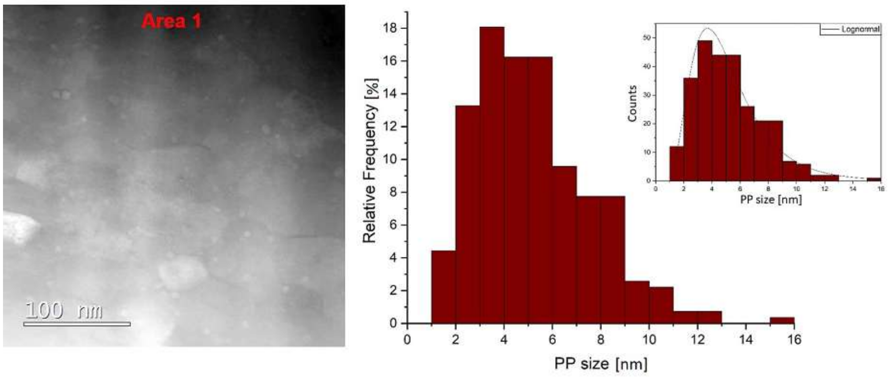

Figure 3.42: HAADF-STEM image representing the HfO_2 PP distribution in Area 1 (left) and statistics of PP size distribution (right); the graph on top right represents the obtained lognormal distribution fit.

Area 2 in Figure 3.43 was found to have a size of 323 nm × 323 nm. The averaged thickness of this area is 53 nm. The number of PP counted in this area is 140. From the histograms showing the PP size distribution, we observed a modal value of (4.5 ± 0.5) nm and considered (5.2 ± 1.5) nm as mean value of the PP size determined by lognormal distribution fit.

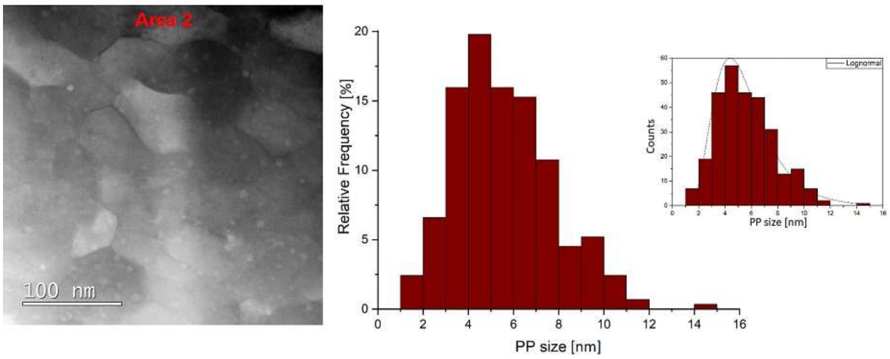

Figure 3.43: HAADF-STEM image representing the HfO_2 PP distribution in Area 2 (left) and statistics of PP size distribution (right); the graph on top right represents the obtained lognormal distribution fit.

Area 3 in Figure 3.44 was found to have a size of 323 nm × 323 nm. The averaged thickness of this area is 38 nm. The number of PP counted in this area is 140. From the histograms showing the PP size distribution, we observed a modal value of (3.5 ± 0.5) nm and considered (4.9 ± 1.6) nm as mean value of the PP size determined by lognormal distribution fit.

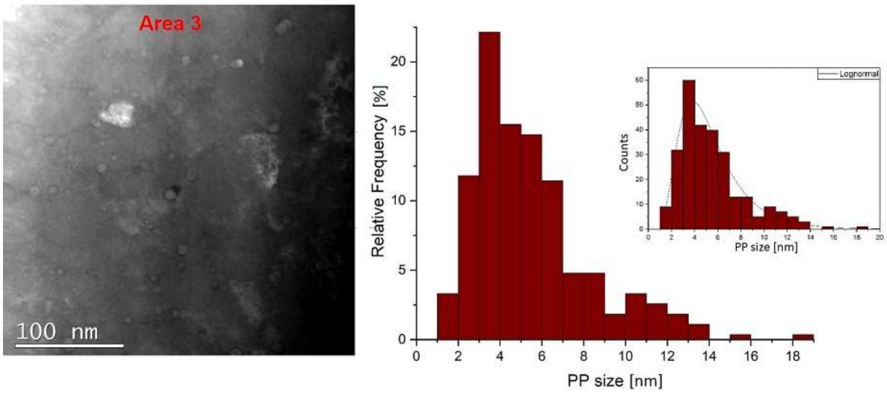

Figure 3.44: HAADF-STEM image representing the HfO_2 PP distribution in Area 3 (left) and statistics of PP size distribution (right); the graph on top right represents the obtained lognormal distribution fit.

Considering the PP size values obtained by lognormal distribution fit for these three areas, we found (4.9 ± 1.6) nm to be the average PP size for S5, which is totally in line with the found average median value (5).
The average PP density for this sample is 50089 μm^{-3}.

Table 3.6 summarizes the average size and density of PP for all five samples. It also shows the heat treatments to have a direct view of the behaviour of PP size and density according to the changes in the heat treatment. The density values are generally comparable, but higher for the wires with HfO_2 nanoprecipitates and higher heat treatment temperatures. Figure 3.45 shows the trend in PP size as the temperature and duration of heat treatment change. The size values obtained are actually very similar to each other within the limit of measurement accuracy, so we cannot draw specific conclusions. However, we found these values to be comparable to those of analogous analyses on the same type of samples [141].

Wire	S1	S2	S3	S4	S5
PP size [nm]	6.4 ± 1.8	5.7 ± 1.5	4.2 ± 1.5	5.5 ± 1.6	4.9± 1.6
PP density [μm^{-3}]	10637	20405	19560	11077	50089
Heat treatment [°C]	675 °C, 380 h	685 °C, 228 h	700 °C, 71 h	675 °C, 317 h	700 °C, 120 h

Table 3.6: Size and density of PP for the five APC-Nb_3Sn wires.

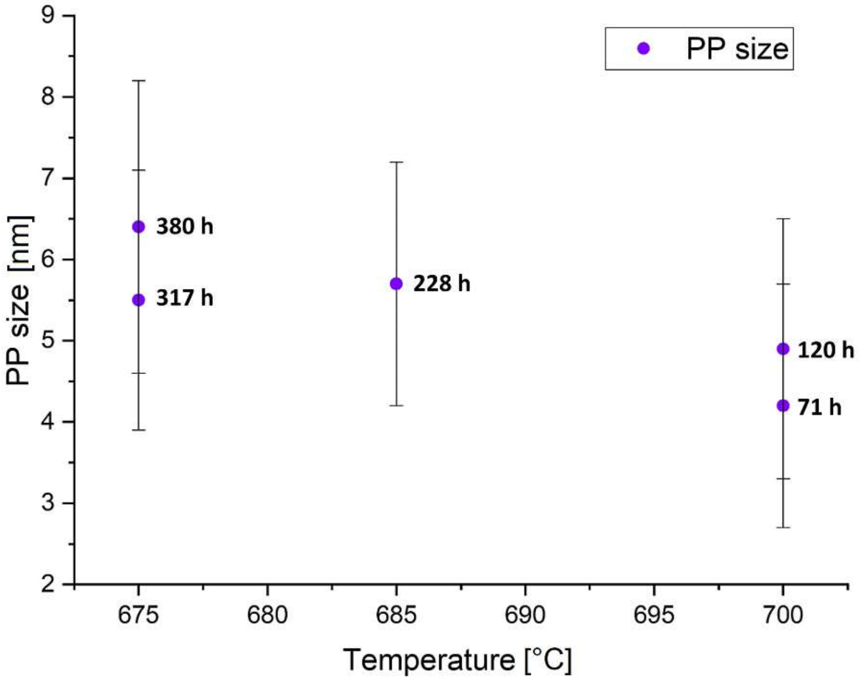

Figure 3.45: PP size (nm) vs Temperature (°C): trend in PP size as the temperature and duration of heat treatment change.

As mentioned in the section on grain size analysis, these results can also be considered as preliminary. In fact, more samples and lamellae per sample (thus higher statistics) would be needed to have a more thorough understanding of the PP size and density dependence on heat treatment changes. For this reason it is not yet possible to establish which type of nanoprecipitate (ZrO_2/HfO_2) leads to better results in terms of PP size-density and grain size. These outcomes will therefore help to complete a wider study currently underway on the newly arrived samples.

3.3 Summary and outlook

In the challenging project concerning the realization of the CERN future hadron collider (FCC-hh), Nb_3Sn represents the best candidate for the construction of high-field superconducting dipole magnets, since it is currently the most cost-effective material able to satisfy the requirements of J_c (non-Cu) = 1.5 kA/mm2 at 16 T and 4.2 K (see Figure 3.46).

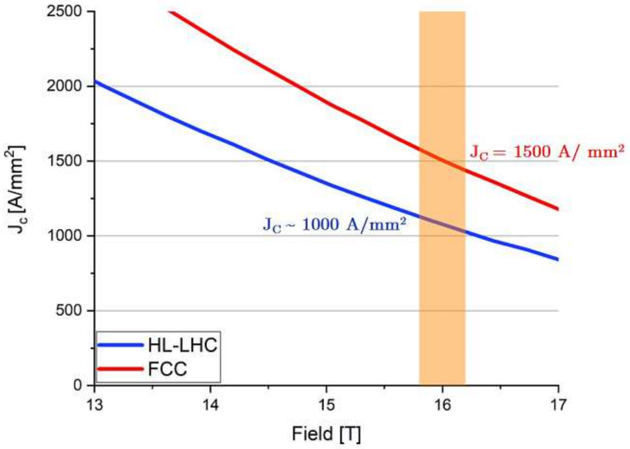

Figure 3.46: J_c of state-of-the-art wires (between 1000 A/mm^2 and 1200 A/mm^2) compared to the FCC target (1500 A/mm^2). *Graph adapted from [23].*

In this context, a three-cluster layout of prototype internal tin Nb_3Sn wires, developed by TVEL and the Bochvar Institute (Russia), was analyzed and compared to a standard layout produced by the same manufacturer with the same heat treatment (see Table 3.1 and Table 3.2). Typically, the main reason for dividing the sub-element into clusters is to reduce the effective sub-element size (d_{eff}) [117], [118], [119], [116].Our idea in this work was to try to understand if cluster layouts, due to Nb-free routes in their starting sub-elements (before heat treatment), can lead the Sn concentration gradient over the wire cross-section to be smaller. It is in fact known that the homogeneity in Sn concentration influences the wire superconducting properties [18], [19], [20]. We also compared two TVEL/Bochvar Institute wires showing the same six-cluster layout but reacted with different heat treatments (see Table 3.1 and Table 3.3): we could therefore face the Sn gradient investigation from another perspective, not only related to another cluster layout type but also influenced by the heat treatment. We think that exploring the microstructure of such cluster layouts could provide interesting contributions to steer the manufacturing processes towards more homogeneous and higher performing wires. We evaluated the effect of cluster and standard layouts on the Sn concentration gradient over the wire cross-section by employing energy dispersive X-ray (EDX) spectroscopy with both scanning electron microscopy (SEM) and transmission electron microscopy (TEM). Furthermore, we performed scanning Hall probe microscopy (SHPM) measurements to understand how these cluster sub-elements, with their specific geometry, influence the local currents flowing through the wire cross-section on a microscopic scale.

The EDX results observed for the cluster layout samples suggest a high potential in terms of radial homogeneity. Catalyzing Sn diffusion through the Nb-free Cu channels towards the peripheral barrier can therefore be an effective way to produce wires with a more homogeneous Sn distribution, an optimized average Sn content, and a resulting higher superconducting performance. Moreover, the local currents evaluated from SHPM show a J_c consistent with the HL-LHC standards, which can be further improved by acting on the manufacturing process steps and the heat treatment parameters. Future studies on different cluster-type samples reacted with the same heat treatment would be very useful to take a further step into the comprehension of cluster role in producing more homogeneous wires.

Beside the study on cluster wires, main focus of this thesis work, we also analyzed five internally oxidized APC Nb_3Sn wires produced by Hyper Tech Inc. (Ohio, US). We wanted to explore the physics behind the high-performance this wire type usually shows ([136], [70], [139], [140]) by observing eventual microstructural changes due to different dopants (Zr and Hf), and heat treatment differences in terms of temperature and time. STEM-HAADF and SEM-TKD analyses were carried out to evaluate respectively size and density of the nanoprecipitates (PP) characterizing such samples (ZrO_2/HfO_2), and the grain size.

Our main objective was to study the correlations between PP size-density and heat treatment, and Nb_3Sn grain size and heat treatment. We also sought to understand which typology of nanoprecipitate (ZrO_2 or HfO_2) led to better results. The outcomes of this analysis were consistent with previous similar studies [141], although not yet representative of the dependence of the wire properties on the heat treatment performed and nanoprecipitate type. In fact, this investigation is part of a work which is currently in progress as new samples have recently arrived. The obtained results can thus be considered as preliminary. More samples and lamellae per sample (thus higher statistics) would be needed to have a more thorough understanding of the grain size, and PP size and density dependence on heat treatment. The here described analyses will therefore help to complete the study currently underway on the newly arrived samples. Once completed, such a study can provide a great contribution in exploring the high performance of the internally oxidized APC wire type, which seems to represent a promising technology for superconducting magnets of future applications, both in the medical and high-energy physics fields.

4 Tl1223 for the FCC-hh beam screen

4.1 Purpose of microstructural characterization

As mentioned in Chapter 1, the production of Tl-1223 thin films is very challenging as Thallium is toxic by nature and highly volatile. The sample preparation performed at CNR-SPIN (see Chapter 1) involved an electrochemical deposition [151], [152], [26] on both Ag and $SrTiO_3$ (STO) substrates for the production of the precursor films, and a heat treatment at temperatures close to 900 ° C for the formation of the final phase. The samples were thus processed in a three-zone tubular furnace at 885°C for ten minutes [26]: in particular, precursor films were kept in a gold foil crucible, along with Tl_2O_3 powder (4 mg), and Tl-1223 pellets for the so called "thallination process" [26]. Using such a system allows the sample to be maintained in a thallium atmosphere, considering that thallium oxide is volatile above 710°C. Our electron microscopy analyses therefore aimed at assessing the formation of the desired phase Tl-1223 and the quality of the substrate coverage. Furthermore, as precursor-pellets or -bulks used for the thallination process were expected to be almost pure Tl-1223, we also characterized their microstruture by employing both SEM and TEM. Precursor-pellets synthesis is described in detail in [26].

In a second step of Tl-1223 film preparation, only Tl_2O_3 powder was used during the thallination process. We therefore analyzed and compared samples obtained through this new thallination process, but for which a different amount of Tl_2O_3 powder was used.

In this way we were able to follow and evaluate the progress of the Tl-1223 film production process conducted at CNR-SPIN.

4.1.0.1 SEM analysis

We carried out a SEM-EDX investigation on the precursor-pellets and on the Tl-1223 thin films produced with different thallination methods. At this end, we used the following microscope settings: a working distance of 10 mm, an electron beam energy of 20 keV, an aperture of 30 μm, and a beam spot size of approx. 4 nm. For recording EDX maps, we selected an image resolution of 256 × 200 pixels, a dwell time of 200 μs per frame. We accumulated 20 frames per image for obtaining accurate EDX maps. For EDX point analysis, we typically selected a dwell time of 100 s.

4.1.0.2 TEM analysis

We performed TEM-EDX mapping survey on the precursor-pellets and for the recorded maps we had the following microscope settings: an electron beam energy of 200 keV, the detector tilted of 25° towards the EDX detector, a beam spot of 5 corresponding to a beam diameter of approx. 1.3 nm, an image resolution of 256 × 200 pixels, and an amplification time of 3.84 μs. The selected spot size is a good compromise between small beam size (for high resolution analysis) and a good signal to noise ratio (to have a reliable analysis). The aforementioned "amplification time" (or process time) is the time given to the pulse processor to evaluate the incoming charge pulse and is related to the resolution of the output EDX spectrum (see the subsections dedicated to EDX operation in Chapter2). Again, it is good to select an amplification time that represents a good compromise between high spectral resolution and low "dead time" (intended as excess time spent by the processor in evaluating the pulse - see subsection 2.2.2. of Chapter2). For the EDX mapping surveys and related data analysis we used the TEAM Software of EDAX-AMETEC Inc.

4.2 Results and discussion

We first evaluated the formation of the Tl-1223 phase in the precursor-pellets, as ingredients intended to maintain a thallium atmosphere (along with 4 mg Tl_2O_3 powder) during heat treatment and to help obtain the desired Tl-1223 phase in the deposited films. We then studied the thin films produced in this manner, not only in terms of phase formation but also in terms of substrate coverage. We will refer to such samples as "type 1". We performed the same microstructural characterization on more recently produced films, obtained through a pellet-free thallination process using only Tl_2O_3 powder. We will call these "type 2". Finally, we will report the results obtained on "type 3" films produced by this last thallination method (without pellets) but with a different amount of Tl_2O_3 powder than the type 2 samples. Please note that the exact amounts of Tl_2O_3 powder used in the thallination processes of type 1 and type 2 samples will not be disclosed due to confidentiality concerns.
All produced films showed a thickness between 1 μm and 2 μm. Table 4.1 summarizes the three types of samples.

Designation	type 1	type 2	type 3
Sample	STl019_6 STl019_12 STl019_13	Tl24a_02 Tl_24b 04 Tl_24d	STl027_Ag STl027_STO
Substrate	STO	Ag	both Ag and STO
Thallination method	Pellet + Tl_2O_3 powder	Tl_2O_3 - amount X	Tl_2O_3 - amount Y

Table 4.1: Overview of the three types of thin film characterized in terms of their microstructure.

4.2.0.1 SEM analysis

Since Tl-1223 is actually representing (Tl,Bi)(Pb,Ba,Sr)$_2$Ca$_2$Cu$_3$O$_x$, we investigated the presence of all those elements in our EDX-analyses. Among those working with EDX, it is well known that quantitative SEM-EDX estimates of oxygen (relatively light atom) in oxides cannot be reliably obtained by directly measuring the oxygen peak [153]. EDX detectors are conventionally not efficient at measuring soft X-rays [153]. In addition, EDX is sensitive to contamination and oxidation, which definitely plays a role in quantifying oxygen. In light of this, we did not consider oxygen in our quantitative analyses. As previously explained, we first performed out SEM-EDX investigation on precursor-pellets used to produce type 1 samples. Figure 4.1 is showing the overview and typical aspect of the analyzed precursor-pellets. The visible dark areas represent Si-rich areas.

It is worth noting that most of the SEM images were taken using the BSE detector which allowed us to better distinguish the grain structure of the three film types. Some images were taken with the SE detector (ETD) as the BSE detector has been unavailable for a long time.

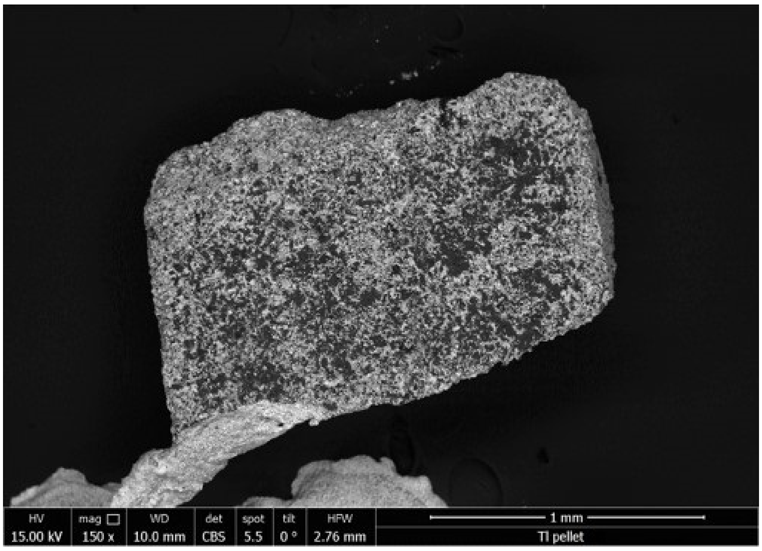

Figure 4.1: Overview SEM image taken with the ETD and showing the overview aspect of an analyzed precursor-pellet.

An example of pellet region with both Si-rich dark areas and holes is exhibited in Figure 4.2. They were easily distinguishable from each other as the Si-rich areas clearly covered the pellet grains. This is also an exemplary type of area where we found plate-like grains somehow disorderly clustered together. Si- and O-rich spots, which have a low average atomic number, are easily visible using the BSE detector (material contrast, see Chapter 2) and result as dark areas in the selected image.

The investigated pellets mostly showed regions of nearly perfect straight parallelepiped-like grains (Figure 4.3). Both types of grains (clustered plate-like grains and straight parallelepipeds) showed either an evident Tl-1223 phase or close to Tl-1234. The latter was found in the plate-like grains of Figure 4.2, as shown by the results in Table 4.2. The reason behind the presence of a phase close to Tl-1234 could be due to copper substituting thallium on its site. The total copper would therefore result in excess. As a counterevidence, we cut a FIB lamella in a region that apparently showed Tl-1234 grains and performed TEM-EDX measurements to see if we still get a Tl-1234-like phase. This analysis will be described in the next section dedicated to TEM-EDX.

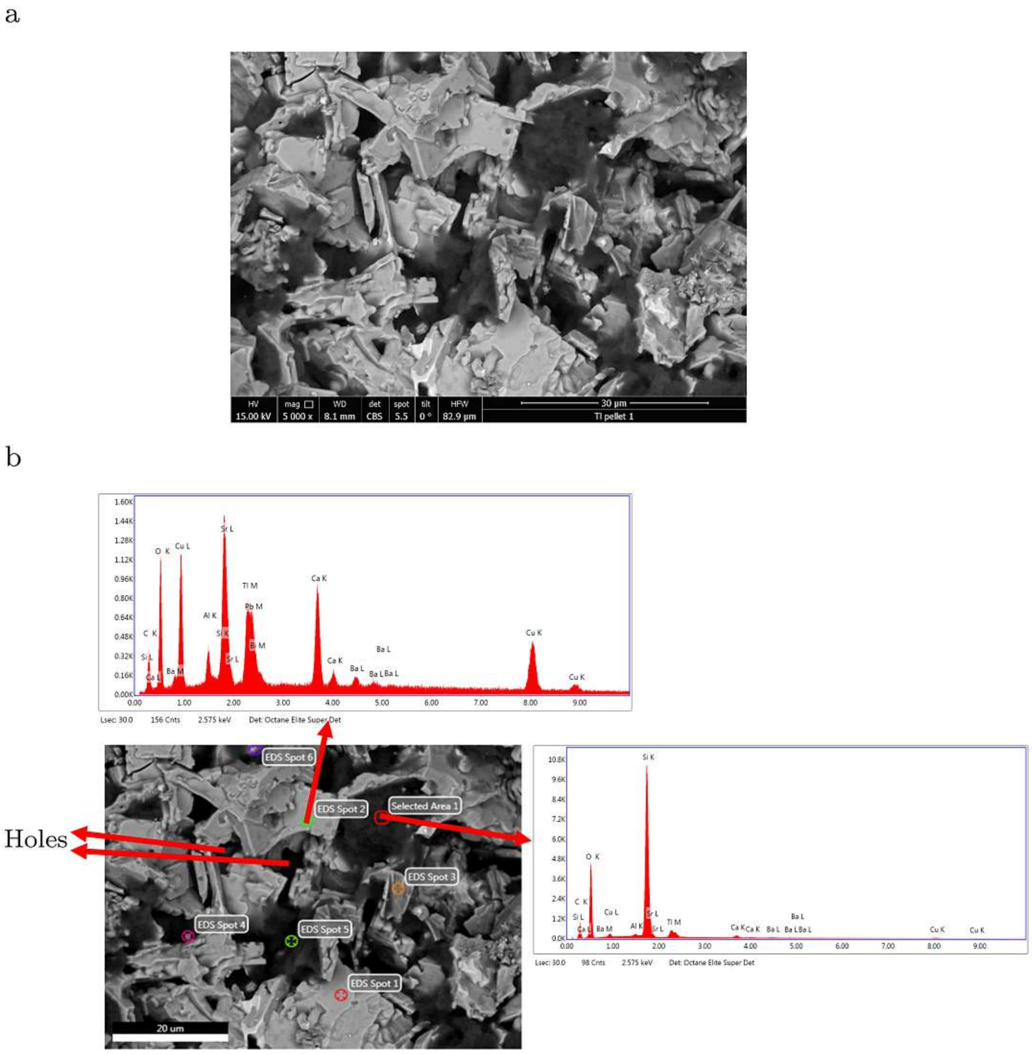

Figure 4.2: SEM images taken with the BSE detector. Example of pellet region (a) with both Si-rich areas and holes. In the EDX-survey image (b) some point measurements are shown for both plate-like grains (EDX spectrum on top of the image) and Si-rich areas (EDX spectrum on the right).

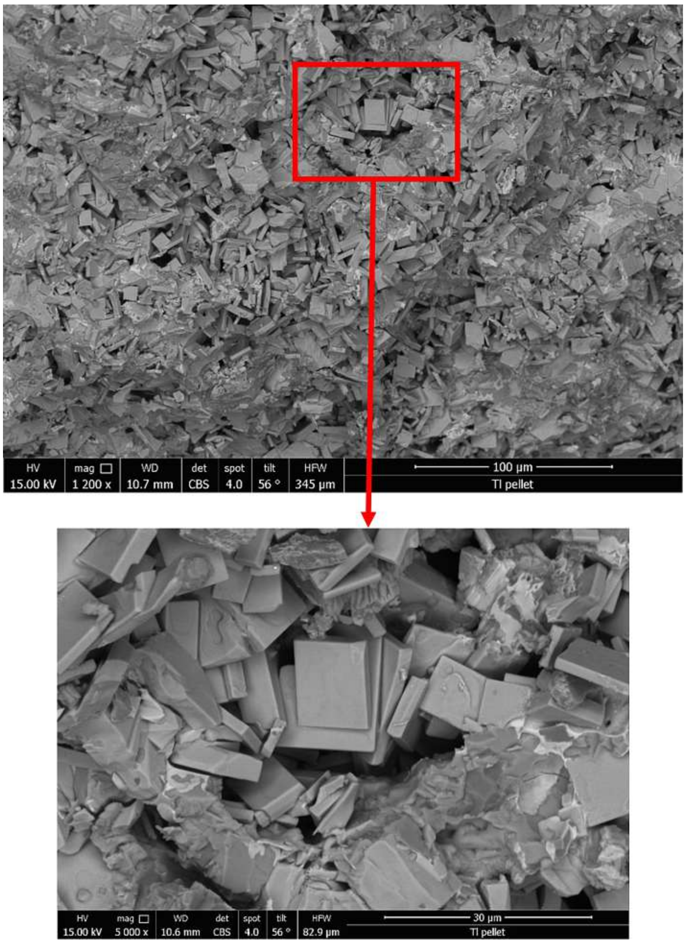

Figure 4.3: Overview of a typical precursor-pellet taken with the BSE detector.

Element	Nominal comp. 1223 [at%]	Nominal comp. 1234 [at%]	EDX outcomes
Tl, Pb, Bi	12.5	10	10.2
Sr, Ba	25	20	23.3
Ca	25	30	29.3
Cu	37.5	40	37.2

Table 4.2: EDX point analysis: our outcomes compared to the nominal composition of Tl-1223 phase [at%] and that of Tl-1234 phase [at%].

After precursor-pellet analysis, we analyzed the type 1 samples to evaluate the efficiency of a thallination method using pellets.Figure4.4 shows the overview of a typical thin film sample received. Since the electrodeposition system used had a circular shaped mask, we could clearly distinguish this shape in all sample overviews. It is highlighted by the dashed red line in Figure4.4, representing sample STL019_6. From this image, one can already see how challenging the production process of films can be, especially when it comes to achieving uniform coverage of the substrate.

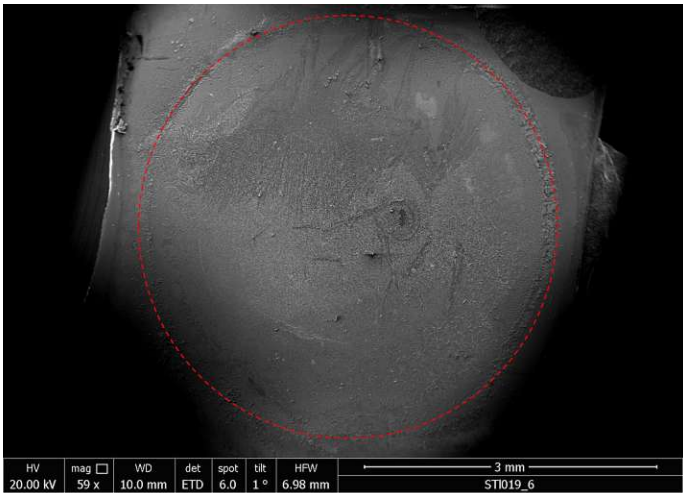

Figure 4.4: Overview of sample STl019_6 also presenting the typical circular shape (drawn by the dotted red line) due to the circular mask of the used electrodeposition system. This SEM image was taken with the ETD.

All analyzed samples belonging to the STl019 series exhibited inhomogeneous coverage and regions where substrate was clearly visible.
Some samples, such as STl019_6, showed elongated structures (between 40 and 130 μm in length) distributed over the entire surface, which we found to be characterized by the desired Tl-1223 phase (Figure 4.5). These structures appeared to be immersed in a matrix consisting of elements of various shapes and predominantly rich in copper and calcium (the darker ones) or barium (the brighter ones).

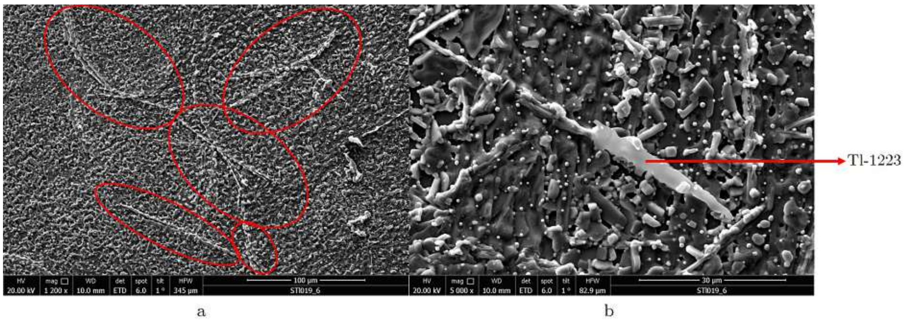

Figure 4.5: A typical area observed in sample STl019_6: (a) SEM image showing the elongated structures (red circles) characterized by Tl-1223 phase; (b) close-up of an elongated structure immersed in a matrix where elements of various shapes are observable. Specifically, the brighter ones are Ba-rich whereas the darker ones Cu-/ Ca-rich. These SEM images were taken with the ETD.

One aspect that we found in all type 1 films concerns the presence of pieces of pellets dispersed on the surface and some ”aggregates” rich in zirconium. Figure 4.6 shows a region of sample STl019_12 where some pieces of pellets are circled in red and some aggregates in yellow. The presence of pellet remnants clearly stems from the fact that they were used during the thallination process. The reason behind the presence of zirconium remains instead doubtful, but could be related to the felt that was used at CNR-SPIN used as support to the substrate during the heat treatment.

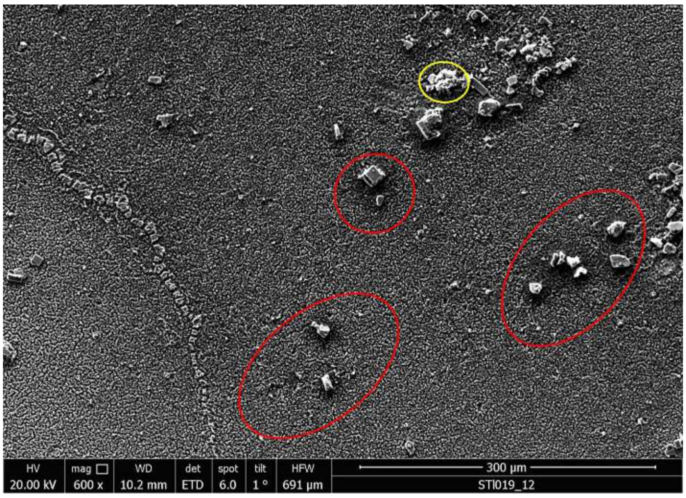

Figure 4.6: Example of region showing pieces of pellets (some of them circled in red) and ”aggregates” rich in zirconium (circled in yellow), which we observed in all type 1 samples. This SEM image was taken with the ETD.

As shown for sample STl019_12 in Figure4.7, some regions were found with small round and rectangular shaped elements (size between 500 nm and 2 μm), mainly rich in -Sr and -Tl (the brightest), and rich in -Cu and -Ca (the darkest). No spots in that region revealed the Tl-1223 phase of interest.

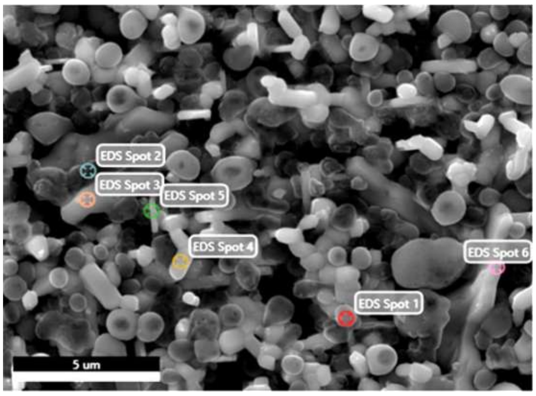

Figure 4.7: SEM image (magnification: 20000x) taken with the ETD detector showing a region with small round and rectangular shaped elements mainly rich in -Sr and -Tl (the brightest), and in -Cu and -Ca (the darkest).

In some cases, such as for sample STl019_13, we saw thinner areas with parts of the substrate clearly visible (Figure 4.8a) next to thicker areas (Figure 4.8b) with no visible substrate. We found a phase composition close to Tl-1223 in the elongated structures of the thinner areas, while in the thicker areas we found mainly Cu-/ Ca- /Sr-rich areas and some agglomerates of about 5 μm (EDS Spot 6 in Figure 4.8b - right) showing the desired Tl-1223 phase.

Type 1 thin films proved therefore to be inhomogeneous in terms of thickness, coverage of the substrate (clearly visible in different regions), also presenting impurities, and randomly oriented grains of various shapes (very often rich in Cu, Ca, Sr or Ba). However, we found the Tl1223 phase of interest in elongated structures spread over the entire surface and in some agglomerates of about 5 μm.

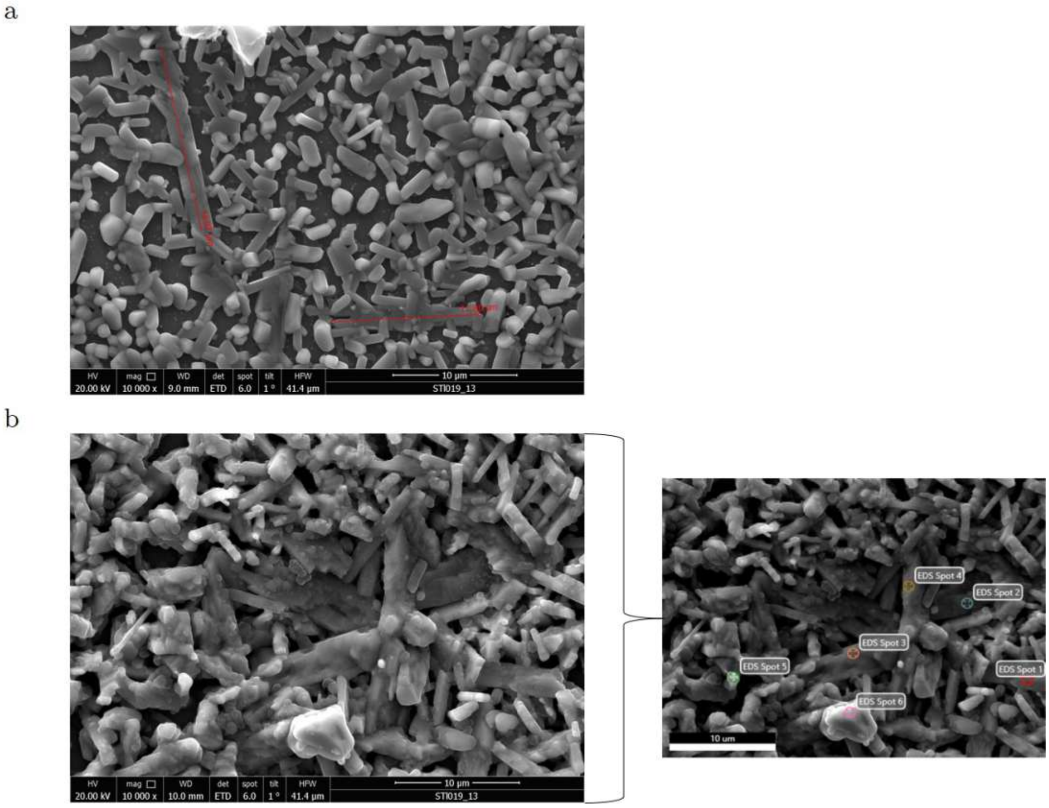

Figure 4.8: (a) Example of a region, wher the substrate is not fully covered. Here, elongated structures between 10 and 15 μm in size can be observed where we found a phase composition similar to Tl-1223. (b) Thick region with no visible substrate surface. The image on the right represents some of the performed EDX point measurements: we found the desired Tl-1223 phase on agglomerates of approx. 5 μm, such as the one labeled ”EDS Spot 6”. These SEM images were taken with the ETD.

We then analyzed the new sets of films from a pellet-free thallination method, starting with type 2 samples.

As the overview image of Tl24a_02 in Figure 4.9a shows, these samples mostly showed poor coverage of the Ag substrate. In fact, the grain boundaries of the substrate were easily distinguishable. We found mainly plate-like grains ranging in size from 30 to 200 μm, some Sr-rich agglomerates (light blue circle in Figure 4.9b), and C-rich impurities (yellow circle in Figure 4.9b).

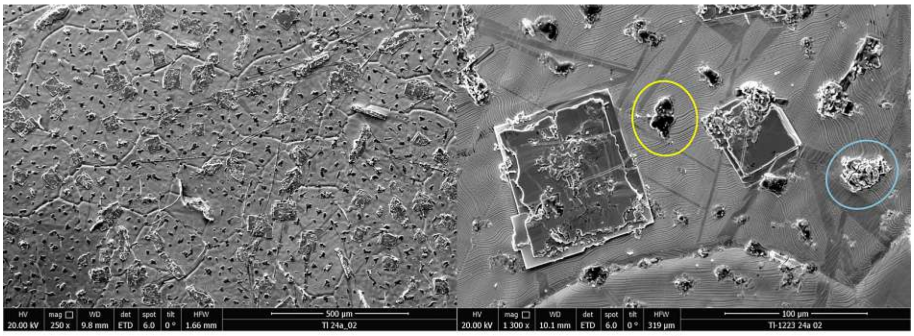
a b

Figure 4.9: (a) Overview image of a typical type 2 thin film where the substrate with its grain boundaries is clearly visible; (b) Close-up of an area with plate-like grains, C-rich impurities and Sr-rich agglomerates. These SEM images were taken with the ETD.

By analyzing several regions with plate-like grains via EDX mapping, we mainly found the presence of the Tl1212 phase. These were, specifically, grains of Tl-1212 superimposed on grains of Tl-1223. In general, it should be noted that the formation of the Tl-1212 phase is energetically favorable compared to that of Tl-1223 [154], [155] and it is therefore easily detectable in such samples. Tl-1212 is also a superconducting phase, but the Tl-1223 phase has better superconducting properties and is more promising for applications in Tl-based films [80], [155]. Figure 4.10 shows one of the plate-like grain-rich areas analyzed by EDX mapping. In addition to grains of Tl-1223 and Tl-1212, Sr- and Ca-rich regions dispersed throughout the sample surface were observed.

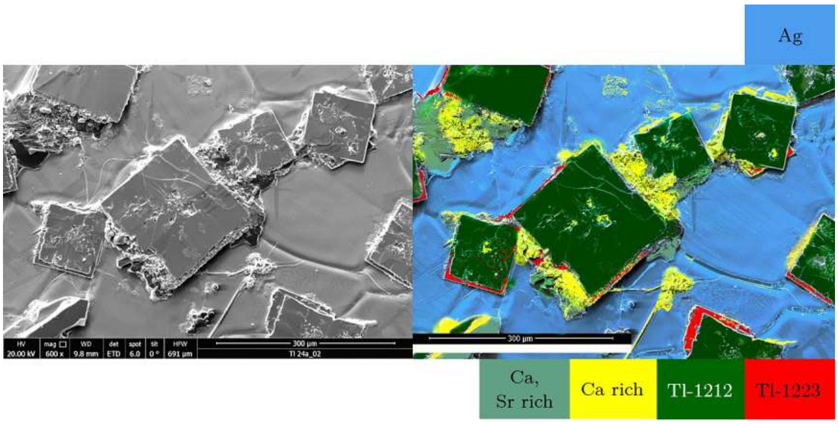

a b

Figure 4.10: (a) A typical plate-like grain-rich area and its (b) EDX mapping mainly showing Tl-1212 grains superimposed on Tl-1223 grains. Regions rich in Ca-Sr (light green) and Ca (yellow) were also observed. This SEM image was taken with the ETD.

The general appearance of sample Tl24b_04 is represented in Figure 4.11a, where we mostly found elongated structures rich in Cu and Sr and between 50 and 500 μm in length. Looking closely at some details similar to such elongated structures (dashed yellow rectangle in Figure4.11b-left), they actually turned out to be a part of a plate-like grain emerging from the substrate. In other words, a tilted plate-like grain, largely covered by Ag stemming from the substrate. This aspect of the "fake elongated structures" concerned mostly those with greater thickness (approximately 15-20 μm). The "true" elongated structures have thicknesses around 5-7 μm.

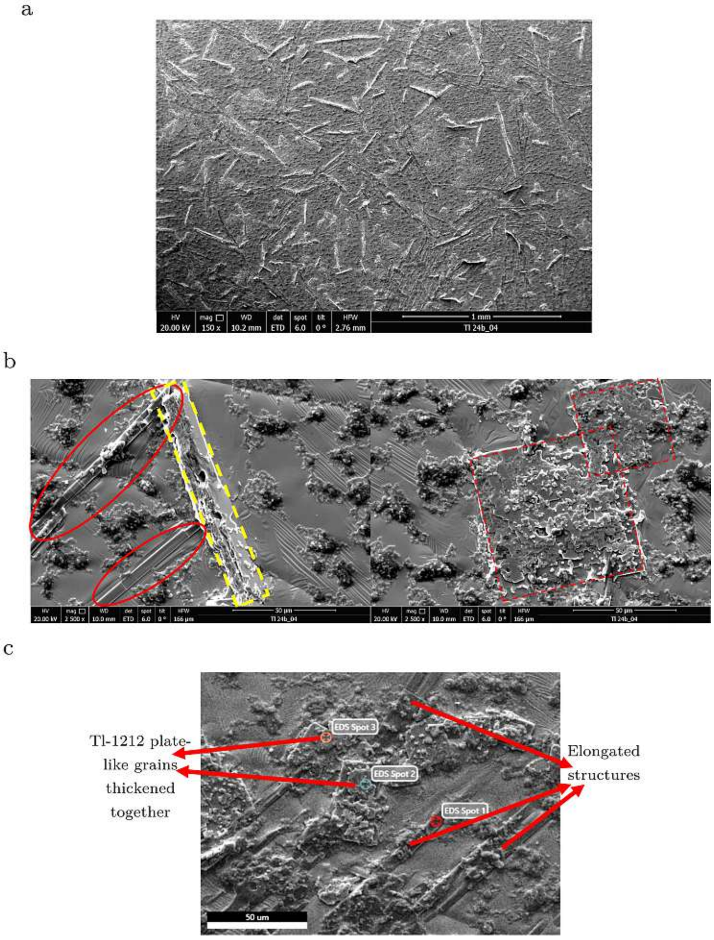

Figure 4.11: (a) Overview image of sample Tl24b_04 where mainly elongated structures are visible. The thickest ones should actually be (b) tilted plate-like grains largely covered by Ag stemming from the substrate (drawn by the dashed yellow rectangle). The red circles represent "real" elongated structures with thicknesses around 5-7 μm; (c) EDX point analysis of elongated structures and plate-like grains: the former are Cu- and Sr-rich, the latter are mostly characterized by Tl-1212 phase. These SEM images were taken with the ETD.

We also found C-rich impurities (dark agglomerates in Figure 4.11b) and plate-like grains almost thickened together (Figure 4.11b-right and Figure 4.11c). The latter were present all over the surface and by EDX analysis were found to be Tl-1212-rich. Their size ranged from 20 to 100 μm.

An overall appearance similar to that of sample Tl24b_04, characterized by elongated structures and plate-like grains sticking together, was also found for sample Tl_24d (Figure 4.12a). In particular, we observed regions with "chains" of grains thickened together (Figures 4.12b – red circle) and regions where single grains could be distiguished (Figure 4.13), in a very similar way to sample Tl24a_02.
To study more carefully the layers constituting the plate-like grains we performed EDX mappings, tilting the sample of about 40°. Figure 4.13 (right) shows the differentiation between the phases constituting the grain. A stratified structure of the grains was found, in general, in all type 2 samples. We observed a Sr-rich zone (in green), a layer clearly characterized by the Tl-1212 phase (in yellow), one in which the phase found was similar to Tl-1212 but with Cu excess (in blue), and finally, below all, a layer of the desired Tl-1223 phase (in red).

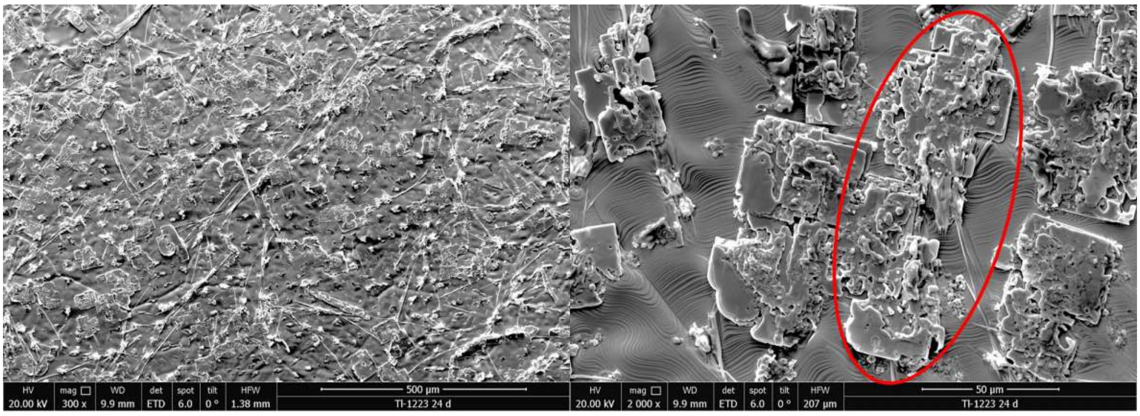

a b

Figure 4.12: (a) Overview image of sample Tl_24d, mostly characterized by elongated structures and (b) chains of plate-like grains sticking together (red circle). These SEM images were taken with the ETD.

Summarizing the type 2 thin films, they were still shown to have poor coverage as seen in the type 1 samples. They were mostly found to be characterized by elongated Cu- and Sr-rich structures, and big plate-like grains of Tl-1212 (size up to 200 μm) overlaid with grains of Tl-1223. In some cases, "tilted" grains of Tl-1212 appeared to be trying to emerge from the substrate, being largely covered by Ag. In addition, C-rich impurities were found distributed throughout the surface.
We then explored the type 3 films to see if a different amount of Tl_2O_3 powder in the thallination process had led to obvious improvements.

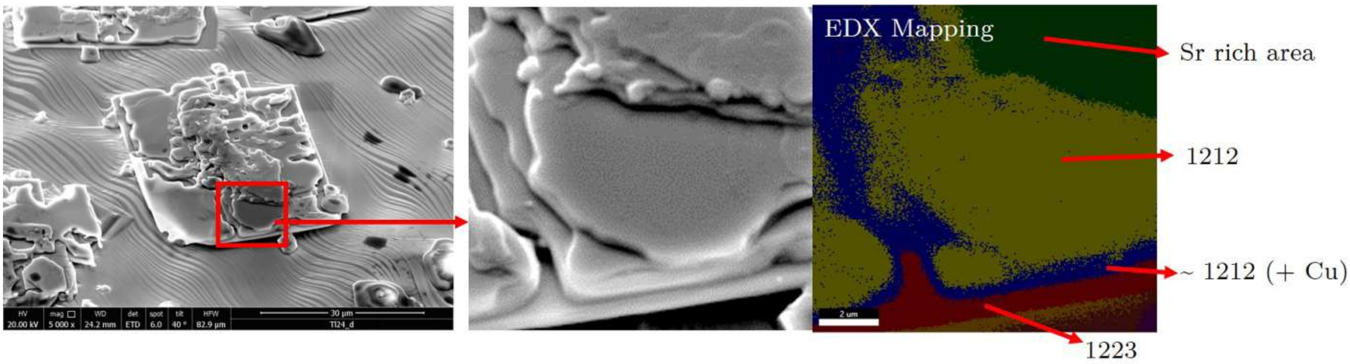

Figure 4.13: An area of Tl_24d sample representative of those regions of this film showing distinguishable "single" plate-like grains (left). EDX mapping (right) was performed to distinguish layers that characterize plate-like grains: a Sr-rich zone (in green), a layer clearly characterized by the Tl-1212 phase (in yellow), one in which the phase found was similar to Tl-1212 but with Cu excess (in blue), and a layer of the desired Tl-1223 phase (in red). These SEM images were taken with the ETD.

Type 3 samples showed overall better coverages than the previous sample types analyzed. Indeed, the substrate was less visible in both Ag and STO cases. We basically observed more plate-like grains, now smaller (size between 30 and 70 μm) than those found in the type 2 samples (size between 30 and 200 μm), less thickened with each other, and more homogeneously distributed across the film surface. Figure 4.14 shows the type 2 (a) and type 3 (b) samples compared in terms of substrate coverage. All SEM images of Figure 4.14 were taken at the same magnification.

Both type 3 films STl027_Ag and STl027_STO, deposited on Ag and STO, respectively, were shown not only to have better substrate coverage, but also to be characterized mainly by Tl-1223 plate-like grains, and only a few Tl-1212 grains. Figure 4.15 and Figure 4.16 show examples of areas investigated by EDX mapping where we always found a majority of Tl-1223-rich grains.
However, also in this case we found C-rich impurities and some areas not characterized by the desired Tl-1223 phase and showing excess amounts of other component elements of the phase of interest (see EDX maps in Figure 4.15b and Figure 4.16b).
Considering, though, how challenging it is to control the production process of such thallium-based thin films, we can say that we obtained clear improvements with type 3 samples in terms of substrate coverage and Tl-1223 phase formation.

In general, all samples produced showed grains (of various shapes in type 1 samples and plate-like for type 2 and 3 samples) disconnected and randomly oriented. However, given the improvements achieved for type 3 specimens, the study on the optimization of the film production process is going on. Further work will be done on the parameters involved in the deposition process and heat treatment to obtain films with complete substrate coverages, effective grain-to-grain connection and a presence of progressively purer Tl-1223 phase. We are confident that this study will help to demonstrate the importance that such thallium-based HTSs can have in terms of superconducting properties and, thus, future high-energy applications.

a

Type 2 samples

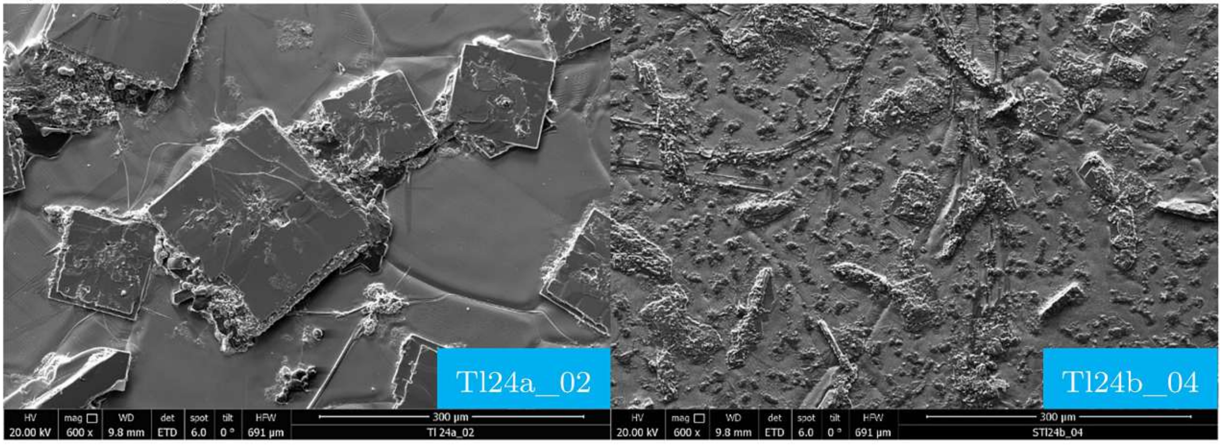

b

Type 3 samples

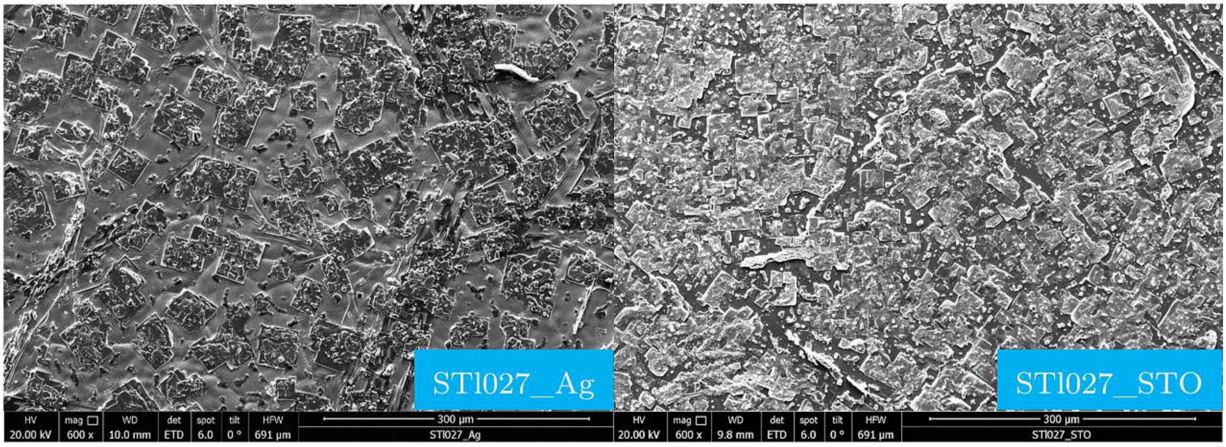

Figure 4.14: Overview SEM images (taken with the ETD and same magnification) comparing substrate coverage for type 2 (a) and type 3 (b) samples. Improvements were observed for the latter in terms of higher number of plate-like grains covering the substrate (size between 30 and 70 μm), less thickening between them, more homogeneous distribution across the surface.

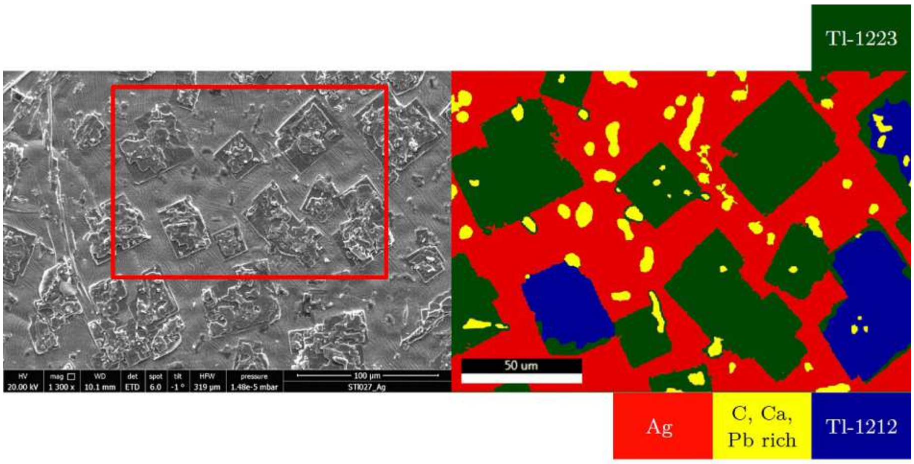

a b

Figure 4.15: (a) A typical area characterizing type 3 films deposited on Ag substrate. The red box refers to (b) one of the areas where EDX mapping was performed. We observed more Tl-1223 than Tl-1212 grains, and some areas rich in C, Ca, Pb. This SEM image was taken with the ETD.

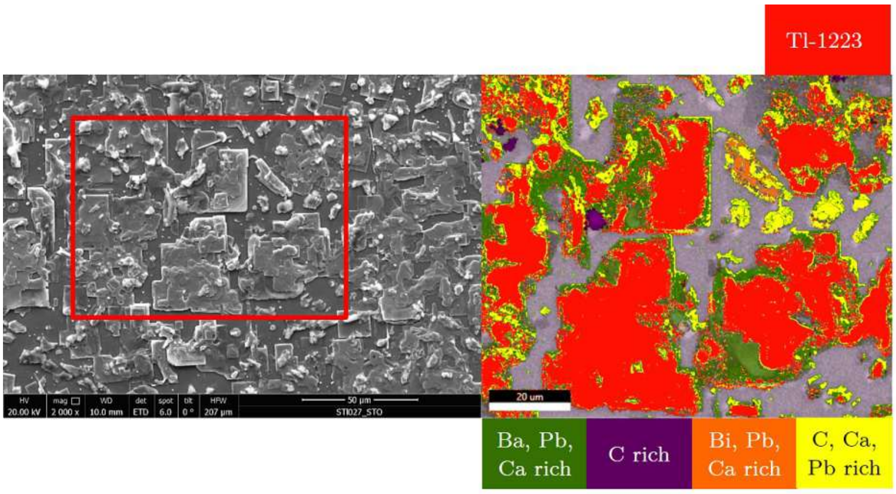

a b

Figure 4.16: (a) A typical area characterizing type 3 films deposited on STO substrate. The red box refers to (b) one of the areas where EDX mapping was performed. We observed Tl-1223 plate-like grains and some areas rich in C - Ba, Pb, Ca - Bi, Pb, Ca - C, Ca, Pb. This SEM image was taken with the ETD.

4.2.0.2 TEM analysis

Previous SEM analysis of precursor-pellets revealed that some regions had a phase composition between Tl-1223 and Tl-1234, particularly closer to Tl-1234. We therefore cut FIB lamellae from some of these areas to investigate this further. Figure 4.17 (top) shows a FIB-lamella where we performed EDX mappings. One of the mapped areas is shown as an example in Figure 4.17 (bottom). In general, we found only grains of Tl-1223 (in yellow in Figure4.17-bottom) along with a few other grains and areas rich in different component elements of the phase of interest (in red, green, and blue in Figure 4.17-bottom).

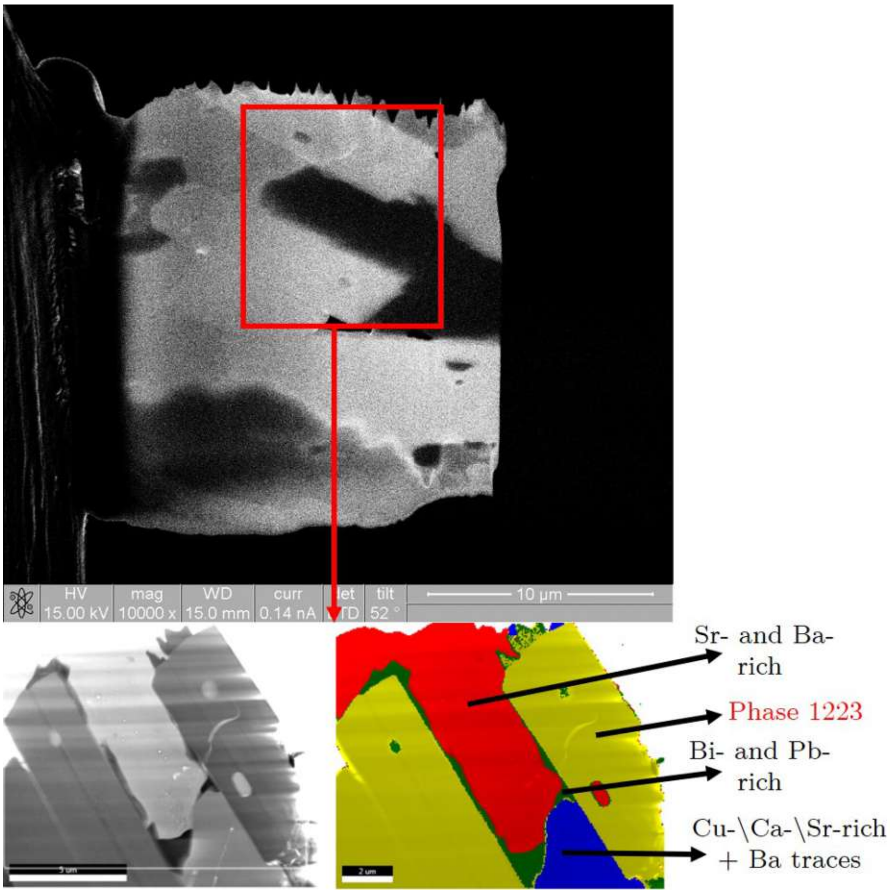

Figure 4.17: HAADF-STEM image as example of pellet-FIB lamella (top) cut from a region showing a phase composition closer to Tl-1234 than Tl-1223. At the bottom of the image a mapped area is shown: we mostly found Tl-1223 grains (yellow) along with a few other grains and spots rich in Sr and Ba (red), Cu, Ca, Sr plus Ba traces (blue), and Bi and Pb (green).

Figure 4.18 shows an EDX mapping for each element composing the Tl-1223 phase. Whenever a certain colour (representing an element) defines the shapes/details of the object having that colour, it means that a specific element is present in that given grain/point. The yellow grains of Figure 4.17-low are indeed characterized by all the elements of the phase, being coloured and well defined in each EDX mapping of Figure 4.18. Most of the elements are evidently present here: only Ba shows a "dull" coloration, especially when compared to the "bright" bluishness of the grain in the middle of those characterized by Tl-1223. If the colour is bright (Bi/Ba/Cu cases), this means that that specific grain/region is particularly rich in that element.

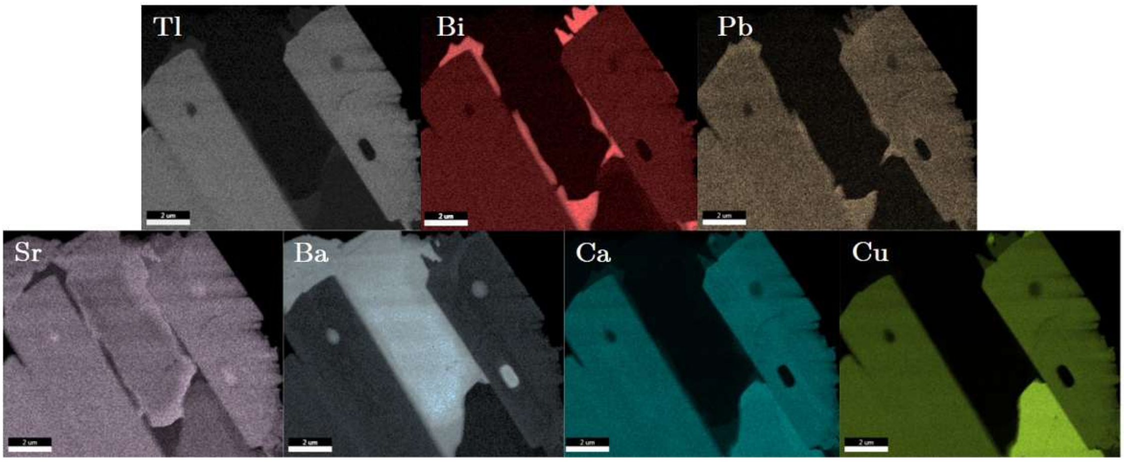

Figure 4.18: EDX mapping for each element composing the Tl-1223 phase. If a certain colour, representing a phase element, clearly defines shape/details of the object having that colour, it means that a specific element is present in that given grain/spot. Bright colours reveal areas/spots particularly rich in the elements those colours are representing.

Our TEM investigations led us to conclude that, in general, the precursor-pellets were primarily characterized by Tl-1223 grains along with a few grains and spots rich in some specific elements composing the phase of interest.

4.3 Summary and outlook

The CERN FCC-hh is expected to produce unprecedented amounts of synchrotron radiation. In order to protect its sensitive components, a superconducting beam screen is necessary, which would be kept at 50 K as shown by the beam screen working point in Figure 4.19. Two suitable candidates for the beam screen coating are the high temperature superconductors YBCO and the technologically still unexploited thallium-based cuprates Tl-1223 ($(\mathrm{Tl,Bi})(\mathrm{Pb,Ba,Sr})_2\mathrm{Ca}_2\mathrm{Cu}_3\mathrm{O}_x$). Since YBCO is expensive and has a complex preparation on large scale, Tl-1223 is currently highly taken into consideration as beam screen coating.

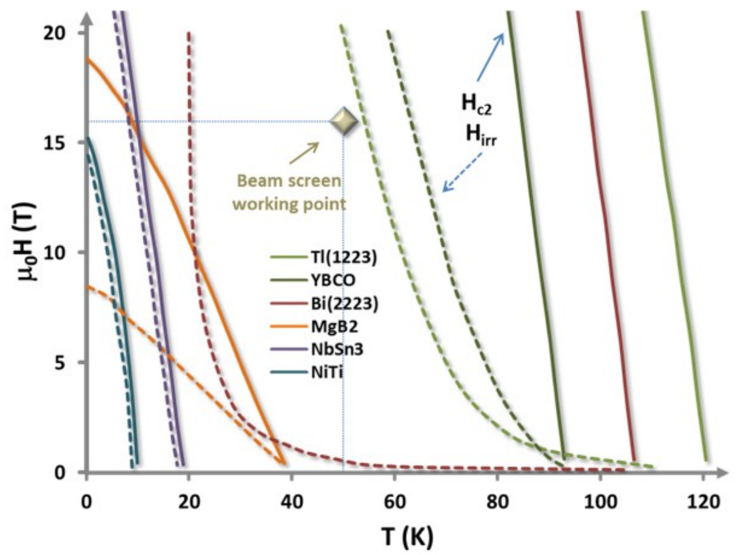

Figure 4.19: Magnetic field (T) vs temperature (T) graph showing the beam screen working point (50 K at 16 T) [27]. The irreversibility field (H_{irr}) lines (dashed ones) of different superducting materials are displayed: according to H_{irr}, Tl-1223 and YBCO are suitable candidates for the beam screen coating.

Thallium is toxic and highly volatile: the production of Tl-1223 thin films is therefore challenging. The sample preparation performed at CNR-SPIN (Genoa, Italy) involved an electrochemical deposition [151], [152], [26] on both Ag and STO substrates for the production of the precursor films, and a heat treatment at temperatures close to 900 ° C, i.e. "thallination process", for the formation of the final phase. Since changes were made to the thallination process in the course of thin film production, we differentiated between three types of samples (see Table 4.1).
Our electron microscopy analyses aimed at assessing the formation of the desired phase Tl-1223 and the quality of the substrate coverage for these three sample types. Furthermore, as precursor-pellets or -bulks used for the thallination process were expected to be almost pure Tl-1223, we also characterized their microstruture. We therefore employed EDX spectroscopy with scanning electron microscopy (SEM) and transmission electron microscopy (TEM). In this way, we were able to follow and evaluate the progress of the Tl-1223 film production process conducted at CNR-SPIN.

According to our EDX investigations performed on precursor-pellets, they showed to be mostly characterized by Tl-1223 grains along with a few grains/spots rich in some specific elements composing the phase of interest.
All deposited thin films had thicknesses between 1 and 2 μm. In general, all samples showed grains (of various shapes in type 1 samples and plate-like for type 2 and 3 samples) disconnected and randomly oriented.
Here some conclusions drawn on each sample type:

Type 1 thin films proved to be inhomogeneous in terms of thickness, coverage of the substrate (clearly visible in different regions), also presenting impurities, and grains of various shapes and very often rich in Cu, Ca, Sr or Ba. However, we found the Tl1223 phase of interest in elongated structures spread over the entire surface and in some agglomerates of about 5 μm.

Type 2 thin films still showed a poor coverage as seen in the type 1 samples. They were mostly characterized by elongated Cu- and Sr-rich structures, and big plate-like grains of Tl-1212 (size up to 200 μm) overlaid with grains of Tl-1223. In some cases, ”tilted” grains of Tl-1212 appeared to be trying to emerge from the substrate, being largely covered by Ag stemming from the substrate itself. In addition, C-rich impurities were found distributed throughout the surface.

Type 3 thin films showed better coverages than the previous sample types analyzed. We basically observed more plate-like grains, now smaller (size between 30 and 70 μm) than those found in the type 2 samples, less thickened with each other, and more homogeneously distributed across the film surface. All type 3 samples proved not only to have better substrate coverages, but also to be mainly characterized by Tl-1223 plate-like grains, and only a few Tl-1212 grains. This is a step forward in the optimization of the deposition process.

The study on the optimization of the film production process is going on: further work will be done on the parameters involved in the deposition process and heat treatment to obtain films with complete substrate coverages, effective grain-to-grain connection and a presence of progressively purer Tl-1223 phase. We are confident that this study will help to demonstrate the importance that such thallium-based HTSs can have in terms of superconducting properties and, thus, future high-energy applications.

5 MgB_2 for the FCC-hh superconducting links

5.1 Purpose of microstructural characterization

As previously described in Chapter 1, MgB_2 superconducting links, already under study for the HL-LHC project [11], would be located in the FCC-hh tunnel for carrying electricity from the power supplies to the magnet coils [1], [9], [10].

Lately, different research groups have been studying possible ways to enhance J_c of MgB_2 [156], [157], [158], [159],[97], [98], [99]: this aspect was observed as a consequence of partial substitution of B by carbon, after the reaction with C based compounds [35].

The innovative B nanostructuration process developed at CNR-SPIN in Genoa (previously described in Chapter 1) allows to homogeneously disperse a carbon source among boron oxide (B_2O_3) molecules through the atomization of solutions in cryogenic liquids [36]. The so-called freeze-drying process (FDP) permits to remove water, in order to obtain a homogenous dispersion of C in B_2O_3 solid phase. The nanostructured B_2O_3 is then reduced to C-doped nano-B by magnesiothermic process [97], [98], [99], [36]. Among various applications [35], [36], nanostructured boron is ideal for superconducting ones as it is related to the formation of nanosized boron grains, for which these conditions have to be met: a homogeneous replacement of some B atoms by C atoms and a homogeneous distribution of C-nanoaggregates (approx. 3 nm - 10 nm in size) being apart by 7 nm to 20 nm from each other. Such conditions are key to increasing J_c of the produced C-doped MgB_2 wires. The ideal values depend on working regime parameters, such as temperature and applied magnetic field [36], and on the type of the chosen C source.

The nominal carbon content refers to the amount introduced during the FDP preparation of the nano-B precursor. The nominal amounts of C (6 wt %) are divided into two percentage values in the final MgB_2 compounds, one of which gives the substitution of the B sites (at.%) and the other represents the C nanoaggregates (wt.%) [36].

In this work, the efficiency of C-doping was evalueted for haemoglobin and inulin as C sources. Our colleagues at CNR-SPIN observed that their C doping process using haemoglobin and inulin as C sources allowed to deploy up to 50% - 60% of the introduced C to replace B on its sites (depending on the nominal C content). This can be established through the determination of the MgB_2 cell parameters and the shift of T_c [36]. What about the leftover percentage (up to 40% - 50%) of the introduced C? We were expecting to find this percentage as C nanoaggregates homogeneously distributed within the MgB_2 matrix. Based on some considerations related to the coherence length (T=0 K) of MgB_2 and its lattice parameter [160], [36], a suitable size for such nanoaggregates would be in the range between 10 nm and 30 nm, and their distance from each other between 10 nm and 50 nm. To confirm this hypothesis, we prepared FIB lamellae (about 100 nm thick) from the polished MgB_2 wire cross-sections (polishing method A in Chapter 1), and we ivestigated them with TEM/STEM/HRTEM imaging and STEM EDX mapping. These techniques allowed us to better understand the behaviour of such doping agents [36].

5.1.0.1 TEM analysis

We employed TEM/STEM/HRTEM imaging to identify C nanoaggregates and for the recorded maps we had the following microscope settings: an electron beam energy of 200 keV, the sample tilted 25° towards the detector, a beam spot of 8 corresponding to a beam size of approx. 0.7 nm, an image resolution of approx. 100 × 100 pixels, a pixel time of 0.1 s, and a measurement step of about 7 nm. For the EDX mapping surveys we used Digital Micrograph Software, and DMS3 of GATAN Inc. for data analysis.

5.2 Results and discussion

In this section we present the analysis of a C-doped MgB_2 wire (BL13) developed by CNR-SPIN (Genoa), which is the most representative sample in terms of C nanoaggregate distribution. A STEM-EDX analysis of a comparable wire (BL17) will be also shown. Table 5.1 shows the main features of BL13 and BL17 (displayed in Figure 5.1).

Sample	BL13	BL17
C source	Inulin	Haemoglobin
C nominal content (wt%)	6	6
B type	nano-B by FDP and magnesiothermic process	nano-B by FDP and magnesiothermic process
Wire preparation	ex-situ PIT	ex-situ PIT

Table 5.1: Main features of the studied wires BL13 and BL17.

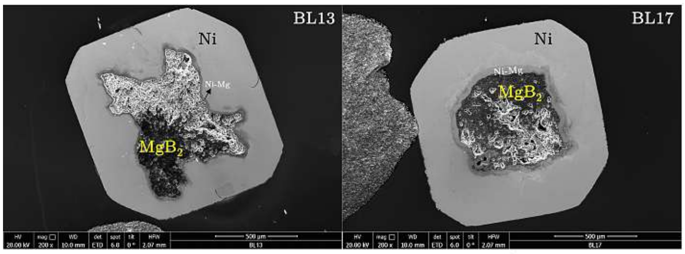

a b

Figure 5.1: SEM overview images of wires (a) BL13 and (b) BL17 taken with the ETD. MgB_2 is the dark core-region and the sorrounding area is characterized by a Ni sheath and a Ni-Mg layer with thicknesses between 10 μm and 60 μm.

5.2.0.1 TEM investigation

We first identified a certain C nanoaggregate/nanoparticle distribution through TEM bright-field (BF) imaging. Figure 5.2 shows a typical area of a C-doped MgB_2 sample. We are dealing in this case with the representative wire BL13. We observed distinctly similar C distribution areas for sample BL17, and so they will not be reported.

Most of the nanoaggregates in Figure 5.2 are between 30 nm and 60 nm in size (yellow circles) and are spaced 40 nm to 70 nm apart. Other smaller nanoaggregates are present (10-15 nm) and the smallest are as small as 3 nm (red circle). The darker regions in TEM-BF images generally represent thicker parts of the lamella. Considering that in TEM-BF images the vacuum is represented by the brightest areas, the thinner the sample, the less contrast there will be between the bright areas of the sample and the vacuum. If the lamella is thick, or it has areas of different thicknesses, the thicker parts will be the ones that contrast most with the vacuum (darker areas). Some dark spots, however, arise from oxygen and carbon contamination (Figure 5.2, bottom right), probably resulting from the manufacturing process.

In Figure 5.3 other two areas of sample BL13 with their C nanoaggregate distributions are shown. Again, some nanoaggregates are highlighted with circles and the green ones are those that could be either inside or above or below a grain. It should be noted that the best way to more clearly identify such nanoaggregates would be to prepare a very thin FIB lamella (about 50 nm) and thus avoid overlapping grains that might hinder their detection. The identification of the grains itself (approx. 100-200 μm in size for such samples) becomes difficult if the sample is not thin enough.

Although we were able to find important information about these samples, we were generally not able to give precise indications of the location of all C nanoaggregates (grain boundary/inside a grain). In fact, we have not yet found for these MgB_2 samples the best recipe to make them as thin as possible through the combination of FIB and PIPS preparation.

In some cases, however, C nanoaggregates clearly placed at the grain boundary were observed (as shown in Figure 5.4). The inset on the right of Figure 5.4 represents an HR-TEM image taken at 400000x magnification, where a C nanoaggregate of about 20 nm is visible at the grain boundary.

Figure 5.3 (right) also shows some nanoaggregates of about 10-15 nm in size (circled in black), which appear to be at grain boundaries. In both areas of Figure 5.3, we mostly observed nanoaggregates with size between 10 and 30 nm (yellow circles), and a few of approx. 3 nm (red circles). Such nanoaggregates are spaced from 10 to 100 nm apart. The nanoaggregate circled in blue (about 15 nm) seems to be in a ”cloud” of O/C contamination. We have highlighted some nanoaggregates through coloured circles as representative of a specific size range, but there are others (mostly around 2-3 nm in diameter) spread throughout the selected regions.

Speaking of contamination, we also observed areas mainly at the edge of the lamella where small particles very close to each other and of size between 1 and 5 nm were visible (see Figure 5.5). These artefacts are due to FIB-induced damage and they are very typical to be found at the edge of a FIB-prepared lamella [161]. Such damaged regions are usually defined as "amorphized". The FIB preparation also very often leads to the presence of gallium-rich zones (considering that Ga is the heavy ion typically characterizing the focused beam used with FIB machines). An example of Ga-rich zones can be seen in Figure 5.6: along with these bright zones, C nanoaggregates ranging in size from 10 nm to 50 nm are visible.

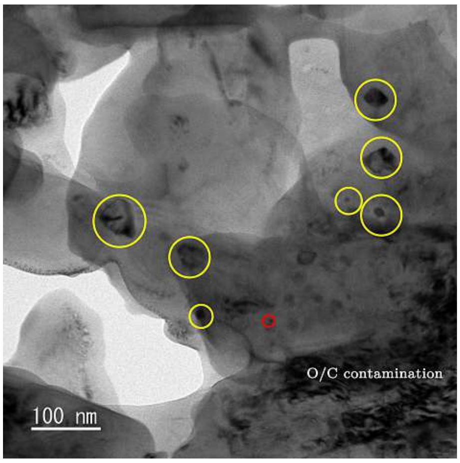

Figure 5.2: TEM-BF image showing a typical area in C-doped MgB_2 wires with C nanoaggregate distribution. Most of the nanoaggregates in this area are between 30 nm and 60 nm in size (yellow circles) and are spaced 40 to 70 nm apart. The smallest nanoaggregates are as small as 3 nm (red circle). The dark spot at the bottom right of the image is due to O and C contamination, probably stemming from the manufacturing process. It should be noticed that these nanoaggregates, highlighted with coloured circles, are representative of a specific size range, but there are others (mostly around 2-3 nm in diameter, thus more difficult to observe directly) spread throughout the selected regions.

We used STEM imaging and STEM-EDX mapping to further investigate C distribution within the MgB_2 matrix. Figure 5.7 represents an example HAADF-STEM image (taken for sample BL13) where we also performed EDX mapping to better distinguish C-rich areas and the MgB_2 matrix. The corresponding EDX maps showing Mg (yellow), B (red), and C (green) present in this area are also displayed. In this sample area where Mg, B and C are simultaneously present, a C nanoparticle with size of about 80 nm is highlighted (bright green spot pointed out with a yellow circle). The different green intensities in the EDX map of C are due to different C contents over the selected region: the brighter the colour, the more C will be present in that area. The highlighted C nanoparticle (80 nm) is the largest in this area, which is actually mostly characterized by aggregates of particles with diameters between 20 nm and 50 nm [36].

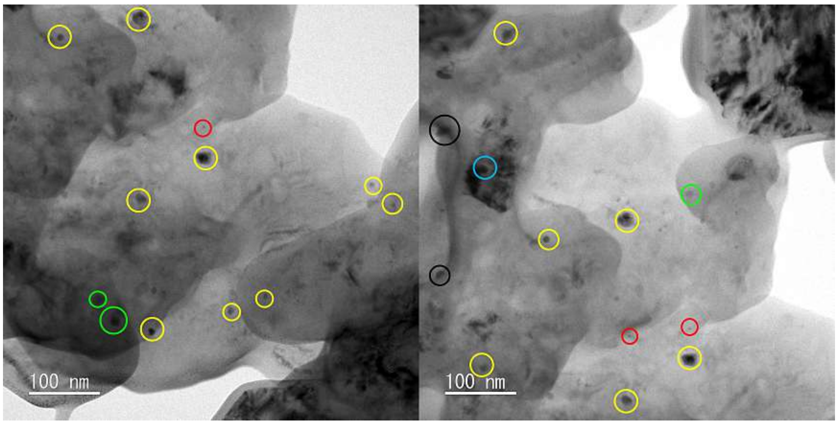

Figure 5.3: TEM-BF images showing two representative areas of C nanoaggragate distributions in C-doped MgB_2 wires. In both areas, most of the nanoaggregates show a size between 10 and 30 nm (yellow circles), and only a few of them have a size of approx. 3 nm (red circles). Such nanoaggregates are spaced from 10 to 100 nm apart. The nanoaggregates circled in black (about 10-15 nm in size) appear to be at grain boundaries and the aggregate circled in blue (about 15 nm) seems to be in a "cloud" of O/C contamination.The green ones are those that could be either inside or above or below a grain. It should be noticed that these nanoaggregates, highlighted with coloured circles, are representative of a specific size range, but there are others (mostly around 2-3 nm in diameter) spread throughout the selected regions.

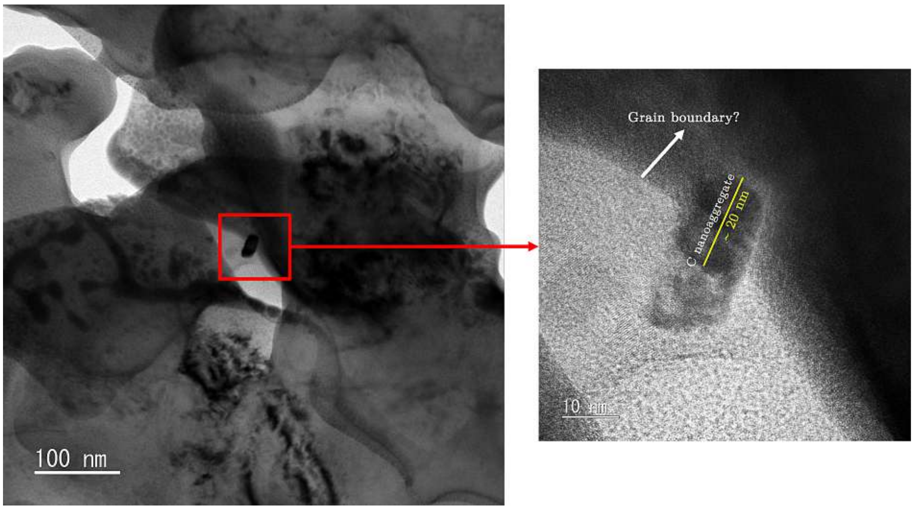

Figure 5.4: HR-TEM image taken at a magnification of 400000x, where a C nanoaggregate located at the grain boundary with size of about 20 nm can be observed.

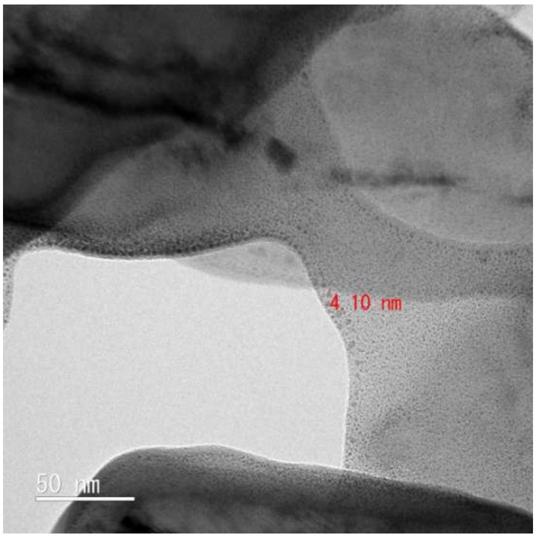

Figure 5.5: TEM-BF image showing an amorphized region at edge of the lamella, where FIB damaging is visible. Specifically, it results in particle-shaped small atefacts very close to each other of size between 1 and 5 nm.

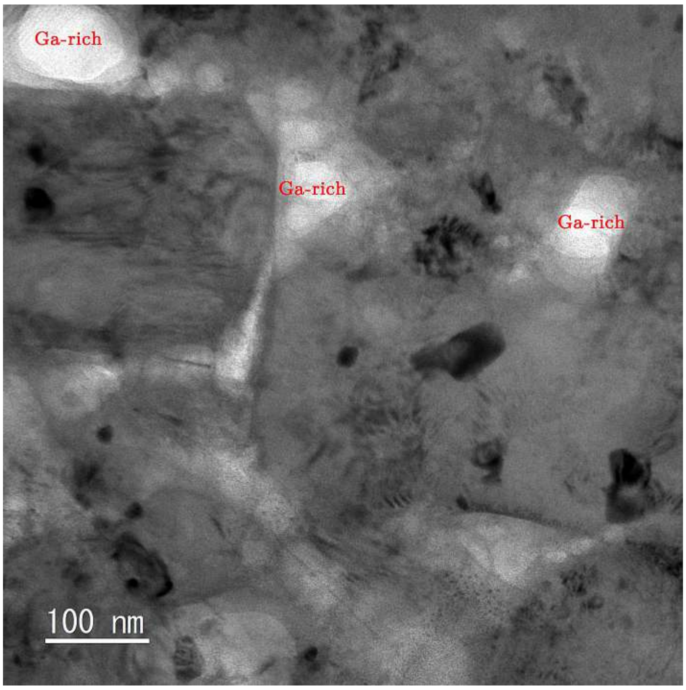

Figure 5.6: TEM-BF image showing an area of sample BL13 where Ga-rich zones can be observed. Along with such bright zones, C nanoaggregates ranging in size from 10 nm to 50 nm are visible.

As an example of the distribution of C within the MgB_2 matrix, we also report the STEM-EDX analysis performed for the BL17 wire. Specifically, Figure 5.8 shows a STEM image of a C-rich region and related EDX maps that give information about the content (at%) of Mg (yellow), B (red), and C (green) in this area. Looking at 3 and 4 EDX maps, it can be noticed that C is mainly present at grain boundaries. In map 4 we set the C detection limit to 20 at%, so we could observe small amounts of C even within the MgB_2 grains. The brighter green spots in this map are related to amounts of C above the given limit (20 at%), and reflecting the results visible in map 3. To give more precise information about these amounts of C, we would have to increase the number of pixels per area under analysis and the measurement time per pixel: this would lead to very long measurement times, which would be beyond the scope of this work.

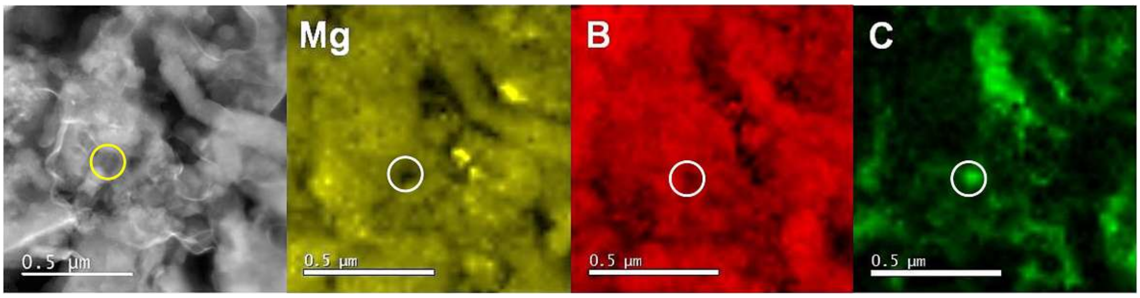

Figure 5.7: HAADF-STEM image of an example area (wire BL13) where we performed EDX mapping, and corresponding EDX elemental maps: Mg (yellow), B (red) and C (green). The yellow circle highlights a C nanoparticle with a diameter of approx. 80 nm.

In Figure 5.9 the percent compositions of Mg, B, and C are shown for a certain region (yellow rectangle) within a MgB_2 grain (white dashed circle). The percentage composition of C is clearly higher at the grain boundary (about 45%) than within the grain (approx between 2% and 8%).

Through our TEM analysis, we were able to investigate the distribution of C within the MgB_2 volume and find it both at grain boundaries (higher amounts) and inside grains (smaller amounts). Most importantly, we were able to confirm what we expected: the residual percentage of C is present as homogeneously dispersed C nanoaggregates within the MgB_2 matrix. In particular, we observed mainly nanoaggregates ranging in size from 10 nm to 50 nm and distanced 10 nm to 100 nm one from the other. These experimental results demonstrated the effectiveness of the FDP in producing C nanoaggregates properly distanced from each other and of a size suitable for being pinning centers with great potential in terms of J_c enhancement [36].

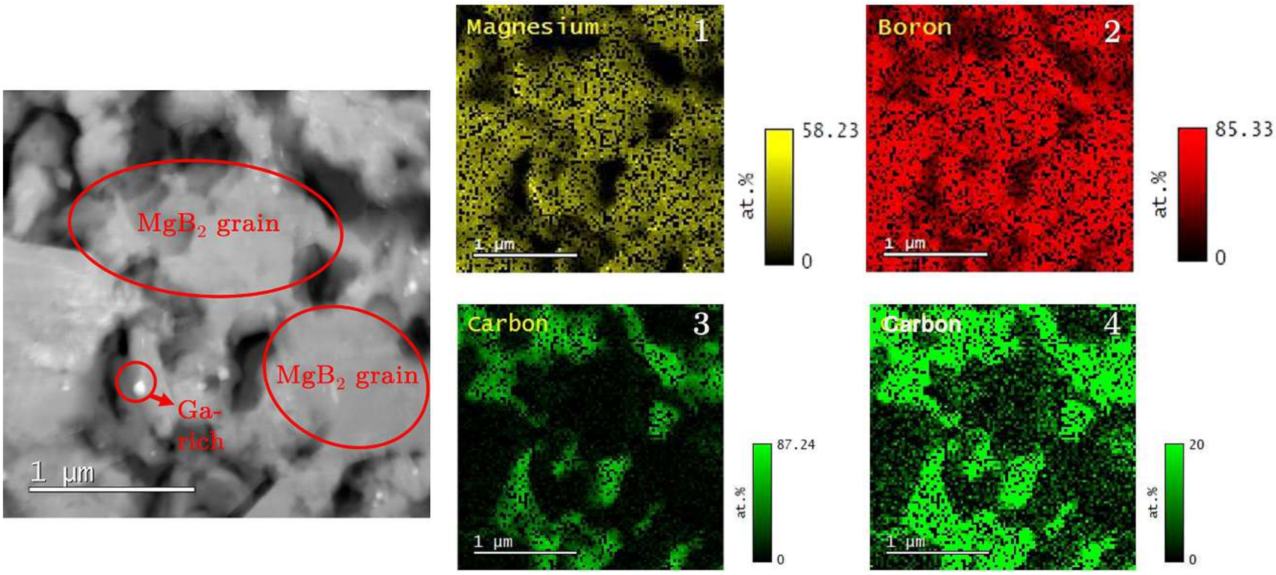

Figure 5.8: STEM-EDX analysis performed for the BL17 wire. A HAADF-STEM image of a C-rich region is shown on the left and EDX maps are displayed on the right giving information about the content (at%) of Mg (1-yellow), B (2-red), and C (3 and 4-green). C map 3 shows the maximum C content (at%) within this area. In C map 4 the C detection limit is set at 20 at% to identify small amounts of C within the MgB_2 grains. The white spots are Ga-rich and two MgB_2 grains are highlighted with red circles.

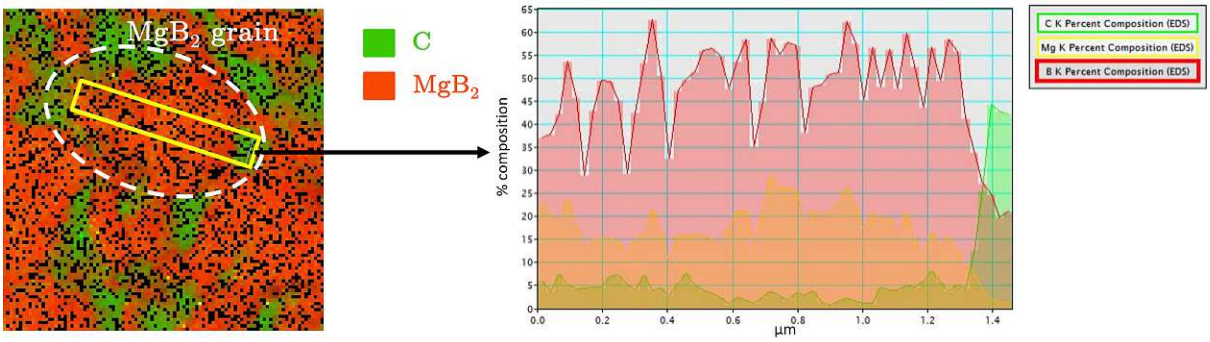

Figure 5.9: Mg, B, and C percent compositions of a certain region (yellow rectangle) within a MgB_2 grain (dashed white circle).

5.3 Summary and outlook

For carrying electricity from the power supplies to the magnet coils, MgB_2 superconducting links would be located in the FCC-hh tunnel, being already under study for the CERN HL-LHC project [11],[1], [9], [10].

Lately different research groups have been studying possible ways to enhance J_c of MgB_2 [156], [157], [158], [159],[97], [98], [99]: this aspect was observed as a consequence of partial substitution of B by carbon, after the reaction with C based compounds [35].
In thix context, we characterized the microstructure of C-doped MgB_2 wires (see Table 5.1) produced at CNR-SPIN (Genoa) using haemoglobin and inulin as C sources. In particular, we aimed at better understanding C dispersion within the MgB_2 matrix. The innovative B nanostructuration process developed at CNR-SPIN in Genoa (described in Chapter 1) allows to homogeneously disperse a carbon source among boron oxide (B_2O_3) molecules through the atomization of solutions in cryogenic liquids [36]. The so-called freeze-drying process (FDP) permits to remove water, in order to obtain a homogenous dispersion of C in B_2O_3 solid phase. The nanostructured B_2O_3 is then reduced to C-doped nano-B by magnesiothermic process [97], [98], [99], [36]. This is then the starting B used to subsequently produce C-doped MgB_2 via ex-situ PIT [36].
Through our TEM characterization (TEM/STEM imaging and STEM-EDX mapping), we were able to investigate the distribution of C within the MgB_2 volume and find it both at grain boundaries (higher amounts) and inside grains (smaller amounts). Most importantly, we were able to confirm what we expected: beside a percentage of C substituting B on its sites (50%-60% of the introduced C), the residual percentage is present as homogeneously distributed C nanoaggregates within the MgB_2 matrix. These C nanoaggregates are thus dispersed in the B grains volume first and afterwards within its compounds. In particular, we observed mainly nanoaggregates ranging in size from 10 nm to 50 nm and distanced 10 nm to 100 nm one from the other. Based on some considerations related to the coherence length (T=0 K) of MgB_2 and its lattice parameter [160], [36], such results demonstrated the effectiveness of the FDP in producing C nano-aggregates properly distanced from each other and of a size suitable for being pinning centers with great potential in terms of J_c enhancement.
This technique used at CNR-SPIN, employing the FDP, can be a worth solution for the lack on the market in terms of manufacturing methods producing nano-B precursors whose defects are introduced in a controlled way [36].

6 Concluding Remarks

In the challenging project for the realization of the CERN future hadron collider (FCC-hh), a target energy of 100 TeV is foreseen inside a 100-km-long tunnel thanks to two counter-rotating proton beams of 50 TeV each. Nb_3Sn, Tl-1223, and MgB_2 represent the best candidate superconductors for some of the FCC-hh main components.
In this work, we presented the microstructural investigations by different electron microscopy techniques (described in Chapter 2) of Nb_3Sn as the material envisioned for the FCC-hh dipole bending magnets (Chapter 3), Tl-1223 for the low surface resistance FCC-hh beam screen (Chapter 4), and MgB_2 for the FCC-hh superconducting links (Chapter 5). The main focus of this thesis was the microstructural characterization and comparison between different types of Nb_3Sn wires.

Nb_3Sn is the LTS candidate envisioned for the FCC-hh dipole bending magnets responsible for steering the proton beams and keeping them in orbit inside the tunnel. This material is currently the most cost-effective solution able to satisfy the requirements of J_c (non-Cu) = 1.5 kA/mm2 at 16 T and 4.2 K. Within this frame, a three-cluster layout of prototype internal tin Nb_3Sn wires, developed by TVEL and the Bochvar Institute (Russia), was analyzed and compared to a standard layout produced by the same manufacturer with the same heat treatment. Typically, the main reason for dividing the sub-element into clusters is to reduce the effective sub-element size (d_{eff}). Our idea was to clarify if cluster layouts, due to Nb-free routes in their starting sub-elements (before heat treatment), can reduce the Sn concentration gradient over the wire cross-section. It is known that the homogeneity in Sn concentration influences the wire properties: in general, the higher the homogeneity, the higher the J_c. We also compared two TVEL/Bochvar Institute wires showing the same six-cluster layout but reacted with different heat treatments. We could therefore face the Sn gradient investigation from another perspective, not only related to another type of cluster layout but also influenced by the heat treatment. We evaluated the effect of cluster and standard layouts on the Sn concentration gradient over the wire cross-section by employing energy dispersive X-ray (EDX) spectroscopy with both scanning electron microscopy (SEM) and transmission electron microscopy (TEM). Furthermore, we performed scanning Hall probe microscopy (SHPM) measurements to understand how these cluster sub-elements, with their specific geometry, influence the local currents flowing through the wire cross-section on a microscopic scale.
The EDX results observed for the cluster layout samples suggested a high potential in terms of radial homogeneity. Catalyzing Sn diffusion through the Nb-free Cu channels towards the peripheral barrier can be an effective way to produce wires with a more homogeneous Sn distribution, an optimized average Sn content, and a resulting higher

superconducting performance. Moreover, the local currents evaluated from SHPM show a J_c consistent with the HL-LHC standards, which can be further improved by acting on the manufacturing process steps and the heat treatment parameters. Future studies on different cluster-type samples reacted with the same heat treatment could be very useful to steer the manufacturing processes towards the production of more homogeneous and higher performing wires.

We also analyzed five internally oxidized artificial pinning centres (APC) Nb_3Sn wires produced with different heat treatments by Hyper Tech Inc. (Ohio, US). We investigated the nanoprecipitate (PP) characterizing such samples (ZrO_2/HfO_2) by high-angle anular dark-field scanning TEM (STEM-HAADF) to evaluate their size and density. Moreover, we employed SEM transmission Kikutchi diffraction (SEM-TKD) to analyze Nb_3Sn grain size. Our main objective here was to study the correlation between PP size-density and heat treatment, and Nb_3Sn grain size and heat treatment, since these factors play an important role in the typical high performance of APC wires. This investigation is part of a work still ongoing as new samples have recently arrived. The preliminary results were consistent with previous similar studies, although not yet representative of the dependence of the wire properties on the heat treatment performed and PP type. More samples and lamellae per sample (thus higher statistics) would be needed to have a more thorough understanding of the grain size, PP size, and PP density dependence on heat treatment. The completion of this work will bring a significant contribution towards a deeper understanding of the high performance of internally oxidized APC wires, which seem to represent a very promising technology for superconducting magnets of future applications, both in the medical and the high-energy physics fields.

For both wire types (IT and APC), it might be interesting to perform the same analysis described before on different slices (cross-sections) of the same wire to evaluate how its properties vary longitudinally (along the wire length).

Since the FCC-hh is expected to produce unprecedented amounts of synchrotron radiation, a superconducting beam screen is necessary to prevent this radiation from impinging on the dipole magnets. This beam screen would be kept at 50 K for cryogenic efficiency and, as beam stability requires to minimize its surface impedance, the HTS Tl-1223 would be a good alternative to the Cu currently used for the LhC beam screen. The deposition process of Tl-1223 thin films should be scalable to the size of the FCC-hh components, but this still represents a challenge as thallium is toxic and highly volatile. We received different Tl-1223 thin film samples produced at CNR-SPIN (Genoa) trough an electrochemical deposition on both Ag and STO substrates, and a "thallination process" at temperatures close to 900 °C. We employed EDX spectroscopy with both SEM and TEM to follow and evaluate the progress of the Tl-1223 film production process conducted at CNR-SPIN. Our analyses aimed to evaluate the formation of the desired Tl-1223 phase and the quality of substrate coverage for three types of samples coming from slightly different thallination processes.

All sample types showed grains disconnected and randomly oriented. Despite this, the latest thin films produced showed clear improvements in terms of substrate coverage and formation of plate-like grains characterized primarily by the desired Tl-1223 phase.

Although this represents an effective step towards the optimization of the production process, further studies are needed to find an optimal recipe to obtain high quality Tl-1223 thin films with complete substrate coverages, effective grain-to-grain connection, and a progressively purer Tl-1223 phase. We are confident that this study will help to demonstrate the importance that such thallium-based HTSs can have in terms of advanced superconducting properties and, thus, future high-energy applications.

MgB_2 superconducting links, already under study for the CERN HL-LHC project, will be located in the FCC-hh tunnel to transmit current from the power supplies to the magnet coils.

The enhancement of J_c in MgB_2 was observed by different research groups as a consequence of partial substitution of B by carbon, after the reaction with C based compounds. We characterized the microstructure of C-doped MgB_2 wires produced at CNR-SPIN (Genoa) using nano-B precursors obtained by freeze-drying process (FDP) and magnesiothermic process. We performed TEM/STEM imaging and STEM-EDX mapping to better understand C dispersion within the MgB_2 matrix. These investigations confirmed that beside a percentage of C replacing B on its sites, there is a residual C in the form of nanoaggregates homogeneously distributed within the MgB_2 matrix. In particular, we demonstrated the effectiveness of the FDP in producing C nano-aggregates properly distanced from each other and of a size suitable for being pinning centers with great potential in terms of J_c enhancement.

The technique used at CNR-SPIN, employing the FDP, can be a valid solution for the lack on the market in terms of manufacturing methods producing nano-B precursors whose defects are introduced in a controlled way.

This work has contributed new insights into the effectiveness of alternative manufacturing processes on the microstructural properties of different superconducting materials, strictly related to their electro-magnetic performance, with the perspective of optimizing such conductors for high-energy physics applications.

References

[1] the FCC Collaboration, A. Abada, M. Abbrescia, S. S. AbdusSalam, I. Abdyukhanov, J. Abelleira Fernandez, M. J. Baldwin, A. H. Ball, M. J. Barnes, W. Chou, P. J. Clark, C. T.A. Cook, S. J. de Jong, J. Ellis, J. Gao, J. Gao, P. C. Harris, R. Islam, A. Kilic, K. Lee, S. Lee, S. Li, R. Li, Z. Liu, M. P. Lombardo, A. J.G. Lunt, R. Martin, O. Martin, R. Patterson, J. Shelton, B. K. Singh, T. M. Taylor, G. N. Taylor, S. Thomas, L. T. Wang, R. Wang, K. Wang, B. F.L. Ward, N. K. Watson, P. H. Williams, A. Winter, X. Wu, G. Yang, H. J. Yang, T. T. Yu, F. Yu, Z. Zhang, Y. Zhang, C. Zhang, H. Zhang, and J. Zhou. Fcc-hh: The hadron collider: Future circular collider conceptual design report volume 3. *European Physical Journal - Special Topics*, 228(4):755–1107, July 2019. ISSN 1951-6355. doi: 10.1140/epjst/e2019-900087-0.

[2] FCC collaboration et al. Fcc-ee: The lepton collider: Future circular collider conceptual design report volume 2. *European Physical Journal: Special Topics*, 228(2):261–623, 2019.

[3] FCC collaboration et al. He-lhc: The high-energy large hadron collider: Future circular collider conceptual design report volume 4. *European Physical Journal: Special Topics*, 228(5):1109–1382, 2019.

[4] T Lehtinen, JP Penttinen, T Salmi, A Stenvall, FCC Collaboration, et al. Fcc physics opportunities. *EUROPEAN PHYSICAL JOURNAL C*, 79(6), 2019.

[5] Future circular collider. `https://home.cern/science/accelerators/future-circular-collider`. Accessed: 2021-02-18.

[6] Amalia Ballarino. Development of superconducting links for the large hadron collider machine. *Superconductor Science and Technology*, 27(4):044024, 2014. doi: 10.1088/0953-2048/27/4/044024. URL `https://doi.org/10.1088/0953-2048/27/4/044024`.

[7] Davide Tommasini, B. Auchmann, Hugues Bajas, Marta Bajko, Amalia Ballarino, Giovanni Bellomo, Michael Benedikt, Susana Izquierdo Bermudez, Bernardo Bordini, Luca Bottura, Marco Buzio, Marc Dhalle, Maria Durante, Gijs de Rijk, Pasquale Fabbricatore, Stefania Farinon, Paolo Ferracin, Peng Gao, Friedrich Lackner, Clement Lorin, Vittorio Marinozzi, Teresa Martinez, J. Munilla, Toru Ogitsu, Rafal Ortwein, Juan Perez, M. Prioli, Jean-Michel Rifflet, Etienne Rochepault, Stephan Russenschuck, Tiina Salmi, Frederic Savary, Daniel Schoerling, Michel Segreti, Carmine Senatore, Massimo Sorbi, Antti Stenvall, Ezio Todesco,

Fernando Toral, Arjan P. Verweij, Giovanni Volpini, Sander Wessel, and Felix Wolf. The 16 t dipole development program for fcc. *IEEE Transactions on Applied Superconductivity*, 27(4):1–5, 2017. doi: 10.1109/TASC.2016.2634600.

[8] J Van Nugteren, Daniel Schoerling, G Kirby, J Murtomaki, G De Rijk, L Rossi, L Bottura, H Ten Kate, and M Dhallé. Layout study for the dipole magnets of the future circular collider using nb-ti and nb 3 sn. *IEEE transactions on applied superconductivity*, 26(4):1–6, 2016.

[9] Lucio Rossi and Oliver Brüning. High luminosity large hadron collider: A description for the european strategy preparatory group. Technical report, 2012.

[10] HiLumi LHC collaboration et al. Fp7 high luminosity large hadron collider design study. Technical report, FP7-INFRASTRUCTURES-2011-1, 2011.

[11] Giorgio Apollinari, O Brüning, Tatsushi Nakamoto, and Lucio Rossi. High luminosity large hadron collider hl-lhc. *arXiv preprint arXiv:1705.08830*, 2017.

[12] Amalia Ballarino and Luca Bottura. Targets for r&d on nb 3 sn conductor for high energy physics. *IEEE Transactions on applied superconductivity*, 25(3):1–6, 2015.

[13] Lucio Rossi and Luca Bottura. Superconducting magnets for particle accelerators. *Reviews of accelerator science and technology*, 5:51–89, 2012.

[14] Alexander V. Zlobin and Daniel Schoerling. *Superconducting Magnets for Accelerators*, pages 3–22. Springer International Publishing, Cham, 2019. ISBN 978-3-030-16118-7. doi: 10.1007/978-3-030-16118-7_1. URL `https://doi.org/10.1007/978-3-030-16118-7_1`.

[15] I Bellafont, M Morrone, L Mether, J Fernández, R Kersevan, C Garion, V Baglin, P Chiggiato, and F Pérez. Design of the future circular hadron collider beam vacuum chamber. *Physical Review Accelerators and Beams*, 23(3):033201, 2020.

[16] Daniel Schoerling, Davide Tommasini, Hugo Bajas, Friedrich Lackner, Mikko Karppinen, Ezio Todesco, Vittorio Parma, Susana Izquierdo Bermudez, Marta Bajko, Attilio Milanese, et al. Strategy for superconducting magnet development for a future hadron-hadron circular collider at cern. Technical report, FCC-DRAFT-ACC-2015-023, 2015.

[17] Amalia Ballarino, Simon C Hopkins, Bernardo Bordini, David Richter, Davide Tommasini, Luca Bottura, Michael Benedikt, Michinaka Sugano, Toru Ogitsu, Shinya Kawashima, et al. The cern fcc conductor development program: a worldwide effort for the future generation of high-field magnets. *IEEE Transactions on Applied Superconductivity*, 29(5):1–9, 2019.

[18] R Flükiger, Davide Uglietti, Carmine Senatore, and Florin Buta. Microstructure, composition and critical current density of superconducting nb3sn wires. *Cryogenics*, 48(7-8):293–307, 2008.

[19] A Godeke, A Den Ouden, Arend Nijhuis, and Herman HJ ten Kate. State of the art powder-in-tube niobium–tin superconductors. *Cryogenics*, 48(7-8):308–316, 2008.

[20] T Baumgartner, J Hecher, J Bernardi, S Pfeiffer, C Senatore, and M Eisterer. Assessing composition gradients in multifilamentary superconductors by means of magnetometry methods. *Superconductor Science and Technology*, 30(1):014011, nov 2016. doi: 10.1088/0953-2048/30/1/014011. URL `https://doi.org/10.1088%2F0953-2048%2F30%2F1%2F014011`.

[21] Paolo Mele, Kosmas Prassides, Chiara Tarantini, Anna Palau, Petre Badica, Alok K Jha, and Tamio Endo. *Superconductivity: From Materials Science to Practical Applications*. Springer Nature, 2019.

[22] X Xu, M Sumption, X Peng, and EW Collings. Refinement of nb3sn grain size by the generation of zro2 precipitates in nb3sn wires. *Applied Physics Letters*, 104 (8):082602, 2014.

[23] Johannes Gutleber. Future circular collider study overview for easitrain, Mar 2018. URL `https://indico.cern.ch/event/638333/sessions/258026/attachments/1610740/2557536/FCC-1802281519-JGU_FCCOverview4EASITRAIN.pdf`.

[24] Stephen J Blundell. *Superconductivity: a very short introduction*. OUP Oxford, 2009.

[25] Michael I Faley. Epitaxial oxide heterostructures for ultimate high-tc quantum interferometers. *Applications of High-Tc Superconductivity, Rijeka: InTech*, pages 147–176, 2011.

[26] A Leveratto, A Saba, S Holleis, M Himmerlich, B Henrist, S Fernandez-Peña, A Moros, J Bernardi, M Eisterer, C Bernini, et al. Future circular collider beam screen: progress on tl-1223 hts coating. *Superconductor Science and Technology*, 33(5):054004, 2020.

[27] S Calatroni, E Bellingeri, C Ferdeghini, M Putti, R Vaglio, T Baumgartner, and M Eisterer. Thallium-based high-temperature superconductors for beam impedance mitigation in the future circular collider. *Superconductor Science and Technology*, 30(7):075002, 2017.

[28] Sergio Calatroni. Hts coatings for impedance reduction in particle accelerators: case study for the fcc at cern. *IEEE Transactions on Applied Superconductivity*, 26(3):1–4, 2016.

[29] E. Bellingeri, H.L. Suo, J.-Y. Genoud, M. Schindl, E. Walker, and R. Flukiger. Electrodeposition of biaxially aligned tl-based superconductors on ag tapes. *IEEE Transactions on Applied Superconductivity*, 11(1):3122–3125, 2001. doi: 10.1109/77.919724.

[30] Shailaj Kumar Shrivastava. Deposition techniques for high-tc superconducting ybco thin films. *Journal Home page: http://www. ijmra. us*, 5(6), 2017.

[31] G Brorsson, Z Ivanov, and P-Å Nilsson. In situ ybco thin films made by laser deposition. In *Science and Technology of Thin Film Superconductors 2*, pages 169–175. Springer, 1990.

[32] Maw-Kuen Wu, Jo R Ashburn, ClJ Torng, Ph H Hor, Rl L Meng, Lo Gao, Z Jo Huang, YQ Wang, and aCW Chu. Superconductivity at 93 k in a new mixed-phase y-ba-cu-o compound system at ambient pressure. *Physical review letters*, 58(9): 908, 1987.

[33] Alessandro Leveratto. Hts tl-based coatings for the fcc-hh beam screens, Apr 2018. URL `https://indico.cern.ch/event/656491/contributions/2947262/attachments/1629683/2597137/FCC2018_ALeveratto.pdf`.

[34] S Berta, S Brisigotti, A Tumino, D Pietranera, G Grasso, and A Ballarino. Development of mgb2 conductors for application to superconducting bus. *CERN EDMS no*, 965302, 2008.

[35] A Ballarino and R Flükiger. Status of mgb2 wire and cable applications in europe. In *Journal of Physics: Conference Series*, volume 871, page 012098. IOP Publishing, 2017.

[36] Marco Capra, Federico Loria, Cristina Bernini, Gianmarco Bovone, Alice Moros, Michael Stöger-Pollach, Thomas Schachinger, Johannes Bernardi, Antonio Sergio Siri, and Maurizio Vignolo. Method for the production of pure and c-doped nanoboron powders tailored for superconductive applications. *Nanotechnology*, 31 (49):494001, 2020.

[37] G Ercolini. Communications from the physical laboratory of the university of leiden. *Il Nuovo Cimento (1895-1900)*, 11(1):319–320, 1900.

[38] David Dew-Hughes. The critical current of superconductors: an historical review. *Low temperature physics*, 27(9):713–722, 2001.

[39] J-L. Jorda. *Thallium-Based Superconducting Cuprates*, pages 833–868. Springer Berlin Heidelberg, Berlin, Heidelberg, 2005. ISBN 978-3-540-27294-6. doi: 10.1007/3-540-27294-1_22. URL `https://doi.org/10.1007/3-540-27294-1_22`.

[40] Syahrul Humaidi. Development of tbcco high temperature superconductor. In *AIP Conference Proceedings*, volume 2221, page 020002. AIP Publishing LLC, 2020.

[41] Roman Mankowsky, Alaska Subedi, Michael Först, Simon O Mariager, Matthieu Chollet, HT Lemke, Jeffrey S Robinson, James M Glownia, Michael P Minitti, Alex Frano, et al. Nonlinear lattice dynamics as a basis for enhanced superconductivity in yba 2 cu 3 o 6.5. *Nature*, 516(7529):71–73, 2014.

[42] Wikipedia contributors. History of superconductivity — Wikipedia, the free encyclopedia. `https://en.wikipedia.org/w/index.php?title=History_of_superconductivity&oldid=1019027146`, 2021. [Online; accessed 9-June-2021].

[43] Elliot Snider, Nathan Dasenbrock-Gammon, Raymond McBride, Mathew Debessai, Hiranya Vindana, Kevin Vencatasamy, Keith V Lawler, Ashkan Salamat, and Ranga P Dias. Room-temperature superconductivity in a carbonaceous sulfur hydride. *Nature*, 586(7829):373–377, 2020.

[44] Wikipedia contributors. Room-temperature superconductor — Wikipedia, the free encyclopedia. `https://en.wikipedia.org/w/index.php?title=Room-temperature_superconductor&oldid=1025515199`, 2021. [Online; accessed 9-June-2021].

[45] Alok K Jha and Kaname Matsumoto. Superconductive rebco thin films and their nanocomposites: the role of rare-earth oxides in promoting sustainable energy. *Frontiers in Physics*, 7:82, 2019.

[46] Carsten Timm. Theory of superconductivity. *Institute of theoretical Physics Dresden*, 2012.

[47] Charles K Poole, Horacio A Farach, and Richard J Creswick. *Handbook of superconductivity*. Elsevier, 1999.

[48] Masatsugu Suzuki and Itsuko S Suzuki. Lecture note on solid state physics ginzburg-landau theory for superconductivity. *Department of Physics, State University of New York at Binghamton, Binghamton, New York*, pages 13902–6000, 2007.

[49] David Larbalestier, Alex Gurevich, D Matthew Feldmann, and Anatoly Polyanskii. High-tc superconducting materials for electric power applications. *Materials For Sustainable Energy: A Collection of Peer-Reviewed Research and Review Articles from Nature Publishing Group*, pages 311–320, 2011.

[50] Alexis P Malozemoff. High t c for the power grid. *Nature materials*, 6(9):617–619, 2007.

[51] SR Foltyn, L Civale, JL MacManus-Driscoll, QX Jia, B Maiorov, H Wang, and M Maley. Materials science challenges for high-temperature superconducting wire. *Nature materials*, 6(9):631–642, 2007.

[52] Ram Gopal Sharma. *Superconductivity: Basics and applications to magnets*, volume 214. Springer, 2015.

[53] Emanuela Barzi and Alexander V Zlobin. Nb3sn wires and cables for high-field accelerator magnets. *Nb3Sn Accelerator Magnets*, page 23, 2019.

[54] Arno Godeke. A review of the properties of nb3sn and their variation with a15 composition, morphology and strain state. *Superconductor Science and Technology*, 19(8):R68, 2006.

[55] JP Charlesworth, I Macphail, and PE Madsen. Experimental work on the niobium-tin constitution diagram and related studies. *Journal of Materials Science*, 5(7): 580–603, 1970.

[56] CS Pande. Transmission electron microscopy of radiation damage in nb3sn. *physica status solidi (a)*, 52(2):687–696, 1979.

[57] Teruo Matsushita et al. *Flux pinning in superconductors*, volume 164. Springer, 2007.

[58] Emanuela Barzi and Alexander V Zlobin. Research and development of nb_3sn wires and cables for high-field accelerator magnets. *IEEE Transactions on Nuclear Science*, 63(2):783–803, 2016.

[59] Amalia Ballarino. Superconducting materials for high field applications, Sep 2018. URL `https://indico.cern.ch/event/663949/sessions/275484/attachments/1711937/2760652/Lecture_Amalia.pdf`.

[60] Xingchen Xu. A review and prospects for nb3sn superconductor development. *Superconductor Science and Technology*, 30(9):093001, 2017.

[61] A Godeke, Matthew C Jewell, Chad M Fischer, Alexander A Squitieri, Peter J Lee, and David C Larbalestier. The upper critical field of filamentary nb 3 sn conductors. *Journal of applied physics*, 97(9):093909, 2005.

[62] E Gregory, M Tomsic, X Peng, R Dhaka, VR Nazareth, and MD Sumption. Niobium tin conductors for high energy physics, fusion, mri and nmr applications made by different techniques. *IEEE transactions on applied superconductivity*, 18 (2):989–992, 2008.

[63] PX Zhang, Y Feng, XH Liu, CG Li, K Zhang, XD Tang, and Y Wu. Microstructure and superconducting properties comparison of bronze and internal tin process nb3sn strands for iter. *Physica C: Superconductivity*, 469(15-20):1536–1540, 2009.

[64] AR Kaufmann and JJ Pickett. Multifilament nb3sn superconducting wire. *Journal of Applied Physics*, 42(1):58–58, 1971.

[65] Giorgio Ambrosio. Nb3sn high field magnets for the high luminosity lhc upgrade project. *IEEE Transactions on Applied Superconductivity*, 25(3):1–7, 2014.

[66] Victor Pantsyrny. Design features and microstructure of the commercially produced high jc internal tin nb3 sn strands with one common diffusion barrier, Apr 2018. URL `https://indico.cern.ch/event/656491/contributions/2915688/attachments/1629001/2595627/2018-FCC-week-_Conductor_Development_in_Russia-3.pdf`.

[67] Leszek R Motowidlo, PJ Lee, C Tarantini, S Balachandran, AK Ghosh, and DC Larbalestier. An intermetallic powder-in-tube approach to increased flux-pinning in nb3sn by internal oxidation of zr. *Superconductor Science and Technology*, 31(1):014002, 2017.

[68] Xingchen Xu, Xuan Peng, Michael Sumption, and EW Collings. Recent progress in application of internal oxidation technique in nb3sn strands. *IEEE Transactions on Applied Superconductivity*, 27(4):1–5, 2016.

[69] Xingchen Xu, Michael D Sumption, and Xuan Peng. Internally oxidized nb3sn strands with fine grain size and high critical current density. *Advanced Materials*, 27(8):1346–1350, 2015.

[70] Shreyas Balachandran, Chiara Tarantini, Peter J Lee, Fumitake Kametani, Yi-Feng Su, Benjamin Walker, William L Starch, and David C Larbalestier. Beneficial influence of hf and zr additions to nb4at% ta on the vortex pinning of nb3sn with and without an o source. *Superconductor Science and Technology*, 32(4):044006, 2019.

[71] Akira Iyo, Yasumoto Tanaka, Yumiko Ishiura, Madoka Tokumoto, Kazuyasu Tokiwa, Tsuneo Watanabe, and Hideo Ihara. Study on enhancement of tc ($\geq$ 130 k) in tlba2ca2cu3oy superconductors. *Superconductor Science and Technology*, 14 (7):504, 2001.

[72] Ryoji Sugise, Masayuki Hirabayashi, Norio Terada, Masatoshi Jo, Takehiko Shimomura, and Hideo Ihara. The formation process of new high-tc superconductors with single-layer thallium-oxide, tlba2ca2cu3oy and tlba2ca3cu4oy. *Japanese journal of applied physics*, 27(9A):L1709, 1988.

[73] R Shipra, Juan Carlos Idrobo, and Athena S Sefat. Superconducting and structural features of tl-1223. *arXiv preprint arXiv:1505.00816*, 2015.

[74] M Jergel, A Conde Gallardo, C Falcony Guajardo, and V Strbik. Tl-based superconductors for high-current, high-field applications. *Superconductor Science and Technology*, 9(6):427, 1996.

[75] TL Aselage, EL Venturini, JA Voigt, and DJ Miller. Stability of the tl-1223 phases. *Journal of materials research*, 11(7):1635–1644, 1996.

[76] Kurt A Richardson. *The manufacture of high temperature superconducting tapes and films*. Universal-Publishers, 1999.

[77] David A Cardwell and DS Ginley. Handbook of superconducting materials volume 2: Characterization, applications and cryogenics. 2002.

[78] David R Armstrong and Peter G Perkins. Electronic band structure of magnesium diboride. *Journal of the Chemical Society, Faraday Transactions 2: Molecular and Chemical Physics*, 75:12–16, 1979.

[79] FL Stavale, JL Gonzalez, ES Yugue, and E Baggio-Saitovitch. Phase diagram for (tl0. 5pb0. 5)(ba0. 2sr0. 8) 2ca2cu3o8+ δ (tl-1223) polycrystalline sample with optimum oxygen content. *Physica C: Superconductivity*, 408:54–55, 2004.

[80] DH Kim, KE Gray, RT Kampwirth, JC Smith, DS Richeson, Tobin J Marks, JH Kang, J Talvacchio, and M Eddy. Effect of cu-o layer spacing on the magnetic field induced resistive broadening of high-temperature superconductors. *Physica C: Superconductivity*, 177(4-6):431–437, 1991.

[81] Hans Hermann Otto. Comment and supplement to structural refinement of the high-tc superconductor tlba2ca2cu3o9, 2016.

[82] Emilio Bellingeri, Roman E Gladyshevskii, and René Flükiger. Textured tl (1223)/ag tapes prepared by electrophoretic deposition. *Journal of superconductivity*, 11(1):77–78, 1998.

[83] J-Y Genoud, Hong Li Suo, Michael Schindl, Emilio Bellingeri, Thomas Tybell, Eric Walker, and R Flukiger. Preparation of {110} textured ag ribbons for biaxially aligned superconducting tapes. *IEEE transactions on applied superconductivity*, 11(1):3371–3374, 2001.

[84] Jun Nagamatsu, Norimasa Nakagawa, Takahiro Muranaka, Yuji Zenitani, and Jun Akimitsu. Superconductivity at 39 k in magnesium diboride. *nature*, 410(6824): 63–64, 2001.

[85] J Akimitsu. paper presented at the symposium on transition metal oxides. *Sendai, Japan*, 10, 2001.

[86] V Russell, R Hirst, FA Kanda, and AJ King. An x-ray study of the magnesium borides. *Acta Crystallographica*, 6(11-12):870–870, 1953.

[87] NV Vekshina, Ya L Markovskii, Yu D Kondrashev, and TK Voevedskaya. Binary borides of al and mg. *J. Appl. Chem*, 44:970–974, 1971.

[88] Karl E Spear. Chemical bonding in alb2-type borides. *Journal of the Less Common Metals*, 47:195–201, 1976.

[89] JD Jorgensen, DG Hinks, and S Short. Lattice properties of mgb 2 versus temperature and pressure. *Physical Review B*, 63(22):224522, 2001.

[90] Halima Zaari, Sufyan Naji, AG El Hachimi, Abdelilah Benyoussef, and Abd Allah El Kenz. The investigations of electronic structure, optical and magnetic properties of mgb 2 nanosheets. In *2014 International Renewable and Sustainable Energy Conference (IRSEC)*, pages 931–934. IEEE, 2014.

[91] Eiji Nishibori, Masaki Takata, Makoto Sakata, Hiroshi Tanaka, Takahiro Muranaka, and Jun Akimitsu. Bonding nature in mgb2. *Journal of the Physical Society of Japan*, 70(8):2252–2254, 2001.

[92] Zi-Kui Liu, DG Schlom, Qi Li, and XX Xi. Thermodynamics of the mg–b system: Implications for the deposition of mgb 2 thin films. *Applied Physics Letters*, 78 (23):3678–3680, 2001.

[93] Harald van Weeren. Magnesium diboride superconductors for magnet applications. 2007.

[94] Rene Flukiger. *MgB2 Superconducting Wires: Basics and Applications*, volume 2. World Scientific, 2016.

[95] SK Chen, KA Yates, MG Blamire, and JL MacManus-Driscoll. Strong influence of boron precursor powder on the critical current density of mgb2. *Superconductor Science and Technology*, 18(11):1473, 2005.

[96] MAA Mahmud, Mike A Susner, Mike D Sumption, Matthew A Rindfleisch, Michael J Tomsic, Jinji Yue, and Edward W Collings. Comparison of critical current density in mgb_2 with different boron sources and nano-particle dopant additions. *IEEE transactions on applied superconductivity*, 19(3):2756–2759, 2009.

[97] Maurizio Vignolo, Gennaro Romano, Alberto Martinelli, Cristina Bernini, and Antonio S Siri. A novel process to produce amorphous nanosized boron useful for mgb_2 synthesis. *IEEE transactions on applied superconductivity*, 22(4):6200606–6200606, 2012.

[98] G Bovone, M Vignolo, C Bernini, S Kawale, and AS Siri. An innovative technique to synthesize c-doped mgb2 by using chitosan as the carbon source. *Superconductor Science and Technology*, 27(2):022001, 2013.

[99] Maurizio Vignolo, Gianmarco Bovone, Davide Matera, Davide Nardelli, Cristina Bernini, and Antonio Sergio Siri. Nano-sized boron synthesis process towards the large scale production. *Chemical Engineering Journal*, 256:32–38, 2014.

[100] Linda H Jansen. Boron, elemental. *Kirk-Othmer Encyclopedia of Chemical Technology*, pages 1–9, 2000.

[101] Wikipedia contributors. Future circular collider — Wikipedia, the free encyclopedia. `https://en.wikipedia.org/w/index.php?title=Future_Circular_Collider&oldid=1025489829`, 2021. [Online; accessed 14-June-2021].

[102] URL `http://easitrain.web.cern.ch/network.html`.

[103] Ray Egerton. *Physical principles of electron microscopy: An introduction to TEM, SEM, and AEM*. 01 2005. ISBN 0387258000. doi: 10.1007/b136495.

[104] Dale E. Newbury, David C. Joy, Patrick Echlin, Charles E. Fiori, and Joseph I. Goldstein. *Electron Channeling Contrast in the SEM*, pages 87–145. Springer US, Boston, MA, 1986. ISBN 978-1-4757-9027-6. doi: 10.1007/978-1-4757-9027-6_3. URL `https://doi.org/10.1007/978-1-4757-9027-6_3`.

[105] Glenn C. Sneddon, Patrick W. Trimby, and Julie M. Cairney. Transmission kikuchi diffraction in a scanning electron microscope: A review. *Materials Science and Engineering: R: Reports*, 110:1–12, 2016. ISSN 0927-796X. doi: https://doi.org/10.1016/j.mser.2016.10.001. URL `https://www.sciencedirect.com/science/article/pii/S0927796X16300493`.

[106] X.Z. Liang, M.F. Dodge, J. Jiang, and H.B. Dong. Using transmission kikuchi diffraction in a scanning electron microscope to quantify geometrically necessary dislocation density at the nanoscale. *Ultramicroscopy*, 197:39–45, 2019. ISSN 0304-3991. doi: https://doi.org/10.1016/j.ultramic.2018.11.011. URL `https://www.sciencedirect.com/science/article/pii/S0304399118300883`.

[107] Quang Duc Truong, Murukanahally Kempaiah Devaraju, Takaaki Tomai, and Itaru Honma. Direct observation of antisite defects in licopo4 cathode materials by annular dark- and bright-field electron microscopy. *ACS Applied Materials & Interfaces*, 5(20):9926–9932, 2013. doi: 10.1021/am403018n. URL `https://doi.org/10.1021/am403018n`. PMID: 24060566.

[108] Wikipedia contributors. Dark-field microscopy — Wikipedia, the free encyclopedia. `https://en.wikipedia.org/w/index.php?title=Dark-field_microscopy&oldid=1006157630`, 2021. [Online; accessed 14-February-2021].

[109] Wikipedia contributors. Transmission electron microscopy — Wikipedia, the free encyclopedia. `https://en.wikipedia.org/w/index.php?title=Transmission_electron_microscopy&oldid=998179358`, 2021. [Online; accessed 14-February-2021].

[110] P.D. Nellist and S.J. Pennycook. The principles and interpretation of annular dark-field z-contrast imaging. volume 113 of *Advances in Imaging and Electron Physics*, pages 147–203. Elsevier, 2000. doi: https://doi.org/10.1016/S1076-5670(00)80013-0. URL `https://www.sciencedirect.com/science/article/pii/S1076567000800130`.

[111] Wikipedia contributors. Annular dark-field imaging — Wikipedia, the free encyclopedia. `https://en.wikipedia.org/w/index.php?title=Annular_dark-field_imaging&oldid=997011486`, 2020. [Online; accessed 16-February-2021].

[112] Johannes Hecher. *Current transport in polycrystalline iron based superconductors*. PhD thesis, Wien, 2016.

[113] Thomas Carlson. *Photoelectron and Auger spectroscopy*. Springer Science & Business Media, 2013.

[114] Siegfried Hofmann. *Auger-and X-ray photoelectron spectroscopy in materials science: a user-oriented guide*, volume 49. Springer Science & Business Media, 2012.

[115] AK Ghosh, LD Cooley, AR Moodenbaugh, J Parrell, MB Field, Y Zhang, and S Hong. Magnetization studies of high j/c/ nb/3/sn strands. *IEEE transactions on applied superconductivity*, 15(2):3494–3497, 2005.

[116] PA Lukyanov, VI Pantsyrny, MV Polikarpova, VV Guryev, DS Novosilova, KO Bazaleeva, AS Tsapleva, MV Alekseev, AG Silaev, IM Abdyukhanov, et al. The comparative study of the internal tin nb3sn wires with different layouts. In *Journal of Physics: Conference Series*, volume 1559, page 012061. IOP Publishing, 2020.

[117] Bruce A Zeitlin, Eric Gregory, Taeyoung Pyon, RM Scanlan, Anatolii A Polyanskii, and Peter J Lee. Progress on the use of internal fins as barriers to reduce magnetization on high current density mono element internal tin conductors (meit). In *AIP Conference Proceedings*, volume 711, pages 417–424. American Institute of Physics, 2004.

[118] Bruce A Zeitlin. A high current density low cost niobium 3 tin titanium doped conductor utilizing a novel internal tin process. Technical report, Supergenics LLC, 2005.

[119] Eric Gregory. Final report sbir phase ii. high current density,(jc), low ac loss, low cost, internal-tin superconductor. 1 2009. doi: 10.2172/946132. URL `https://www.osti.gov/biblio/946132`.

[120] NJ Pugh, JE Evetts, and ER Wallach. A transmission electron microscopy study of bronze-processed nb 3 sn and (nb, ta) 3 sn multifilamentary superconducting wire. *Journal of materials science*, 20(12):4521–4526, 1985.

[121] V Abacherli, D Uglietti, P Lezza, B Seeber, R Flukiger, M Cantoni, and P-A Buffat. The influence of ti doping methods on the high field performance of (nb, ta, ti)/sub 3/sn multifilamentary wires using osprey bronze. *IEEE transactions on applied superconductivity*, 15(2):3482–3485, 2005.

[122] Carmine Senatore, Giorgio Mondonico, Florin Buta, Bernd Seeber, René Flükiger, Bernardo Bordini, Patrick Alknes, and Luca Bottura. Phase formation, composition and tc distribution of binary and ta-alloyed nb3sn wires produced by various techniques. *IEEE Transactions on Applied Superconductivity - IEEE TRANS APPL SUPERCONDUCT*, 22:6001304–6001304, 06 2012. doi: 10.1109/TASC.2011.2178992.

[123] Peter J Lee and David C Larbalestier. Microstructure, microchemistry and the development of very high nb/sub 3/sn layer critical current density. *IEEE transactions on applied superconductivity*, 15(2):3474–3477, 2005.

[124] D Uglietti, B Seeber, V Abächerli, A Pollini, D Eckert, and R Flükiger. A device for critical current versus strain measurements up to 1000 a and 17 t on 80 cm long hts and lts technical superconductors. *Superconductor Science and Technology*, 16 (9):1000, 2003.

[125] Dave A Shirley. High-resolution x-ray photoemission spectrum of the valence bands of gold. *Physical Review B*, 5(12):4709, 1972.

[126] Sven Tougaard. Universality classes of inelastic electron scattering cross-sections. *Surface and Interface Analysis: An International Journal devoted to the development and application of techniques for the analysis of surfaces, interfaces and thin films*, 25(3):137–154, 1997.

[127] J Hrn Scofield. Hartree-slater subshell photoionization cross-sections at 1254 and 1487 ev. *Journal of Electron Spectroscopy and Related Phenomena*, 8(2):129–137, 1976.

[128] M Suenaga, DO Welch, RL Sabatini, OF Kammerer, and S Okuda. Superconducting critical temperatures, critical magnetic fields, lattice parameters, and chemical compositions of "bulk"pure and alloyed nb3sn produced by the bronze process. *Journal of applied physics*, 59(3):840–853, 1986.

[129] MV Krylova, IM Abdyukhanov, AS Tsapleva, EA Dergunova, K Mareev, MV Alekseev, IA Karateev, AV Ovcharov, IN Trunkin, MM Potapenko, et al. The microstructure of nb3sn superconductors differing in the number of copper inserts at various stages of heat treatment. In *IOP Conference Series: Materials Science and Engineering*, volume 502, page 012174. IOP Publishing, 2019.

[130] Charlie Sanabria. New understanding of the heat treatment of nb-sn superconducting wires. 2017.

[131] Charlie Sanabria, Michael Field, Peter J Lee, Hanping Miao, Jeff Parrell, and David C Larbalestier. Controlling cu–sn mixing so as to enable higher critical current densities in rrp® nb3sn wires. *Superconductor Science and Technology*, 31(6):064001, 2018.

[132] Simon C Hopkins, Algirdas Baskys, Amalia Ballarino, Jonas Lachmann, and Andreas Leineweber. Phase evolution during heat treatment of nb¡sub¿3¡/sub¿sn wires under development for the fcc study. *IEEE Transactions on Applied Superconductivity*, pages 1–1, 2021. doi: 10.1109/TASC.2021.3063675.

[133] M Klemm, E Seibt, W Specking, JQ Xu, and R Flukiger. Enhancement of jc at 10-12 t in nb3sn wires by artificial ta inclusions distributed at a nanometre scale. *Superconductor Science and Technology*, 3(5):249, 1990.

[134] M Suenaga and W Jansen. Chemical compositions at and near the grain boundaries in bronze-processed superconducting nb3sn. *Applied physics letters*, 43(8):791–793, 1983.

[135] M. B. Field, Y. Zhang, H. Miao, M. Gerace, and J. A. Parrell. Optimizing Nb$_3$Sn conductors for high field applications. *IEEE Transactions on Applied Superconductivity*, 24(3):1–5, 2014. doi: 10.1109/TASC.2013.2285314.

[136] Xingchen Xu, Xuan Peng, Jacob Rochester, Jae-Yel Lee, and Mike Sumption. High critical current density in internally-oxidized nb3sn superconductors and its origin. *Scripta Materialia*, 186:317–320, 2020.

[137] Xingchen Xu, Jacob Rochester, Xuan Peng, Mike Sumption, and Mike Tomsic. Ternary nb3sn superconductors with artificial pinning centers and high upper critical fields. *Superconductor Science and Technology*, 32(2):02LT01, 2019.

[138] Jacob Rochester, Mattia Ortino, Xingchen Xu, Xuan Peng, and Mike D Sumption. The roles of grain boundary refinement and nano-precipitates in flux pinning of apc nb 3 sn. *IEEE Transactions on Applied Superconductivity*, 2021.

[139] X Xu, X Peng, J Rochester, MD Sumption, J Lee, GA Calderon Ortiz, and J Hwang. The strong influence of ti, zr, hf solutes and their oxidation on microstructure and performance of nb3sn superconductors. *Journal of Alloys and Compounds*, 857:158270, 2021.

[140] Chiara Tarantini, Shreyas Balachandran, Steve M Heald, Peter J Lee, Nawaraj Paudel, Eun Sang Choi, William L Starch, and David C Larbalestier. Ta, ti and hf effects on nb3sn high-field performance: temperature-dependent dopant occupancy and failure of kramer extrapolation. *Superconductor Science and Technology*, 32 (12):124003, 2019.

[141] Stephan Pfeiffer. *The Microstructure of Nb3Sn Superconductors for the Future Circular Collider Project and its Impact on the Performance*. PhD thesis, Wien, 2020.

[142] Edward J Kramer. Scaling laws for flux pinning in hard superconductors. *Journal of Applied Physics*, 44(3):1360–1370, 1973.

[143] DR Dietderich and A Godeke. Nb3sn research and development in the usa–wires and cables. *Cryogenics*, 48(7-8):331–340, 2008.

[144] George F Vander Voort. *Metallography, principles and practice*. ASM international, 1999.

[145] Satyam Suwas and Ranjit Kumar Ray. *Crystallographic texture of materials*. Springer, 2014.

[146] Xingchen Xu. *Prospects for improving the critical current density of superconducting Nb3Sn strands via optimization of Nb3Sn fraction, stoichiometry, and grain size*. PhD thesis, The Ohio State University, 2016.

[147] Arno Godeke. Performance boundaries in nb3sn superconductors. Technical report, Ernest Orlando Lawrence Berkeley NationalLaboratory, Berkeley, CA (US), 2006.

[148] Christopher Segal, Chiara Tarantini, Peter J Lee, and David C Larbalestier. Improvement of small to large grain a15 ratio in nb3sn pit wires by inverted multistage heat treatments. In *IOP Conference Series: Materials Science and Engineering*, volume 279, page 012019. IOP Publishing, 2017.

[149] Friedrich-Wilhelm Wellmer. *The Use of the Lognormal Distribution*, pages 67–94. Springer Berlin Heidelberg, Berlin, Heidelberg, 1998. ISBN 978-3-642-60262-7. doi: 10.1007/978-3-642-60262-7_9. URL `https://doi.org/10.1007/978-3-642-60262-7_9`.

[150] Wikipedia contributors. Log-normal distribution — Wikipedia, the free encyclopedia. `https://en.wikipedia.org/w/index.php?title=Log-normal_distribution&oldid=1012084202`, 2021. [Online; accessed 15-April-2021].

[151] E Bellingeri, HL Suo, J-Y Genoud, M Schindl, E Walker, and R Flukiger. Electrodeposition of biaxially aligned tl-based superconductors on ag tapes. *IEEE transactions on applied superconductivity*, 11(1):3122–3125, 2001.

[152] DY Jeong, YH Kim, PM Shirage, SY Kim, S Horiuchi, and JH Lee. A new process to prepare thick bufferless tl-1223/ag high temperature superconducting coated conductors using electrodeposition. *Superconductor Science and Technology*, 20 (12):1239, 2007.

[153] J. F. Konopka. Quantitative Analysis of Oxygen in Metal Oxides with SEM/EDS by Direct Measurement of all X-ray Peaks. In *AGU Fall Meeting Abstracts*, volume 2012, pages V23C–2831, December 2012.

[154] JE Tkaczyk, JA DeLuca, PL Karas, PJ Bednarczyk, MF Garbauskas, RH Arendt, KW Lay, and JS Moodera. Transport critical currents in spray pyrolyzed films of tlba2ca2cu3o z on polycrystalline zirconia substrates. *Applied physics letters*, 61 (5):610–612, 1992.

[155] XX Gao, W Xie, Z Wang, XJ Zhao, M He, X Zhang, SL Yan, and L Ji. The study of purity improvement on tl-1223 thin films by dc sputtering and post-annealing method. *Journal of Superconductivity and Novel Magnetism*, 27(7):1665–1670, 2014.

[156] SX Dou, XL Wang, J Horvat, D Milliken, AH Li, K Konstantinov, EW Collings, MD Sumption, and HK Liu. Flux jumping and a bulk-to-granular transition in the magnetization of a compacted and sintered mgb2 superconductor. *Physica C: Superconductivity*, 361(2):79–83, 2001.

[157] MA Susner, MD Sumption, M Bhatia, X Peng, MJ Tomsic, MA Rindfleisch, and EW Collings. Influence of mg/b ratio and sic doping on microstructure and high field transport jc in mgb2 strands. *Physica C: Superconductivity*, 456(1-2):180–187, 2007.

[158] Shu Jun Ye, Akiyoshi Matsumoto, Yun Chao Zhang, and Hiroaki Kumakura. Strong enhancement of high-field critical current properties and irreversibility field of mgb2 superconducting wires by coronene active carbon source addition via the new b powder carbon-coating method. *Superconductor Science and Technology*, 27(8):085012, 2014.

[159] GZ Li, MD Sumption, JB Zwayer, MA Susner, MA Rindfleisch, CJ Thong, MJ Tomsic, and EW Collings. Effects of carbon concentration and filament number on advanced internal mg infiltration-processed mgb2 strands. *Superconductor Science and Technology*, 26(9):095007, 2013.

[160] Cristina Buzea and Tsutomu Yamashita. Review of the superconducting properties of mgb2. *Superconductor Science and Technology*, 14(11):R115, 2001.

[161] Joachim Mayer, Lucille A Giannuzzi, Takeo Kamino, and Joseph Michael. Tem sample preparation and fib-induced damage. *MRS bulletin*, 32(5):400–407, 2007.